

**PULSED LASER DEPOSITION OF ALUMINIUM-DOPED ZINC  
OXIDE FILMS FOR OPTOELECTRONICS APPLICATION**

**REESON KEK**

**FACULTY OF SCIENCE  
UNIVERSITY OF MALAYA  
KUALA LUMPUR**

**2017**

**PULSED LASER DEPOSITION OF ALUMINIUM-DOPED ZINC  
OXIDE FILMS FOR OPTOELECTRONICS APPLICATION**

**REESON KEK**

**DISSERTATION SUBMITTED IN FULFILMENT OF THE  
REQUIREMENTS FOR THE DEGREE OF MASTER OF SCIENCE**

**DEPARTMENT OF PHYSICS  
FACULTY OF SCIENCE  
UNIVERSITY OF MALAYA  
KUALA LUMPUR**

**2017**

**UNIVERSITY OF MALAYA  
ORIGINAL LITERARY WORK DECLARATION**

Name of Candidate: **REESON KEK**

Matric No: **SGR150054**

Name of Degree: **MASTER OF SCIENCE**

Title of Dissertation:

**Pulsed Laser Deposition of Aluminum-doped Zinc Oxide Films  
for Optoelectronics Application.**

Field of Study: **Experimental Physics**

I do solemnly and sincerely declare that:

- (1) I am the sole author/writer of this Work;
- (2) This Work is original;
- (3) Any use of any work in which copyright exists was done by way of fair dealing and for permitted purposes and any excerpt or extract from, or reference to or reproduction of any copyright work has been disclosed expressly and sufficiently and the title of the Work and its authorship have been acknowledged in this Work;
- (4) I do not have any actual knowledge nor do I ought reasonably to know that the making of this work constitutes an infringement of any copyright work;
- (5) I hereby assign all and every rights in the copyright to this Work to the University of Malaya ("UM"), who henceforth shall be owner of the copyright in this Work and that any reproduction or use in any form or by any means whatsoever is prohibited without the written consent of UM having been first had and obtained;
- (6) I am fully aware that if in the course of making this Work I have infringed any copyright whether intentionally or otherwise, I may be subject to legal action or any other action as may be determined by UM.

Candidate's Signature

Date:

Subscribed and solemnly declared before,

Witness's Signature

Date:

Name:

Designation:

University of Malaya

**PULSED LASER DEPOSITION OF ALUMINIUM-DOPED ZINC OXIDE  
FILMS FOR OPTOELECTRONICS APPLICATION**

**ABSTRACT**

ZnO is one of the promising materials to be used for optoelectronics due to its direct and large bandgap at 3.3 eV. Pure ZnO shows n-type behaviour but in order to increase the stability and conductivity, group III element such as B, Al and Ga can be introduced as dopants. In this project Al-doped ZnO (AZO) thin films are deposited by pulsed laser deposition (PLD) on glass and Si substrates. The project is divided into two parts. In the first part, the properties of the AZO films deposited by 355 nm and 532 nm lasers are studied. The electrical properties of AZO film are measured by four-point probe whereas the optical properties of AZO film are measured by using Ultraviolet-visible (UV-Vis) spectrophotometer. Other characterization techniques include Scanning Electron Microscopy (SEM) and Atomic Force Microscopy (AFM) are used for measuring morphology of AZO films. The laser-produced plasma plume at different laser wavelengths and energy affects the electrical and optical properties of AZO films. By using ions probe and optical emission spectroscopy, the emission species, ions velocities and energy are obtained at different laser fluences and wavelengths. The relation of plasma characteristics and the properties of AZO thin films are discussed. In the second part, AZO thin films are deposited on p-Si (100) substrate to form AZO/Si heterojunction. The IV characteristics of the AZO/Si heterojunction are measured in dark and under illuminations. Photoresponse are observed from the AZO/Si heterojunction and the characteristics are studied.

**Keywords:**

laser-produced plasma, Al-doped Zinc Oxide (AZO), Pulsed Laser Deposition (PLD), AZO/p-Si heterojunction and Current-Voltage (I-V) Characteristics.

**PULSED LASER DEPOSITION OF ALUMINIUM-DOPED ZINC OXIDE  
FILMS FOR OPTOELECTRONICS APPLICATION**

**ABSTRAK**

Zink oksida (ZnO) berpotensi untuk digunakan dalam optoelektronik kerana jurang jalur tenaganya yang tinggi pada 3.3 eV. ZnO tulen menunjukkan ciri jenis-n, tetapi untuk meningkatkan kestabilan dan kekonduksiannya, unsur kumpulan III seperti B, Al dan Ga sering digunakan sebagai dopan. Dalam projek ini, filem nipis Zink Oksida Terdop Aluminium (AZO) dideposit oleh pemendapan laser berdenyut (PLD) di atas substrak silikon dan kaca. Projek ini dibahagikan kepada dua bahagian. Dalam bahagian pertama, ciri-ciri filem AZO yang diperolehi dengan laser 355 nm dan 532 nm dikaji. Ciri-ciri elektrik filem AZO diukur dengan penduga empat titik, manakala ciri-ciri optiknya diukur dengan menggunakan spektrofotometer Uv-vis. Teknik- teknik lain yang digunakan termasuk mikroskop imbasan electron (SEM) and mikroskop daya atom (AFM) diguna untuk ukur morfologi filem AZO. Plasma dihasilkan oleh laser dengan panjang gelombang dan tenaga yang berbeza boleh mempengaruhi sifat-sifat filem AZO. Oleh itu, dalam projek ini, plasma terbentuk dalam proses PLD dikaji dengan menggunakan teknik ion siasatan dan spektrokopi pemancaran optik di mana halaju dan tenaga spesies; dan juga jenis ion iditentukan. Hubungan antara ciri-ciri plasma dengan ciri-ciri filem AZO dibincangkan. Dalam bahagian kedua, filem AZO dideposit di atas silikon jenis-p Si (100) untuk membentuk struktur persimpangan hetero (heterojunction) AZO/p-Si. Ciri-ciri arus-voltan (I-V) untuk struktur AZO/p-Si diukur dalam keadaan gelap and di bawah diluminasi. Persimpangan hetero AZO/p-Si bertindak balas terhadap cahaya dan ciri-cirinya dikajikan.

**Keywords:**

laser-produced plasma, Al-doped Zinc Oxide (AZO), Pulsed Laser Deposition (PLD), AZO/p-Si heterojunction and Current-Voltage (I-V) Characteristics.

## ACKNOWLEDGEMENTS

This master project entitled “Pulsed Laser Deposition of Aluminium-doped Zinc Oxide Films for Optoelectronics Application” is never a work for anyone alone. All the hard works contributed by many different people in many different ways have made this possible. I would like to express my utmost and deepest gratitude and appreciation to my supervisors, Prof. Abdul Kariem Bin HJ Mohd Arof and Dr. Yap Seong Ling. I thank them for the encouragement and sincere supervision.

I would also like to thank Dr. Yap Seong Shan. She has been a tremendous mentor for me. But what attracted me the most was her passion in research and untiringly works to achieve excellence in research. She has groomed me from undergraduate to an independent researcher. My special thank for her continuous guidance particularly in the experimental aspects and assistant in dissertation preparation leading to the final completion of this project. Her willingness to share her knowledge with all her students is much appreciated.

Last but not least, my warmest appreciation to all my friends and my seniors especially Lim Lian Kuang, Ong Tean Sian, Lee Yen Sian and Ngoi Siew Kien for their passionate on assisting me during my hard time.

## TABLE OF CONTENTS

<b>ABSTRACT .....</b>	<b>iii</b>
<b>ABSTRAK .....</b>	<b>iv</b>
<b>ACKNOWLEDGEMENTS.....</b>	<b>v</b>
<b>TABLE OF CONTENTS.....</b>	<b>vi</b>
<b>LIST OF FIGURES .....</b>	<b>x</b>
<b>LIST OF TABLES .....</b>	<b>xvi</b>
<b>CHAPTER 1: INTRODUCTION.....</b>	<b>1</b>
1.1 Zinc Oxide (ZnO) based Material.....	1
1.1.1 Structure and Properties of ZnO.....	2
1.1.2 Electrical Properties of ZnO.....	3
1.1.3 Optical Properties of ZnO .....	4
1.1.4 Doping of ZnO .....	6
1.2 Application of ZnO based on Thin Films.....	9
1.2.1 UV light Source and Detector .....	9
1.2.2 Transparent Conducting Oxide.....	9
1.2.3 Piezoelectric Sensor .....	10
1.2.4 ZnO/Si heterojunction Optoelectronisc.....	10
1.3 Deposition Methods of ZnO .....	12
1.3.1 Spray Prolysis.....	13
1.3.2 Chemical Vapor Deposition (CVD) .....	14
1.3.3 Sputtering Deposition.....	15
1.3.4 Atomic Layer Deposition (ALD) .....	16
1.3.5 Pulsed Laser Deposition .....	17

1.4	Project Objectives .....	19
1.5	Problem Statement.....	19
1.6	Thesis Outline.....	20
<b>CHAPTER 2: LITERATURE REVIEW.....</b>		<b>21</b>
2.1	Introduction.....	21
2.2	PLD of AZO.....	21
2.2.1	The Effect of Dopant Concentration in AZO .....	21
2.2.2	The Effect of Laser Wavelength and Energy in PLD Growth of AZO....	23
2.2.3	The Effect of Oxygen Background Gas in Growth of AZO Thin Films..	26
2.2.4	The Effect of Substrate Temperature in Growth of AZO Films .....	27
2.3	ZnO/Si Heterojunction.....	29
2.3.1	Effect of Different Percentage of Al-dopant in AZO/Si Heterojunction .	35
2.3.2	Effect of UV and Visible Light in AZO/p-Si Heterojunction .....	38
2.3.3	Effect of Different Pressure in Growth Heterojunction .....	40
<b>CHAPTER 3: METHODOLOGY.....</b>		<b>42</b>
3.1	Introduction.....	42
3.2	Pulsed Laser Deposition (PLD) System .....	42
3.3	Deposition Parametes of AZO thin films .....	44
3.4	Plasma Diagnostics .....	45
3.4.1	Ion Probe Measurement.....	45
3.4.2	Optical Emission Spectroscopy (OES).....	46
3.5	AZO Thin Films Characterization Techniques .....	47
3.5.1	Stylus Profilometer .....	47
3.5.2	Scanning Electron Microscope (SEM).....	48
3.5.3	Atomic Force Microscopy (AFM).....	49

3.5.4	UV-VIS Spectrophotometry .....	50
3.5.5	Four Point Probe.....	51
3.5.6	X-Ray Diffraction (XRD).....	52
3.5.7	Room Temperature Photoluminescence .....	52
3.6	Fabrication and Characterization of AZO/p-Si Heterojunction .....	53
3.6.1	Fabrication for AZO/p-Si Heterojunction .....	53
3.6.2	Characterization of AZO/p-Si Heterojunction .....	54
<b>CHAPTER 4: PLASMA CHARACTERISTIC AND PROPERTIES OF AZO THIN FILMS BY PLD...</b> .....		<b>56</b>
4.1	Introduction .....	56
4.2	The Effect of Laser Wavelength and Fluence on the Plasma Characterization .....	56
4.2.1	Optical Emission Spectra .....	56
4.2.2	Time of Flight Measurement.....	59
4.3	The Effect of Laser Fluence and Laser Wavelength on the Properties of AZO Thin Films.....	63
4.3.1	Ablation Rate and Growth Rate .....	63
4.3.2	Surface Morphology .....	64
4.3.3	Crystallinity .....	73
4.3.4	Optical Properties .....	74
4.3.5	Electrical Resistivity.....	76
4.4	Summary .....	77
<b>CHAPTER 5: AZO/P-SI HETEROJUNCTION CHARACTERISTICS .....</b>		<b>81</b>
5.1	Introduction.....	81
5.2	Properties of AZO Samples and Fabrication of AZO/p-Si Structure Heterojunction.....	81
5.3	The Effect of Visible Light Illumination on AZO/p-Si Heterojunction.....	87

5.4	The Effect of UV Illumination on AZO/p-Si Heterojunction.....	96
5.5	Effect of Resistivity .....	103
5.6	Summary.....	110

**CHAPTER 6: CONCLUSIONS & SUGGESTIONS FOR FURTHER WORK ..113**

6.1	Conclusion .....	113
6.2	Suggestion for Further Work.....	115

**REFERENCES..... 116**

**LIST OF PUBLICATIONS..... 128**

University of Malaya

## LIST OF FIGURES

Figure 1.1	: (a) rocksalt, (b) zinc blende and (c) wurtzite crystalline structures of ZnO respectively.....	2
Figure 1.2	: (a) main planar surface of ZnO and (b) lattice vectors or unit cell axes of ZnO.....	3
Figure 1.3	: (a) ZnO valence and conduction bandgap. (b) Valence band maximum was set to zero.....	4
Figure 1.4	: Level position an electronic transition for the green luminescence (a) 300 K temperature and (b) less than 50 K temperature .....	5
Figure 1.5	: The optical bandgap of undoped ZnO on left and doped ZnO on right .....	7
Figure 1.6	: Schematic of ZnO/P-Si heterojunction solar cell .....	11
Figure 1.7	: Schematic cross section of the complete structure of ZnO/Si-based photodiode.....	12
Figure 1.8	: Schematic diagram of basic spray pyrolysis deposition system .....	14
Figure 1.9	: Schematic diagram of CVD system .....	15
Figure 1.10	: Schematic diagram of sputtering process system .....	16
Figure 1.11	: Schematic diagram of the ALD process. (a) precursor A(blue), (b) precursor B(blue), (c)precursor A and B and (d) desired film.....	16
Figure 1.12	: Schematic of Pulsed Laser Deposition System.....	17
Figure 1.13	: Schematic illustrating three different growth modes (a) 3D island growth (Volmer-Weber), (b) 2D layer-by-layer growth (Frank-van der Merwe) and (c) layer-by-layer followed by an island grow (Stranski Krastanov) .....	19
Figure 2.1	: The electrical properties of AZO in different percentage dopant.....	22
Figure 2.2	: The optical transparency of AZO in different percentage of Al-doped and undoped ZnO thin films .....	23
Figure 2.3	: SEM micrographs of the films deposited by (a) 248 nm laser and 532 nm laser.....	24

Figure 2.4	: Graph of resistivity versus different laser fluence for AZO thin film with two different laser wavelength (a) 355 nm and (b) 248 nm.....	24
Figure 2.5	: The electrical properties of AZO deposition at room temperature on the top and the transparency properties of AZO deposition at room temperature on the below .....	27
Figure 2.6	: (a) The transmittance spectra of AZO with various substrate temperature and (b) The Optical Bandgap with various substrate temperature.....	28
Figure 2.7	: The electrical properties in different substrate temperature .....	29
Figure 2.8	: n-ZnO/p-Si heterojunction energy diagram in zero bias and non-illuminated.....	32
Figure 2.9	: p-ZnO/n-Si heterojunction energy diagram in zero bias and un-illumination.....	33
Figure 2.10	: Energy band diagram and charge transport mechanism of n-ZnO/p-Si heterojunction under reverse and forward bias .....	34
Figure 2.11	: I-V characteristics of the undoped and Al-doped ZnO/p-si heterojunction at different Al concentration: (a) dark and (b) under illumination (340 nm.. light wavelength, 2 mW).....	36
Figure 2.12	: Current density- voltage (J-V) characteristics of Al-doped ZnO/p-Si heterojunctions at different Al-doping percentage: (a) 0.8 %, (b)1.0% (c) 1.2% and (d) 1.6 %.....	37
Figure 2.13	: I-V characteristics of the n-ZnO/p-Si heterojunction in the dark and illumination with (a) UV light (355 nm) and visible light (514 nm).The effect of the light intensity in (c) $I_{sc}$ and (d) $V_{oc}$ .....	39
Figure 2.14	: Energy band diagram and carriers transport mechanism of n-ZnO/p-Si heterojunction under (a) zero bias (b) forwards bias and (c) reverse bias.....	39
Figure 2.15	: The energy band diagram of the n-ZnO/p-Si heterojunction deposited with oxygen pressure of (a) $10^{-5}$ Torr and $10^{-4}$ Torr ; (b) $10^{-3}$ Torr and $10^{-2}$ Torr .....	41
Figure 2.16	: SEM image of ZnO and the I-V characteristics of the n-ZnO/p-Si heterojunction deposited by PLD with different oxygen pressure (a) $10^{-5}$ Torr, (b) $10^{-4}$ Torr (c) $10^{-3}$ Torr and (d) $10^{-2}$ Torr.....	41

Figure 3.1	: Schematic diagram of Pulsed Laser Deposition System.....	42
Figure 3.2	: Schematics diagram of laser beam delivery optics system.....	43
Figure 3.3	: Experiment set up for ions probe measurement.....	45
Figure 3.4	: Schematics diagram of the ion probe (Top View).....	46
Figure 3.5	: Schematics diagram of the optical emission spectroscopy set-up.....	47
Figure 3.6	: Electron-sample interaction mechanism.....	48
Figure 3.7	: UV-VIS spectrophotometer set-up.....	50
Figure 3.8	: (a) Schematic diagram of 4-point probe (b) Geometry of thin film which define the relationship between the sheet resistances.....	51
Figure 3.9	: Experiment set up for PL measurement.....	53
Figure 3.10	: Schematics diagram of the Ag/AZO/p-Si/Al structure.....	54
Figure 3.11	: (a) Diagram of the illumination system, (b) Spectrum of the illumination... visible light and (c) Spectrum of the illumination UV light.....	55
Figure 4.1	: Optical emission spectra of the ablation of AZO target with (a) 355 nm laser wavelength and (b) 532 nm laser wavelength.....	57
Figure 4.2	: The normalized intensity of the characteristics line of Zn I (334.50nm, 472.21 nm, 481.05 nm, 636.23 nm), Zn II (492.40 nm) and Al I (396.15 nm).....	58
Figure 4.3	: Time of flight signals of (a) 355 nm and (b) 532 nm laser ablation of AZO target at different laser fluence. Inserts show the ions signal measured at 2 J/cm <sup>2</sup> at different O <sup>2</sup> background pressure.....	59
Figure 4.4	: (a) ions velocity, (b) ions energy and (c) ion intensity of the 355 nm and 532 nm laser wavelength with different laser fluence.....	62
Figure 4.5	: AFM images of the AZO thin Films deposited in 355nm (2 J/cm <sup>2</sup> ).....	65
Figure 4.6	: AFM images of the AZO thin Films deposited in 355nm (4 J/cm <sup>2</sup> ).....	66
Figure 4.7	: AFM images of the AZO thin Films deposited in 532 nm (2 J/cm <sup>2</sup> ).....	66
Figure 4.8	: AFM images of the AZO thin Films deposited in 532 nm (4 J/cm <sup>2</sup> ).....	68
Figure 4.9	: Intensity of Al in the thin films.....	68

Figure 4.10	: (a) SEM image (b) EDX spectra of AZO films (c) AZO mapping image from EDS analyst of the AZO films deposited at 2 J/cm <sup>2</sup> , 355 nm laser wavelength.....	69
Figure 4.11	: (a) SEM image (b) EDX spectra of AZO films (c) AZO mapping image from EDS analyst of the AZO films deposited at 4 J/cm <sup>2</sup> , 355 nm laser wavelength.....	70
Figure 4.12	: (a) SEM image (b) EDX spectra of AZO films (c) AZO mapping image from EDS analyst of the AZO films deposited at 2 J/cm <sup>2</sup> , 532 nm laser wavelength.....	71
Figure 4.13	: (a) SEM image (b) EDX spectra of AZO films (c) AZO mapping image from EDS analyst of the AZO films deposited at 4 J/cm <sup>2</sup> , 532 nm laser wavelength.....	72
Figure 4.14	: XRD spectra of AZO thin films deposited on glass with different laser parameters.....	73
Figure 4.15	: Optical transmittance of AZO thin films deposited in different laser parameters.....	74
Figure 4.16	: Optical absorption coefficients of AZO thin films in function of photon energy for different laser parameters.....	75
Figure 4.17	: Photoluminescence spectra detected by 355 nm laser excitation of AZO target.....	78
Figure 5.1	: Optical properties of AZO films deposited in different laser parameters :(a) Optical transmittance of AZO thin films and (b) Optical absorption of AZO thin films .....	81
Figure 5.2	: Optical absorption coefficients of AZO thin films in function of photon energy for different laser parameters.....	82
Figure 5.3	: I-V results of the AZO thin films deposited in 355 nm laser wavelength for sheet resistance: (a) S1 and (b) S2 .....	83
Figure 5.4	: I-V results of the AZO thin films deposited in 532 nm laser wavelength for sheet resistance: (a) S3 and (b) S4 .....	84
Figure 5.5	: Photoluminescence spectra of samples .....	85
Figure 5.6	: Schematics diagram of the Ag/AZO/p-Si/Al structure .....	86
Figure 5.7	: Transmittance of Au films .....	86

Figure 5.8	: I-V characteristic of Au/AZO/Au structure .....	87
Figure 5.9	: J-V characteristic of the Au/p-Si/Al heterojunction with different visible light intensity: (a) semi-log plot and (b) linear plot.....	88
Figure 5.10	: J-V characteristic of S1 with different visible light intensity: (a) semi log plot and (b) linear plot.....	89
Figure 5.11	: J-V characteristic of the S2 with different visible light intensity: (a) semi-log plot and (b) linear plot.....	90
Figure 5.12	: J-V characteristic of the S3 with different visible light intensity: (a) semi-log plot and (b) linear plot.....	91
Figure 5.13	: J-V characteristic of the S4 with different visible light intensity: (a) semi-log plot (b) linear plot.....	95
Figure 5.14	: The ratio of Photocurrent and Dark current ( $I_{ph}/I_d$ ) of the AZO/p-Si heterojunction with different laser parameter in (a) reverse bias and (b) forward bias .....	95
Figure 5.15	: The band diagram of Au/AZO/p-Si heterojunction in reverse bias .....	96
Figure 5.16	: Optical absorption coefficients of AZO thin films in function of photon energy for different laser parameters.....	96
Figure 5.17	: J-V characteristic of the Au/p-Si/Al heterojunction in dark and UV illumination: (a) semi-log plot and (b) linear plot.....	97
Figure 5.18	: J-V characteristic of the S1 with UV illumination: (a) semi-log plot and (b) linear plot .....	98
Figure 5.19	: J-V characteristic of the S2 with UV illumination: (a) semi-log plot and (b) linear plot.....	99
Figure 5.20	: J-V characteristic of the S3 with UV illumination: (a) semi-log plot and (b) linear plot .....	100
Figure 5.21	: J-V characteristic of the S4 with UV illumination: (a) semi-log plot and (b) linear plot .....	101
Figure 5.22	: J-V characteristic of AZO/p-Si heterojunction in dark: (a) linear plot and (b) semi-log plot .....	103
Figure 5.23	: Schematic of the pn junction bandgap and the pn junction in reverse bias.....	105

Figure 5.24	: J-V characteristic of AZO/p-Si heterojunction under illumination: (a) S1 and (b) S2 .....	107
Figure 5.25	: Load line for the photovoltaic mode of the S1: (a) Zoom in (b) overall of the curve .....	108
Figure 5.26	: Load line for the photovoltaic mode of the S2: (a) Zoom in (b) overall of the curve .....	109

University of Malaya

## LIST OF TABLES

Table 1.1: Basic electrical properties of ZnO.....	4
Table 1.2: Resistivity and transparency of doped-ZnO prepared by PLD .....	6
Table 1.3: The dopant and growth techniques for p-type ZnO .....	8
Table 1.4: Deposition techniques for AZO thin films.....	13
Table 2.1: Parameter value of the ZnO/Si heterojunction Bandgap of the Figure 2.11.....	30
Table 3.1: AZO thin films deposition parameter.....	44
Table 4.1: Detailed parameters were used in laser-produced plasma .....	60
Table 4.2: The ablation rate and thickness of AZO thin films .....	64
Table 4.3: Detailed of the AZO thin films roughness in different laser parameter.....	67
Table 4.4: The detailed of the resistivity of the AZO thin films .....	76
Table 4.5: Summary of laser parameters, ions and thin films properties in this work.. ..	79
Table 5.1: Properties of the AZO films used in AZO/p-Si .....	83
Table 5.2: Ratio of the photocurrent with dark current ( $I_{ph}/I_d$ ).....	93
Table 5.3: Ratio of photocurrent $I_{ph}$ / dark current $I_d$ (under UV illumination) .....	102

## CHAPTER 1: INTRODUCTION

### 1.1 Zinc Oxide (ZnO) based materials

Zinc oxide (ZnO) is of main interests in the optoelectronic applications because of its unique combination of properties such as direct and wide bandgap, large exciton binding energy, piezoelectric, luminescence, conductivity, high thermal conductivity, amenability to wet chemical etching and transparent. In addition to the distinct properties, it is also an eco-friendly material. Due to wide abundant source, the cost of ZnO is very low and it is non-toxic.

ZnO is thus a highly promising material to be used in optoelectronics such as transparent conductive oxide (TCO) (Zaharescu et al., 2014), laser-diode (Willander et al., 2009) and pressure transducers (Kuoni et al., 2003). ZnO crystallizes in wurtzite structure in atmosphere, similar to GaN. However, ZnO is more stable in wet etching as compared to the GaN which is important in the design of devices and fabrication. High conductivity and high transparency can be achieved by doping. Aluminium doped Zinc Oxide (AZO) for example, has high potential to replace Indium Tin Oxide (ITO) as TCO where AZO is less expensive, non-toxics and more abundant.

In addition, many of research deposited ZnO on the p-type material such as Si (Ajimsha et al., 2008), CdTe (Khomyak et al., 2013), GaN (Zhu et al., 2008) and AlGaN (Tang et al., 2013) to form heterojunction solar cell, electroluminescence diode and pn junction . However, among the p-type materials, p-Si was the most affordable and most commonly used due to its abundance in nature, cheaper and stable.

### 1.1.1 Structure and Properties of ZnO

ZnO is an II-IV compound semiconductor, with Zn from group II element and O from group IV element. It is an inorganic compound and ceramic material. In general, it has 3 different types of crystalline structure (Morkoç & Özgür, 2009). There is zinc blende, rocksalt and wurtzite crystalline structure as shown in Figure 1.1 The hexagonal wurtzite structure is most common and stable form in ambient condition. There are four Zn ions per unit cell bonding with the four O<sub>2</sub> by covalent bonding whereas the zinc blende only can stabilize it by growing it with the cubic lattice substrates. The rocksalt structure of ZnO is only formed or stable in high pressures condition that is higher or equal 10 Gpa. In this experiment, wurtzite structure of ZnO is used. Figure 1.1 shown the main planar surface of ZnO, grey colour spheres represent Zn atom and black spheres represent O atom.

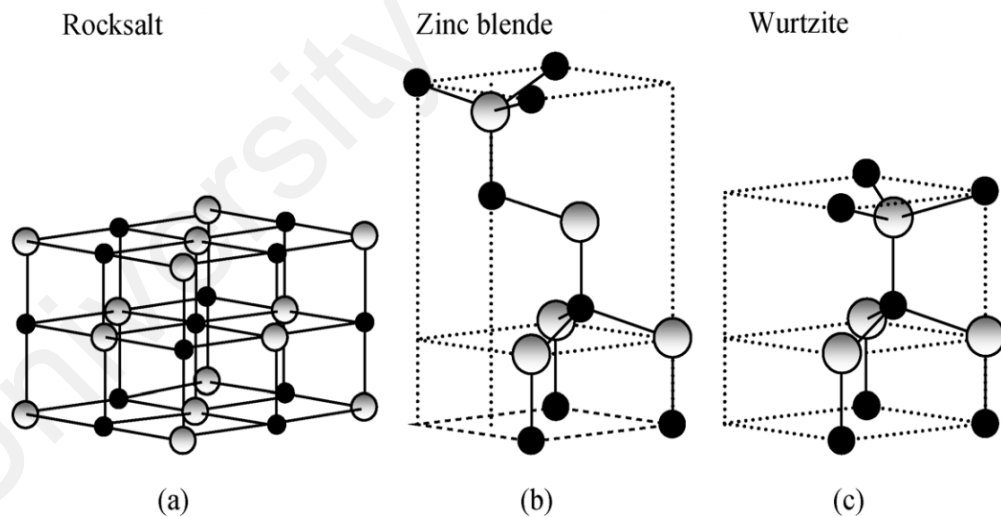


**Figure 1.1:** (a) rocksalt, (b) zinc blende and (c) wurtzite crystalline structures of ZnO respectively.

Wurtzite ZnO has a hexagonal structure along c-axis and with the lattice parameter of a-axis and b-axis which are near or equal to 0.3296 nm and c-axis is near or equal to 0.52065 nm. Hence, the lattice vectors of a-axis and b-axis are perpendicular to c-axis as shown in Figure 1.2.

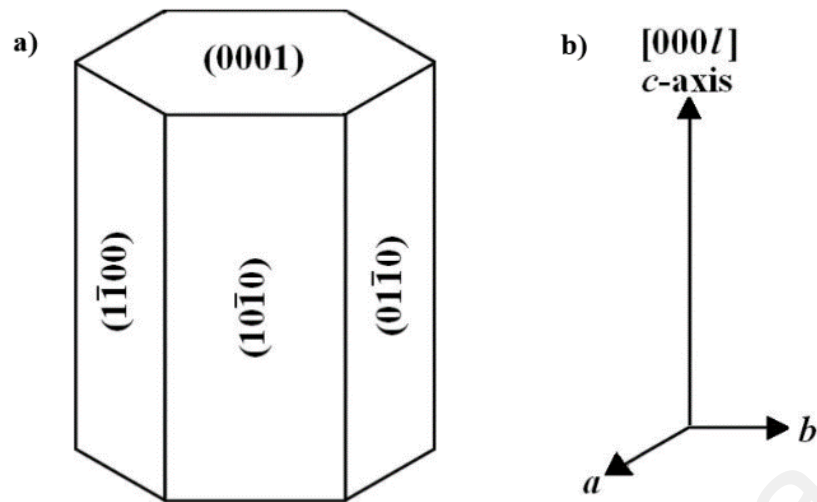


**Figure 1.2:** (a) main planar surface of ZnO and (b) lattice vectors or unit cell axes of ZnO.

Typically, the surfaces orientation of ZnO which include  $(000\bar{2})$  and  $(0001)$  (basal plane),  $(10\bar{1}0)$  and  $(11\bar{2}0)$  (prism planes) and  $(11\bar{2}1)$  (pyramidal plane). The basal plane is the most common surface orientation because it is the most stable structure in ambient condition. Hence, the positive Zn ion  $(0001)$  and negative O ion  $(000\bar{1})$  are usually facing opposite side by each other, resulting a normal dipole and spontaneous polarization effect as well as divergence in energy surface of wurtzite ZnO. The other two surface prism planes and pyramidal plane are non-polar surface so they are lower surface energy when compare to the basal plane.

### 1.1.2 Electrical Properties of ZnO

The electrical properties of ZnO are determined by the electron transport or mobility of the electron in the ZnO material. The electron transport of ZnO samples can be measured by Hall Effect and electron transport must be considered in low or high magnetic field. In low electric field, the ohm's law is obeyed. However, when the electric field is increased to certain threshold, the electron distribution function is changed; the scattering rate of electron is increased. The electrons become hot electrons when electron temperature is higher than the lattice temperature, and the mobility of the electron

decreases (Butcher & Hearn, 1969). The electrical properties of ZnO in low electric field are shown in Table 1.1:

**Table 1.1:** Basic electrical properties of ZnO (Coleman & Jagadish, 2006).

Property	ZnO
Direct bandgap energy (eV)	3.37
Electron mobility (cm <sup>2</sup> /V.s)	205
Hole mobility (cm <sup>2</sup> /V.s)	5.5
Electron effective mass	0.24 m <sub>0</sub>
Hole effective mass	0.59 m <sub>0</sub>
Exciton binding energy (meV)	60

### 1.1.3 Optical Properties of ZnO

The bandgap of undoped ZnO is 3.37 eV at room temperature and the lowest point of the conduction bands (CB) is directly above to the highest valence bands (VB) in ZnO, they are at the same point in the hexagonal Brillouin zone (Figure 1.3) which results in direct transition. Among the group II-IV elements, the ionization energy of oxygen of ZnO is the highest and this leads to strongest interaction between Zinc 4s and Oxygen 2p-orbit. The empty 4s states of Zn<sup>2+</sup> is the lowest conduction band and the upper most conduction band is at Zn 4p state whereas the highest valence bandgap is originated by the binding sp<sup>3</sup> orbitals or 2p orbitals of O<sup>2-</sup>. The lowest valence band is at Oxygen 2s state. Due to the hexagonal crystal field, the binding sp<sup>3</sup> orbitals split without spin into two states which are  $\Gamma_5$  and  $\Gamma_1$ .

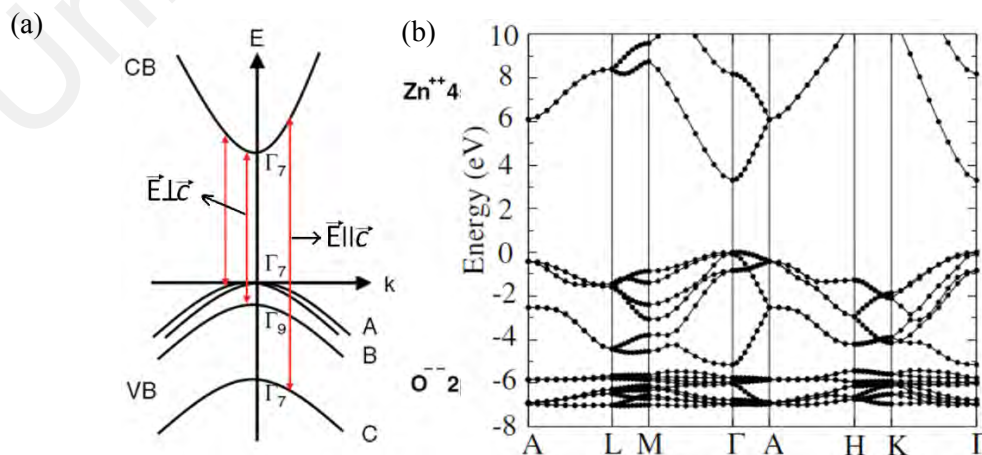


**Figure 1.3:** (a) ZnO valence and conduction bandgap (Klingshirn, 2007) and (b) Valence band maximum was set to zero (Janotti & Van de Walle, 2009).

ZnO crystal is transparent in the visible and IR (400 nm to 2000 nm). Its refractive index is around 1.93 to 2. The refractive index of bulk ZnO is slightly higher than ZnO films. It shows electro-optical properties and vice versa. The electro-optical properties of ZnO are based on the intrinsic and extrinsic defect. Intrinsic defect of ZnO is referred to the optical transition between the CB and VB while the extrinsic defect is related to the level created by dopant. Intrinsic defect of ZnO such as oxygen vacancies ( $V_o$ ), Zinc Vacancies ( $V_{zn}$ ), Oxygen interstitial ( $O_i$ ), Zinc interstitial ( $Zn_i$ ) and oxygen or zinc anti-site which all make the ZnO a promising material for deep level emission (DLE). The green luminescence of ZnO is caused by the ionized oxygen vacancies (Bhaskar et al., 2009; Cao et al., 2006). In addition, the electronic transition between the deep acceptor and the shallow donor in ZnO cause the green luminescence (Rodnyi & Khodyuk, 2011; Zhang et al., 2015) as shown in Figure 1.4.

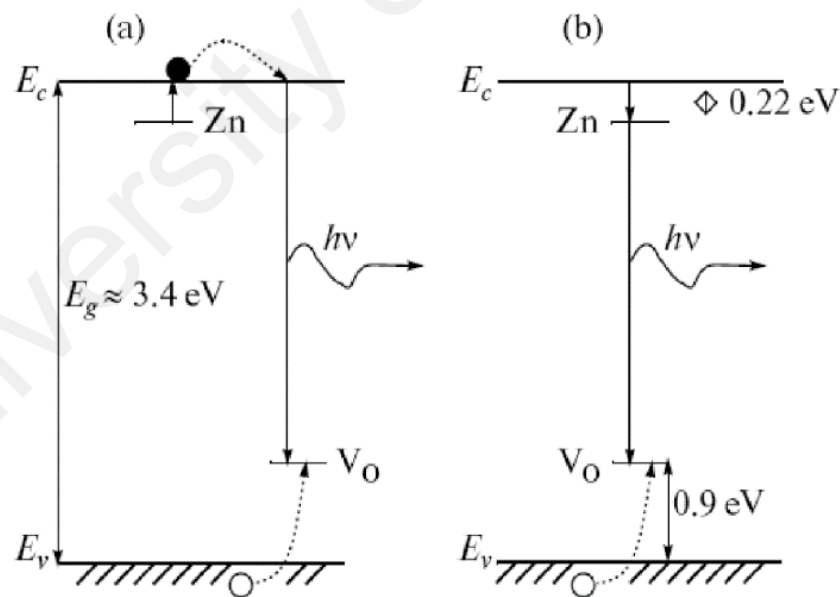


**Figure 1.4:** Level position and electronic transitions responsible for the green luminescence (a) 300 K temperature and (b) less than 50 K temperature (Cao et al., 2006).

The red luminescence from ZnO occurred in the case of zinc-rich growth where the formation energy of oxygen vacancy is lower than the zinc interstitial. As a result, the red luminescence of ZnO arises because of the double ionized oxygen vacancies

In summary, the wide bandgap of ZnO (3.37 eV) makes ZnO a highly potential material for photonic application in UV or blue spectral region. Due the large exciton-binding energy of ZnO, ZnO able to has efficient excitonic emission at room temperature. The UV emission is caused by the recombination of free excitons (near band-edge of ZnO).

#### 1.1.4 Doping of ZnO

In order to improve and to obtain a new multifunction of ZnO, dopant is introduced. A lot of methods can be used for doping such as diffusion (Kulczyk-Malecka et al., 2011), ion implantation (Kohiki et al., 1994) and epitaxial growth (Kim et al., 2002). N-type of ZnO can be easily obtained by either native or extrinsic donor whereas p-type ZnO still a challenge.

In order to obtain highly conductive and transparent ZnO film, Group III element such as aluminium (Al), gallium (Ga), and Indium (In) are used as dopant for ZnO. Table 1.2 shows the resistivity and the transparency of ZnO after being doped with different element. Among the dopants, the Aluminium doped ZnO thin films (AZO) have low resistivity and high transparency. The AZO sample in Table 2.2 is deposited by 266 nm laser and low fluence (1 J/cm<sup>2</sup>). In this thesis, 355 nm and 532 nm laser ( $\geq 2$  J/cm<sup>2</sup>) are used for deposition.

**Table 1.2:** Resistivity and transparency of doped-ZnO prepared by PLD (Liu et al., 2013).

Dopants	Optimum content in target (%)	Thickness (nm)	Resistivity ( $\Omega$ -cm)	Transmittance (%)
Al	2	500	$4.5 \times 10^{-4}$	88%
Ga	5	200	$8.12 \times 10^{-4}$	>90%
In	40	>1000	$4.02 \times 10^{-4}$	>85%
F	2	200	$4.83 \times 10^{-4}$	>90%
Si	2	~150	$6.2 \times 10^{-4}$	~80%

When ZnO is heavily doped, blue shift will occur that increases the total optical bandgap of doped-ZnO. Optical bandgap shift is affected by two effects; they are Burstein-Moss effect (BM) and Bandgap Narrowing effect (BGN) as shown in Figure 1.5. The BM effect is the phenomenon caused by heavy doping. The absorption edge of doped-ZnO is shifted to higher energies as the carrier concentration increased to a threshold level. As a result, the Fermi level is higher than the lowest energy band of conduction or inside the conduction band. Equation 1.1 represents the relationship between the BM effect and electron effective mass ( $m^*$ ): (Kang & Joung, 2013)

$$\Delta E_g = \left( \frac{h^2}{8m^*} \right) \left( \frac{3}{\pi} \right)^{2/3} n^{2/3} \quad (1.1)$$

where  $\Delta E_g$  is the shift bandgap of the doped-ZnO refer to the undoped ZnO,  $h$  is the Plank's constant. The second effect of heavy doping in ZnO; BGN effect is narrowing the bandgap by the electrostatic interaction force between ionized impurities and free electron.

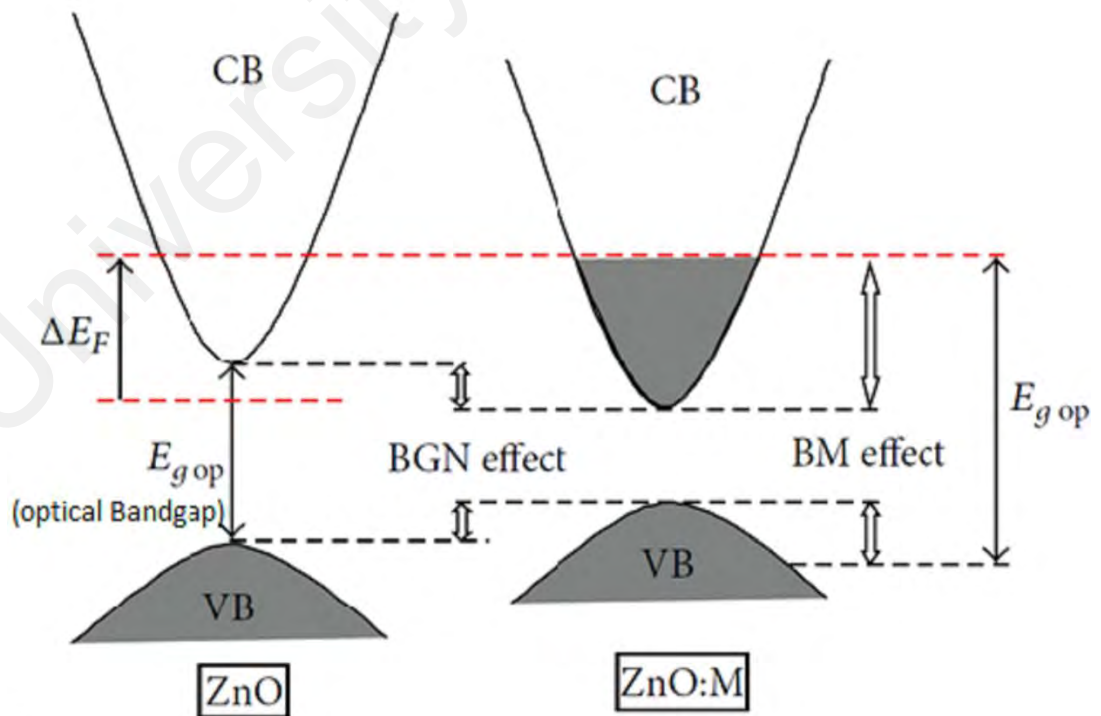


**Figure 1.5:** The optical bandgap of undoped ZnO on left and doped ZnO on right, this image gained from (Liu & Lian, 2007).

P-type ZnO can be obtained by doping with acceptors such as Group I element (Li, Na, K) which introduces shallow acceptor level. Li-doped ZnO, for example, has shown a high resistivity but Li-doped ZnO didn't show p-type conductivity at room temperature. The challenges to produce the p-type ZnO may be due to several reasons (Wei et al., 2008), including the followings:

- Acceptors are less soluble than the threshold achievable donor concentration.
- Charge carrier generated are not enough at working temperature due to the defect transition energy levels are too deep.
- Larger bond than Zn-O bond that causes the lattice strain, lattice strain may lower the formation energy of the native donor defect.
- Acceptors may have natural tendency to pair with native defects which may form electrically inactive complexes.

In order to solve the problems mentioned above, Group V elements (N, As, P) were studied, some examples are shown in Table 1.3

**Table 1.3:** The dopant and growth techniques for p-type ZnO (Maksimov, 2010).

Dopant	Growth Technique	$N_A$ (cm <sup>-3</sup> )	$\mu$ (cm <sup>2</sup> / V s)	$P$ (Ohm cm)
N	CVD	1.06x10 <sup>18</sup>	0.34	17.3
N	CVD		ZnO:N remained n-type	
P	Diffusion		ZnO:P layer was p-type	
P	Sputtering	1.9x10 <sup>16</sup> - 3.8x10 <sup>19</sup>	6.9 - 40.1	0.02 - 8.1
As	PLD	10 <sup>18</sup> - 10 <sup>21</sup>	0.1 - 50	10 <sup>-5</sup> - 10
As	Sputtering	9x10 <sup>19</sup>	4	-
As	PLD	2.4x10 <sup>17</sup> - 1.1x10 <sup>18</sup>	-	2.2 - 6.7
As	CVD	1.45x10 <sup>18</sup>	1.92	2.3
As	PLD	4x10 <sup>19</sup>	2	0.05
Sb	MBE	1x10 <sup>16</sup>	10	6
Sb	PLD	1.9x10 <sup>17</sup>	7.7	4.2
Li	PLD	6.04x10 <sup>17</sup>	1.75	5.9
N + As	CVD		Mixed conductivity	
N + Al	Sputtering	2.52x10 <sup>17</sup>	0.43	57.3
N + Al	Sputtering	1.45x10 <sup>18</sup>	1.62	2.64
N	PLD		8	
Ag	PLD	4.9x10 <sup>16</sup> - 6.0x10 <sup>17</sup>	0.29 - 2.32	34 - 54
Bi	MBE		ZnO:Bi remained n-type	

## **1.2 Application of ZnO based thin films**

ZnO is a semiconductor which possesses a large of interesting properties such as direct and wide bandgap (Morkoç & Özgür, 2009), large exciton binding energy, piezoelectric (Kuoni et al., 2003), high transparency and high conductivity (Zaharescu et al., 2014). In this section, the applications of ZnO are discussed.

### **1.2.1 UV light source and detector**

The bandgap of ZnO is 3.37 eV at room temperature and its free-exciton binding energy is 60 meV. Such wide bandgap are very suitable used in UV light-emitting diode (Rodnyi & Khodyuk, 2011), solar cell (Hussain et al., 2015a) and photodetector (Ghosh et al., 2016). Direct and wide bandgap makes the ZnO able to luminesce in the UV or blue photon and the large exciting binding energy makes the ZnO less thermal noise at room temperature. For the photodetector and solar cell, the photocurrent (electron-hole pair) will be generated when the ZnO photodetector or solar cell exposed to the UV light.

### **1.2.2 Transparent conducting oxide**

TCOs require high electrical conductivity around  $10^{-3}$   $\Omega\text{cm}$  to  $10^{-4}$   $\Omega\text{cm}$  and high optical transmittance above 80 % in visible region, and high reflectance in infrared region (Edwards et al., 2004) . The main material for TCO currently; Indium Tin Oxide (ITO) has a lot of disadvantages such as the concern in toxicity, shortage of indium globally and high cost. Doped-ZnO has been suggested as replacement for ITO (Cranton et al., 2016; Liu et al., 2013). Compare with the ITO, doped-ZnO are more stable, higher in thermal stability, less expensive, non-toxics, good resistance against damage by hydrogen and more abundant (Pandey et al., 2012).

### 1.2.3 Piezoelectric sensors

Piezoelectric material generates electricity when experience to the mechanical stress and vice versa. Piezoelectric material is usually used as mechanical sensor (Lee & Chiu, 2015) , transducers (Hsu et al., 2008) and actuator (Zhao et al., 2004). ZnO has the property of piezoelectric, due to the electromechanical coupling and low symmetry of the wurzite crystal structure of ZnO (Janotti & Van de Walle, 2009).

### 1.2.4 ZnO/Si heterojunction optoelectronics

ZnO can be used as a window layer or antireflection coating when it is grown on Si to form ZnO/Si heterojunction. Both of the materials are abundance and non-toxic. In addition, the refractive index ZnO is near to Si. Therefore, ZnO/Si heterojunction can be used in the integration of the opto-electronics device. Some examples are briefly described as followed.

As mentioned above, the properties of ZnO fulfil several important requirements for solar cell such high transmittance in visible and IR region, high absorption energy in the structure, chemical stability and the most important is adhesion to Si. ZnO/Si heterojunction solar cell consisted of a larger bandgap (bandgap of ZnO) on a single crystal silicon wafer. ZnO/Si heterojunction is defined as a mono-junction solar cell; it can maximize to collect the light energy because it has double band structure: ZnO has wide bandgap while Si has smaller bandgap. On top of being the antireflection layer, ZnO can absorbs the high photo energy (UV region) whereas the low photo energy is absorbed by p-Si (Wei-Ying et al., 2008). The basic structure of the ZnO/Si is shown in the Figure 1.6.

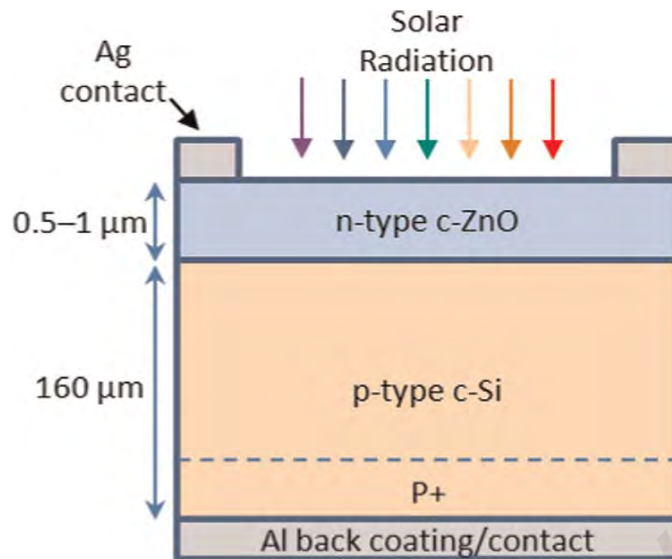


**Figure 1.6:** Schematic of ZnO/P-Si heterojunction solar cell (Hussain et al., 2015b).

Si-based photodiodes have been continuously developed due to Si is an abundance and non-toxic material. However, Si-based photodiodes are only high sensitive to visible and infrared radiation. Its responsivity for the UV spectrum is still inefficiency (Lee et al., 2003). Thus, group II-IV wide bandgap material are chosen to increase the responsivity and stability of UV photodiodes as well as due to their intrinsic visible-blindness properties (Wang et al., 2005). According to the previous report (Chen & Tien, 2010), ZnO was deposited on the Si as antireflection window for Si-based photodiodes as shown Figure 1.7. The barrier potential and carrier-depletion would build up between the ZnO and Si junction. Low energy may be collected at the Si depletion side whereas UV energy may be absorbed at ZnO side. Photoelectric response can be improved in ZnO/Si heterojunction by a good interface (pn junction) to avoid leakage current and good ZnO film for the light transmission for carrier transport.

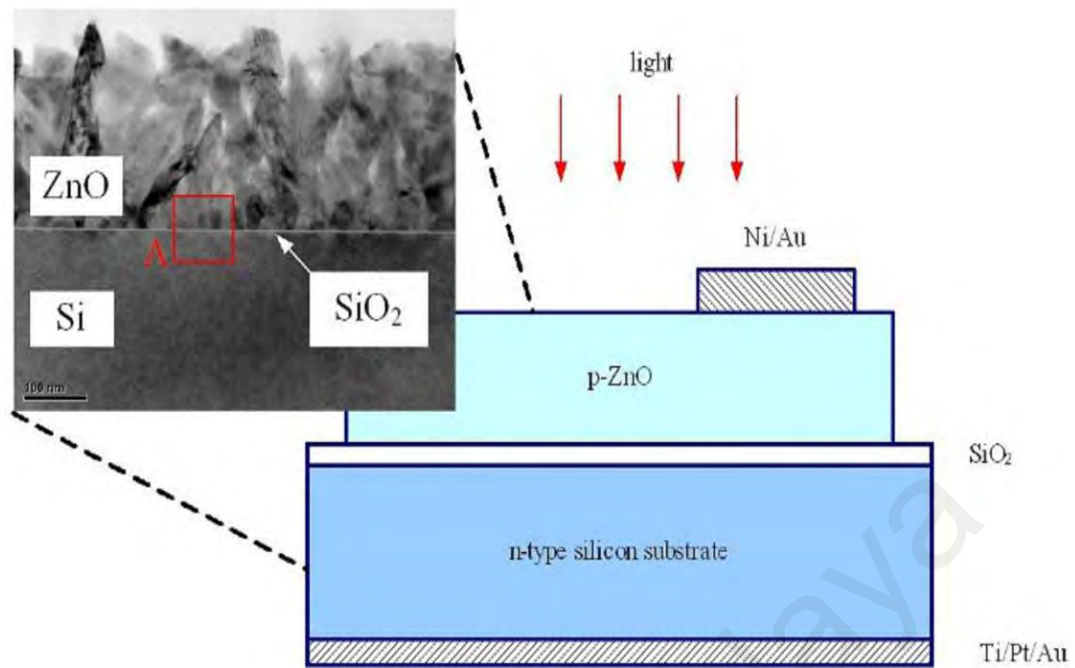


**Figure 1.7:** Schematic cross section of the complete structure of ZnO/Si –based photodiode (Chen & Tien, 2010).

### 1.3 Deposition methods of ZnO

ZnO thin films have been fabricated by various deposition techniques started from early 1980s (Table 1.4).

**Table 1.4:** Deposition Techniques for AZO thin films.

Deposition Techniques	References
DC Magnetron Sputtering	Eshaghi & Hajkarimi, 2014; Isherwood et al., 2015; Ko et al., 2005. Li et al., 2012; Murdoch et al., 2009; Samwel et al., 2015; Yao et al., 2013; Zhu et al., 2013
RF Magnetron Sputtering	Chey et al., 2009; Chang et al., 2013; Duygulu et al., 2014; Fernandez & Naranjo; 2010;

**Table 1.4, continued.**

---

	Isherwood et al., 2015; Miao et al., 2014; Wang et al., 2013; Tamiko et al., 2016
Pulsed Laser Deposition	Cao et al., 2014; Dosmailov et al., 2015; Gu et al., 2011; Girtan et al., 2013; Inguva et al., 2015; Kaur et al., 2015; Kang & Joung, 2013; Wong et al., 2013
Chemical Vapour Deposition	Johnson et al., 2013; Kim et al., 2011; Mohanta et al., 2014
Spray pyrolysis	Johnson et al., 2013; Mohanta et al., 2014; Kim et al., 2011
Atomic Layer Deposition	Gong et al., 2013; Yuan et al., 2012

---

### **1.3.1 Spray pyrolysis**

Spray pyrolysis is an inexpensive technology. The ionic solution is containing element of Al, Zn, alcohol and DI water (Kaid & Ashour, 2007). These elements are stored inside the precursor solution reservoir. During the deposition, the ionic solution will be sprayed onto the substrate surface. After that, samples will be heated at 450 °C (Kaid & Ashour, 2007) in the normal atmospheric condition as shown in Figure 1.8. A desired solid film such as AZO is formed after the deposition process.

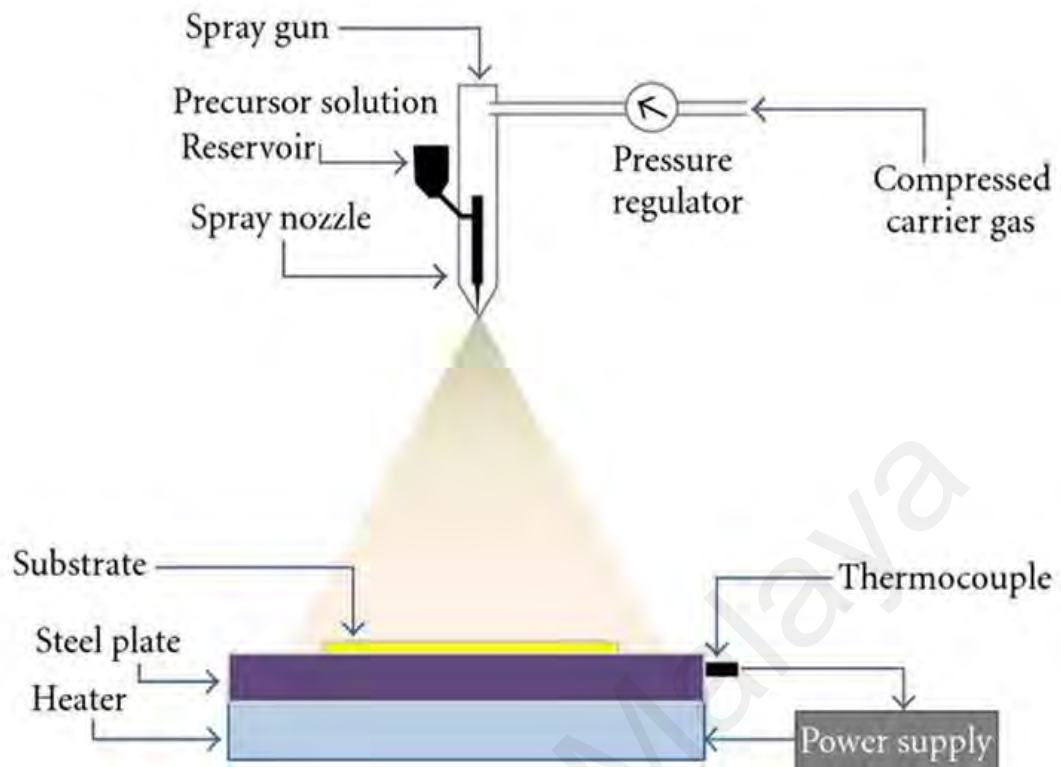


**Figure 1.8:** Schematic diagram of basic spray pyrolysis deposition system (Jarzebski, 1982) .

### 1.3.2 Chemical Vapor Deposition (CVD)

CVD is a widely used technology for deposition, the majority of its involved thin film coating such as AZO. However, it is also used to produce high purity bulk material. The basic working principle of CVD starts from the gaseous precursors. Then, the gaseous precursors are flown into the chamber with the desired atmosphere to be coated onto the heated object. The precursor gases are first decomposed on the surface of the substrate and transport through the surface. The growth involves the process of adsorption, diffusion and decomposition. As a result, the final thin film is produced as shown in Figure 1.9. During the deposition, homogenous chemical reactions will occur between the precursor gases and the surface of the substrate. The unwanted gas products will be removed by the gas flow.

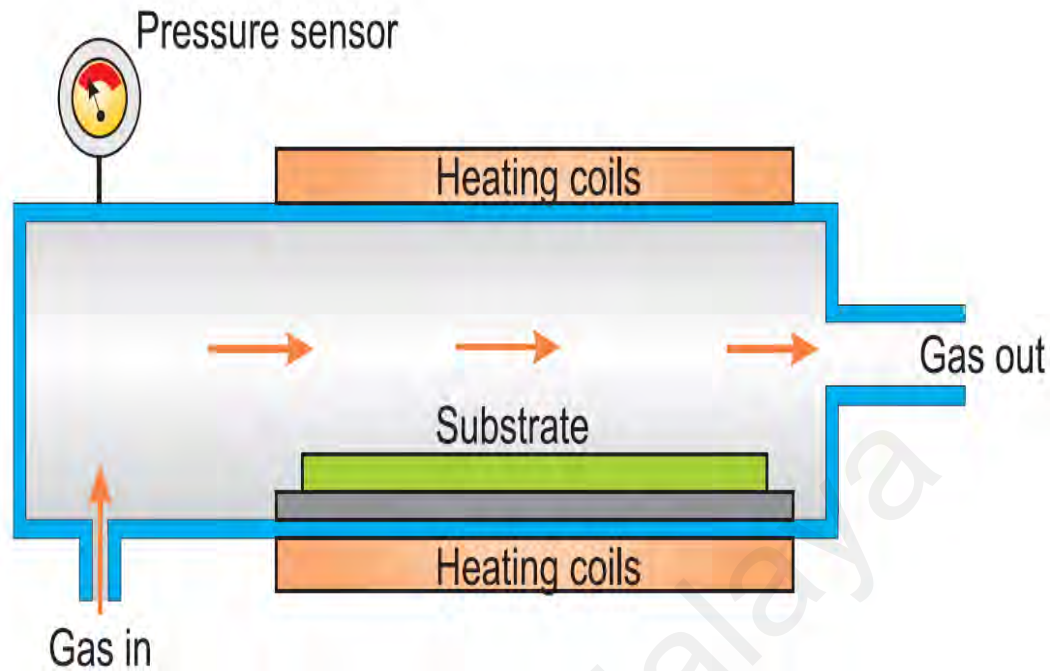


**Figure 1.9:** Schematic diagram of CVD system (Lei, 2004).

### 1.3.3 Sputtering Deposition

Sputtering deposition technology is the physical deposition process as it does not involve any chemical reactions. Sputtering is suitable to be used for high melting temperature material. The arrangement of plasma chamber is an important step to achieve a high density of ions for coating. The target acts as cathode whereas the substrate acts as anode. During sputtering, electrically neutral Argon atom are introduced into a vacuum chamber (1 to 10 mTorr). Argon atom are ionized by a dc voltage between the target and substrate, resulting a plasma is created. These Argon ions are now charged and they are accelerated to the anode target. The target is bombarded by the energetic  $\text{Ar}^+$  ions. The atoms on the surface of the target will be knocked out and the atoms will be transported to the substrate, resulting deposition of the thin film as shown in Figure 1.10.

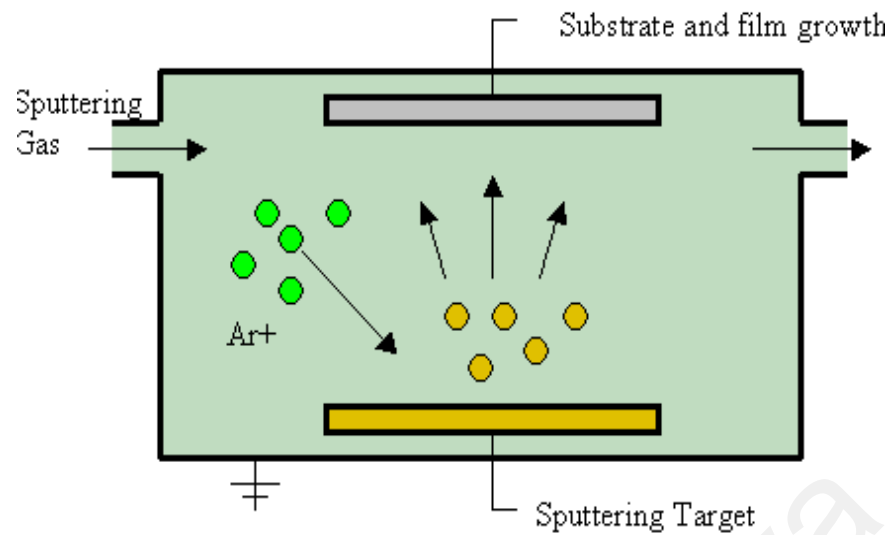


**Figure 1.10:** Schematic diagram of sputtering process system.

### 1.3.4 Atomic Layer Deposition (ALD)

In ALD, materials are deposited onto the substrate layer by layer. ALD used two precursors: gases and vapours onto the surface of the substrate and subsequent chemisorption of the precursor's gases. The deposition cycle is repeated and atomic layer are formed layer by layer until the desired film thickness is gained as shown in Figure 1.11.

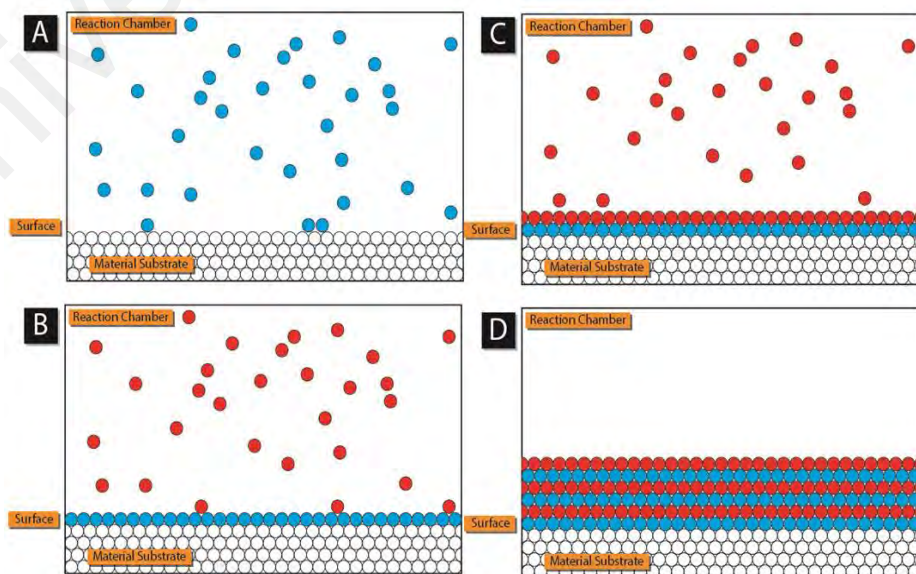


**Figure 1.11:** Schematic diagram of the ALD process. (a) precursor A(blue), (b) precursor B(blue), (c)precursor A and B and (d) desired film (George, 2009).

Firstly, the precursor A(blue) is added into the reaction chamber and deposit on the surface of the substrate. After precursor A has adsorbed and bond with the surface, the second precursor B(blue) is added sequentially and bonding with the precursor A. This process is repeated until a desired film is achieved as shown in Figure 1.11(d).

### 1.3.5 Pulse Laser Deposition (PLD)

PLD is a versatile physical vapor deposition technique to deposit thin films. Low resistivity and high transparency AZO films have been grown by PLD (Agura et al., 2003; Matsubara et al., 2003; Suzuki et al., 1996). In 2015, ZnO have been successfully deposited on the polymer by PLD (Dosmailov et al., 2015), which permit PLD able to deposit material at room temperature. PLD has shown advantages in depositing multi-element oxides and superconducting films as compared to other deposition method such as CVD, chemical bath deposition and spray pyrolysis (Chattopadhyay, 2009). PLD is also capable of stoichiometric transfer of the target material to the resultant film (Zhang et al., 2015; Guo et al. 2009; Hu & Tang et al. 2012). The schematic diagram of a typical PLD setup is shown in Figure 1.12.

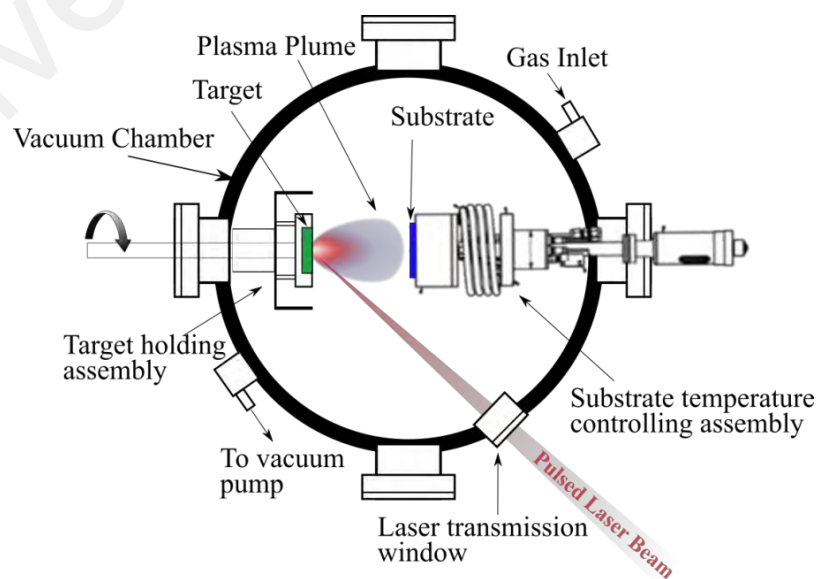


**Figure 1.12:** Schematic of Pulsed Laser Deposition System (Radziemski & Cremers, 1989).

The film growth in PLD is highly influenced by the deposition parameter such as laser wavelength, laser fluence and substrate temperature. The target materials are first ablated or ejected, move towards the substrate surface and finally adsorb on the substrate surface. After that, the species on the substrate surface so-called adatom, are diffused to some distance before they react each other. The adatoms will undergo nucleation when they collide to each other and form clusters. Adatoms nucleation will determine the morphology and topology of the growing thin film. There are 3 types of growth modes of the film in PLD, they are: 2D layer-by-layer growth (Frank-van der Merwe), 3D island growth (Volmer-Weber) and layer-by-layer followed by an island growth (Stranski-Krastanov) as shown in Figure 1.13. The growth mode depends on the thermodynamics that related surface energy between the substrate and film where the free energy of the surface and the interface (substrate and film) are minimized. Frank-van der Merwe mode is the full monolayer growth. Thin film growths in Frank-van der Merwe (Mishra et al., 2014) involves complete coalescence before the cluster are growth on the next film layer. The growth species in Frank-van der mode have high mobility on a surface where the high mobility maybe gained from the substrate surface temperature or kinetic energy of the arriving species. A good lattice match between the substrate and film is also necessary in this mode. Volmer-weber mode growth (Floro et al., 2001) occurs when the species in a growing film are more strongly bound to each other than to the substrate thereby forming cluster. On the other hand, Stranski-Krastanov (Baskaran & Smereka, 2012) mode occurs when the full monolayer growth is incomplete and change to the 3D-island growth. The thin film grows in Starnski-Krastaanoy mode may due to the lattice mismatch between the surface of substrate and film.

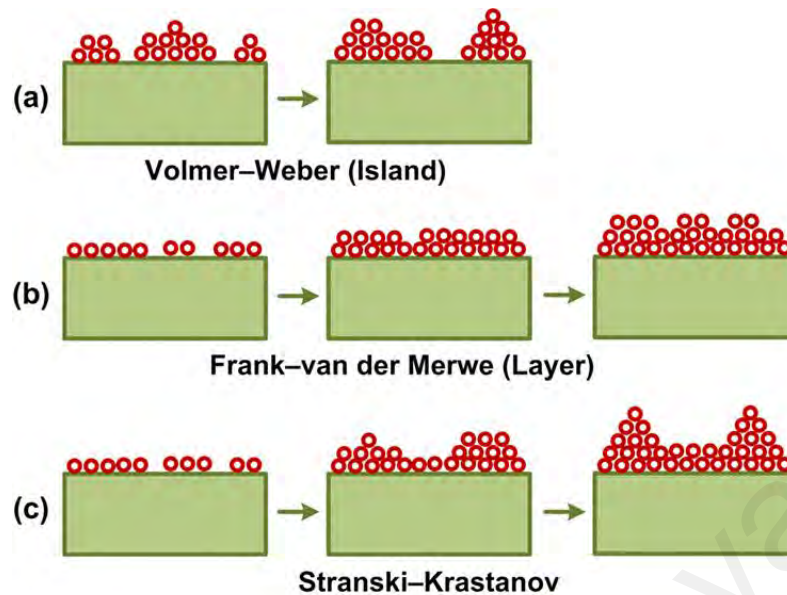


**Figure 1.13:** Schematic illustrating three different growth modes (a) 3D island growth (Volmer-Weber), (b) 2D layer-by-layer growth (Frank-van der Merwe) and (c) layer-by-layer followed by an island growth (Stranski-Krastanov).

#### 1.4 Project Objectives

This project aimed to study the deposition and growth of Al-doped ZnO thin films on glass or silicon by PLD. The main objectives are:

1. To investigate the growth of Al-doped ZnO film by PLD technique
2. To study the properties of AZO film for optoelectronic device application

#### 1.5 Problem Statement

Although pulsed laser deposition has been used in the deposition of various oxide films, the laser-produced plasma that influences the growth has not been widely investigated. In particular, the plasma characteristics that are responsible for the growth of ZnO have not been deeply studied. The relation between plasma plume and ZnO properties are important in understanding the growth and thereby controlling the films' properties for various applications. In the current work, the parameters of laser energy and the background environment for plasma formation are investigated and are optimized by considering the results of AZO thin films such as XRD, SEM, AFM, optical

transmittance and resistivity. The optimized parameters are used for the fabrication of AZO/p-Si heterojunction.

## **1.6 Thesis Outline**

Chapter 1 provides an introduction of ZnO, applications and the deposition methods of ZnO. Chapter 2 reviews on the Al-doped ZnO by PLD and the effects of various parameters and the plasma processes involved. The detail of the experiment set up for PLD is described in Chapter 3.

The results and discussion of the work are reported in Chapter 4 and 5. In Chapter 4, the effects of laser parameters on the plasma plume and the properties of AZO thin film are presented. The characteristics and properties of AZO/p-Si heterojunctions are reported in Chapter 5.

Finally, a summary and conclusion of the project are presented in Chapter 6

## CHAPTER 2: LITERATURE REVIEW

### 2.1 Introduction

Al-dopant improves the electrical and optical performance of ZnO. In PLD, Al-doped ZnO (AZO) can be grown by deposition from an Al-doped ZnO target. Plasma plume consisting of the Al, Zn, O are formed subsequently. Finally, materials growth occurred on the substrates are placed. Thus, the conditions in deposition of AZO such as percentage of Al-dopant, temperature of substrate, pressure and laser fluence play importance role in quality or performance of AZO. In addition, plasma diagnostic can be used to reveal the dependence of AZO films properties on the plasma species.

### 2.2 PLD of AZO

Among the group (III) elements dopant for ZnO, Al is the most common and popular because AZO thin films show the lowest electrical resistivity (Alauddin et al., 2010). Al-dopant improve the electrical and optical performance of ZnO in electrical and optical. PLD method as introduced in Chapter 1.3.5 has shown to be versatile for the deposition of various oxide films. The parameters such as laser energy, background gases and substrate temperature play important roles in optimize the quality of AZO thin films.

#### 2.2.1 Effects of dopant concentration in AZO

After Al doped into ZnO,  $\text{Al}^{3+}$  ion will substitute or replace the  $\text{Zn}^{2+}$  ion sites and result in the increase of carrier concentration. Hence, one electron will be donated and added to the conduction band. Figure 2.1 shows the effect of the amount of Al dopant in AZO on the electrical properties. The resistivity of AZO decreased when the amount of dopant increased until 2 wt.% of Al; and the resistivity increased as the percentage of Al-dopant increase further. An optimum level of dopant is observed because as the carrier

concentration increases above a critical level, the carrier mobility of carrier decreased due to the scattering processes such as ion scattering and grain boundary scattering.

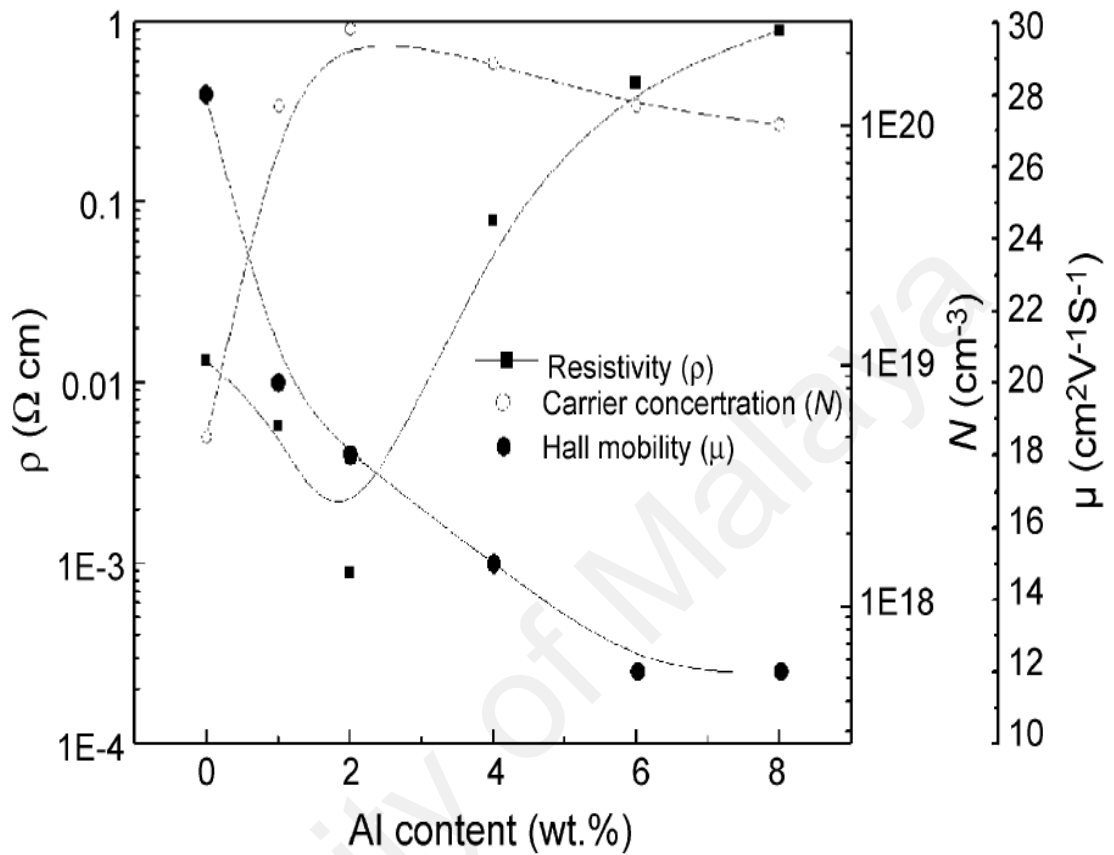


**Figure 2.1:** The electrical properties of AZO in different percentage dopant. (Liu & Lian, 2007).

Figure 2.2 represents the transparency of AZO in different percentage of Al dopant. All the AZO films have an average optical transparency above 80 %. However, when the dopant concentration increases, the optical absorption is shifted to high energy or short wavelength. This phenomenon can be explained by BM effect as mention in Chapter 1.

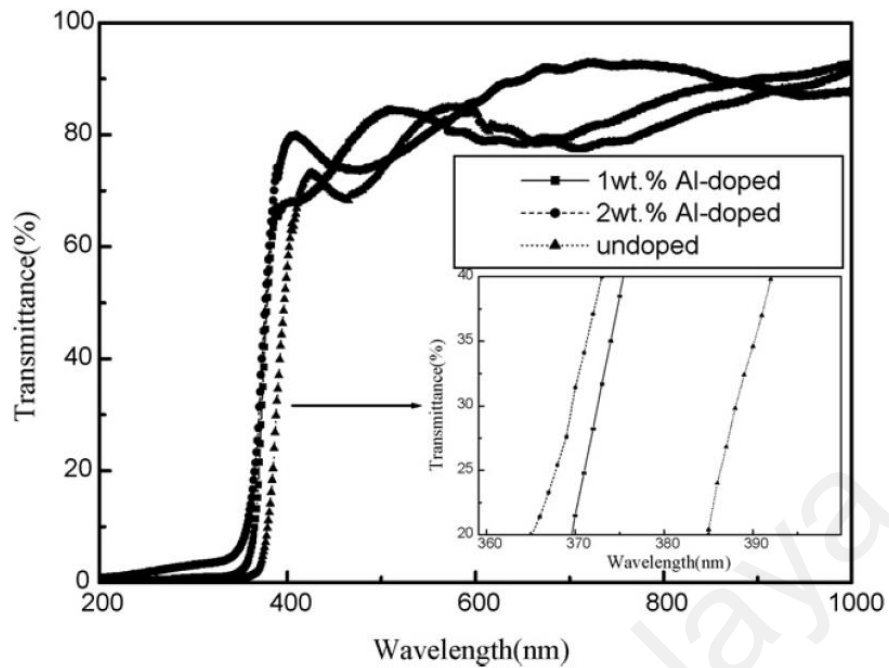


**Figure 2.2:** The optical transparency of AZO in different percentage of Al-doped and undoped ZnO films (Liu et al., 2009).

### 2.2.2 The Effects of Laser Wavelength and Energy in PLD growth of AZO

Laser wavelength and laser fluence affect the ablation process when laser interacts with the target material. Shorter laser wavelengths provide photons with high energy that result in smaller laser penetration depth. It was first shown that 248 nm laser produced ZnO films with lowest resistivity of  $8.54 \times 10^{-5} \Omega\text{cm}$  among all deposition methods (Agura et al., 2003). In another report, the comparison of ArF laser (193 nm) and KrF laser (248 nm) shown that 193 nm laser led to good quality crystal structures in the samples (Valerini et al., 2008). 355 nm laser has also been used for the growth of AZO films where resistivity in the range of  $10^{-3} \Omega\text{cm}$  were obtained (Holmelund et al., 2004).

On the other hand, Craciun observed different morphology in the samples grown at 248 nm and the samples grown at 532 nm (Craciun et al., 1995). Columnar growth was obtained by using 248 nm laser but nonuniform crystals growth was detected when 532 nm laser is used. The presence of particulates was also detected in the deposition by 532 nm laser (Yap et al., 2016).

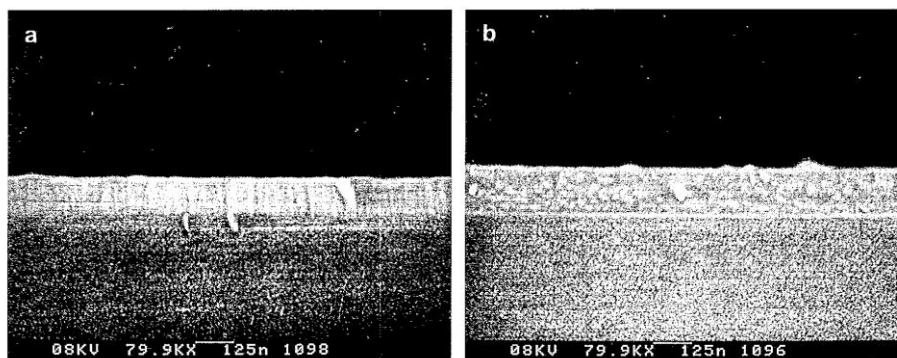


**Figure 2.3:** SEM micrographs of the films deposited by (a) 248 nm laser and (b) 532 nm laser (Craciun et al., 1995).

A low laser fluence may decrease the deposition rate of the thin film and at the same time, unable to ablate some materials from the target. Thus, there is always a threshold laser fluence for deposition. For AZO, the laser fluence used is typically  $> 1 \text{ J/cm}^2$  to ensure sufficient ablation. The growth rate of the films typically increased with laser fluence when more materials are ablated. However, if the laser fluence is too high, phase explosion and particulates generation may occur and affect the films quality. The phase explosion is also depending on the laser wavelengths and kind of target. Thus, an optimum laser fluence is always observed, where the films' growth occurs at a satisfactory rate and the morphology of the films are good. Figure 2.4 shows the resistivity of AZO deposited by 248 nm laser wavelengths and 355 nm laser wavelength with different laser fluence.

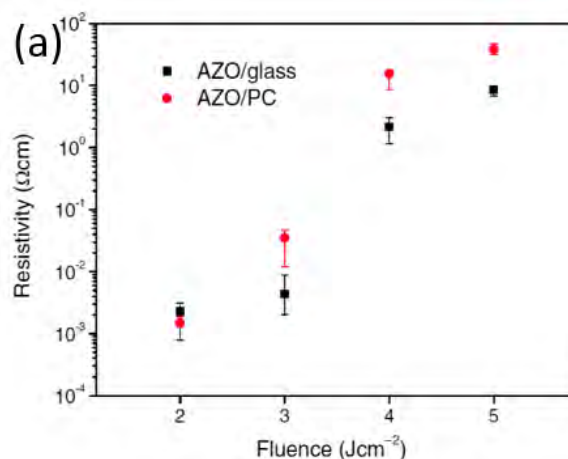


**Figure 2.4:** Graph of resistivity versus different laser fluence for AZO film with two different laser wavelength (a) 355 nm (Tan et al., 2014) (b) 248 nm (Agura et al., 2003).

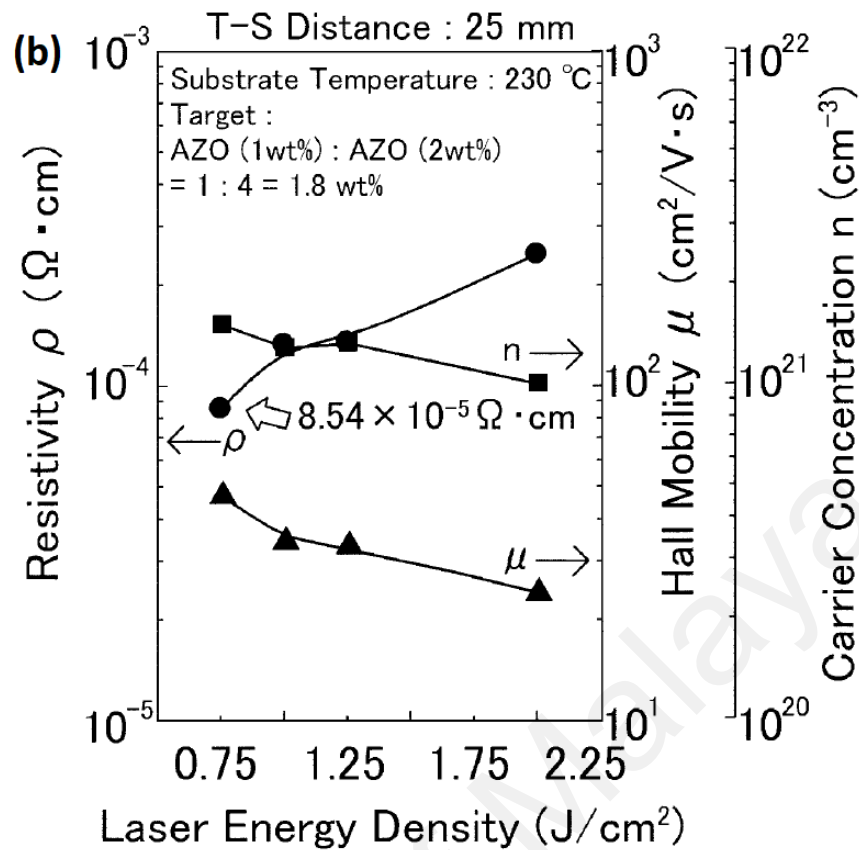


Figure 2.4, continued.

As shown in Figure 2.4, highest laser fluence results in AZO films with the highest resistivity. Thus the best laser fluence was  $2 \text{ J/cm}^2$  (Tan et al., 2014). At lower laser fluence ( $< 2 \text{ J/cm}^2$ ), the growth is too low, indicating that the laser fluence is insufficient for ablation of the target. In addition, the ablated adatoms such as  $\text{Al}^{3+}$ ,  $\text{Zn}^{2+}$  and  $\text{O}^{2-}$  may be unable to reach the surface of the substrate because of low kinetic energy. When the laser energy was increased, the resistivity of the AZO thin films was increased. Based on the research of the Tan et al., 2014 and Girtan et al., 2013, the roughness and the grain size of the thin films increase as the laser fluence increase. High roughness morphology and the larger grain size of the thin film reduce the mobility of the carriers by scattering. Lower mobility of carrier results in higher resistivity.

### 2.2.3 The effects of Oxygen background gas in the growth of AZO films

In general, oxygen is often used in the growth of oxide in order to compensate oxygen loss from the target. If the substrate is heated at high temperature, oxygen background gas also takes part in the growth. In addition, oxygen act as a collision gas which collide with the ablated species and control the kinetic energy of ablated species (Thestrup & Schou, 1999).

If the kinetic energy of the ablated species is too high, the species will knock out the atom from the growing films instead of deposition. The second possible mechanism is the ablated species penetrate into substrate. Thus, the presence of oxygen in the background moderates the flow of ablated species towards the substrate. However, if the oxygen pressure is too high the atoms from the target are unable to reach the surface of substrate. Hence, it is a critical to optimize the oxygen pressure for good crystalline growth. As shown in Figure 2.5, when the pressure increases the resistivity decrease (Manoj, 2012). The decrease in resistivity is due to good crystalline growth which increases the carrier concentration of the thin films at the same time reduce the grain boundary scattering. However, as the oxygen pressure is over or reaches 0.005 mbar the resistivity increase. In addition to resistivity, the transmission of the films is also dependent on the background pressure. The bandgap is highest at 0.005 mbar and then decrease.

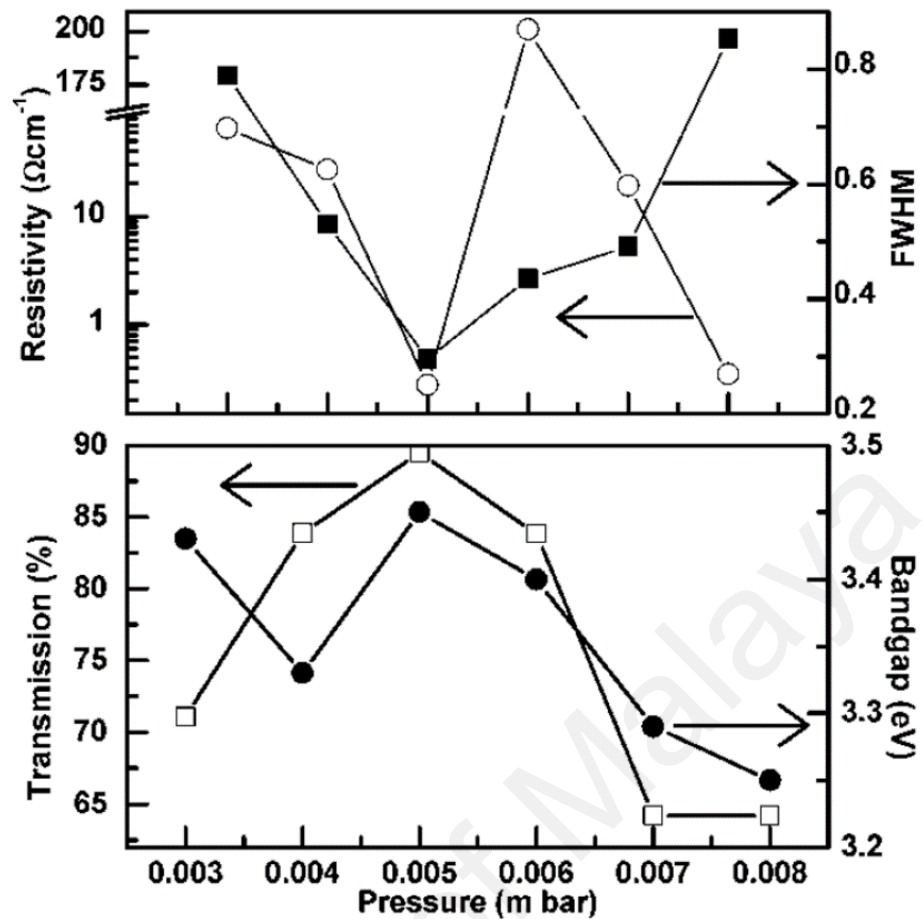


**Figure 2.5:** The electrical properties of AZO deposition at room temperature on the top and the transparency properties of AZO deposition at room temperature on the below (Manoj, 2012).

#### 2.2.4 The effects of substrate temperature in the growth of AZO

Higher substrate temperature up to 400 °C is found to increase the bandgap of AZO films when a 248 nm laser ( $2 \text{ J/cm}^2$ ) was used (Kang & Joung, 2013). As shown in Figure 2.6, the optical transmittance of AZO film with different substrate temperatures are over 80 % that the substrate temperatures did not affect the transparency of AZO films. Lower resistivity films of  $6.7 \times 10^{-4} \Omega\text{cm}$  were also obtained at 400 °C (Figure 2.7). Both the carrier concentration and mobility were higher when deposited at 400 °C. However, as the temperature reached 400 °C, the resistivity increase due to the large grain size of the films. Large grain size causes more scattering such as ionized impurity and grain boundary scattering, which results in low carrier mobility.

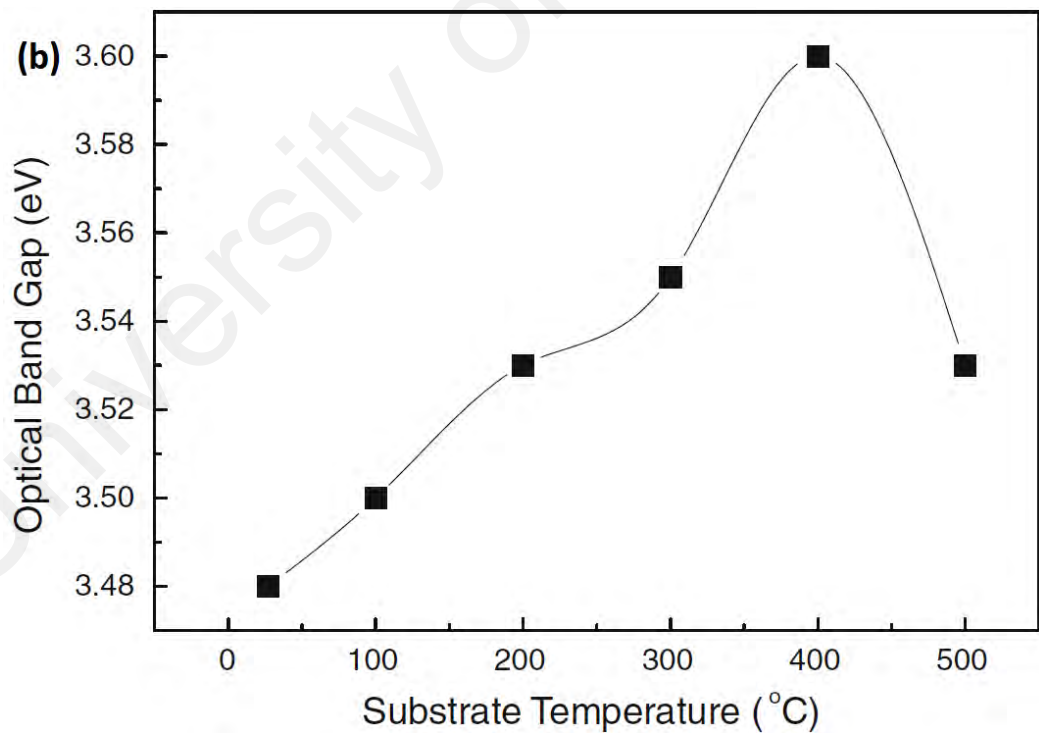
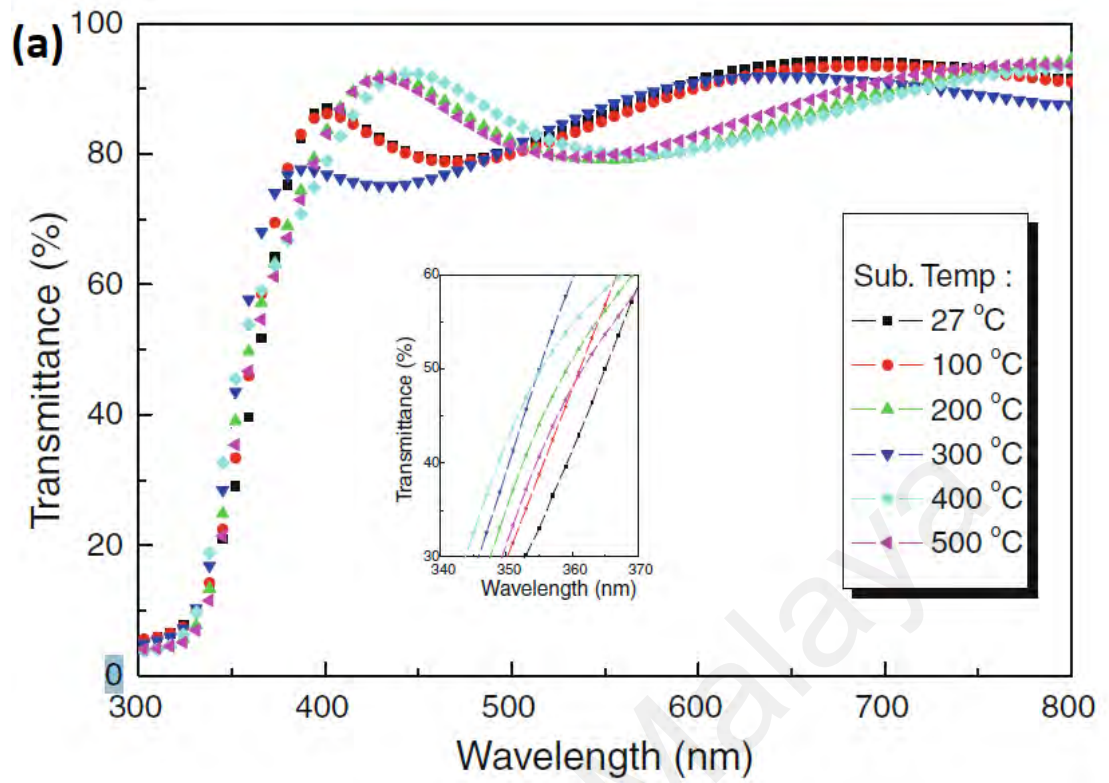


**Figure 2.6:** (a) The transmittance spectra of AZO with various substrate temperatures and (b) the Optical Bandgap with various substrate temperatures on the right (Kang & Joung, 2013).

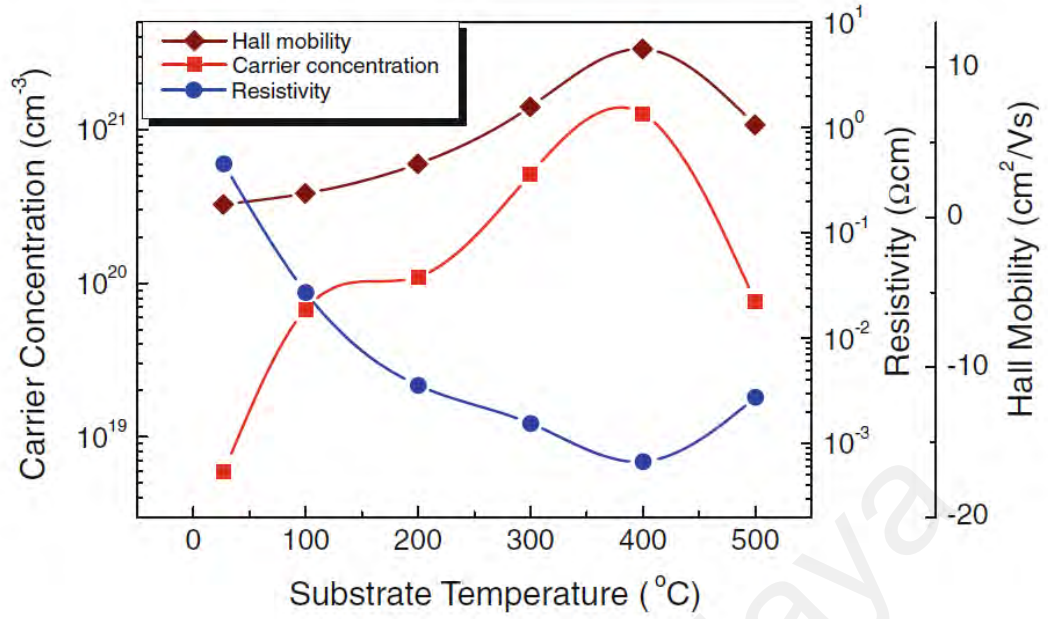


**Figure 2.7:** The electrical properties in different substrate temperature (Kang & Joung, 2013).

### 2.3 ZnO/Si heterojunction

According to Tuomisto et al., 2003; Liu et al., 2010; Look et al., 2005 and Fallert et al., 2007 unintentionally doped ZnO is n-type semiconductor due to its intrinsic defect. Thus, in order to fabricate ZnO based heterojunction, p-type substrate such as NiO (Hasan et al., 2015), GaN (Zhu et al., 2008) and Si (Jeong et al., 2003) were used. Among all of these p-type substrates, p-Si is widely used.

The band structure of an ideal case of n-ZnO/p-Si heterojunction based on the Anderson model in non-illuminated condition is shown in Figure 2.8. In this model, all the lattice mismatch and interface traps effect are neglected. The model has been used by Jeong and Alivov to explain their results (Alivov et al., 2005; Jeong et al., 2003), of ZnO/p-Si heterojunction and they used the Equation 2.1 to find out the value of  $\Delta E_c$  as shown in Figure 2.8.

$$\chi_1 - \Delta E_c - \chi_2 = 0 \quad (2.1)$$

where  $\chi_1$  represents the vacuum level of material “1”,  $\chi_2$  represents the vacuum level of material “2” and  $\Delta E_c$  is the different value between the conduction band of material “1” and conduction band of material “2”.

In the model, the total energy of an electron from the vacuum level to conduction bandgap of semiconductor material 1 to the conduction band of semiconductor material “2” and back to vacuum level must be zero. Therefore, based on the Equation 2.1, the conduction band discontinuity,  $\Delta E_c$  is the different between two electron affinities,  $\Delta E_c = \chi_{ZnO} - \chi_{Si}$ . The valence band discontinuity,  $\Delta E_v = \Delta E_c + \Delta E_g$ , where  $\Delta E_g$  is the different energy bandgap of the ZnO and Si. Other parameter value (room temperature) of the band structure which appeared at Figure 2.8 has shown in Table 2.1.

**Table 2.1:** Parameter value of the ZnO/Si heterojunction Bandgap of the Figure 2.8.

Symbol	Energy Value (eV)	References
$\chi_{Si}$	4.05	Ghosh et al., 1987; Majumdar & Banerji, 2009; Sundaran & Khan, 1997.
$\chi_{ZnO}$	4.45 ~ 4.5	Jeong et al., 2003; Alivov et al., 2005; Majumdar & Banerji, 2009.
Energy bandgap of silicon, $E_g$	1.12	Low et al., 2008.
Energy bandgap of ZnO, $E_g$	3.27~3.3	Morkoc & Ozgur, 2009.

**Table 2.1**, continued.

$\Delta E_v$	$\approx 2.55$ (n-ZnO/p-Si) $\approx 1.97$ (p-ZnO/n-si)	Bedia et al., 2013; Kabra et al., 2014.
$\Delta E_c$	$\approx 0.4$	Bedia et al., 2013

The value of  $\Delta E_c \approx 0.4$  eV and the  $\Delta E_v$  may be larger than 2.55 eV, the majority of the carriers (electrons) of the n-ZnO will diffuse across the junction from n-ZnO to p-Si in non-illuminated condition. Similarly, the majority carries of the p-Si (holes), holes will diffuse easily from p-Si into junction followed by into ZnO in non-illuminated condition. As a result, the equilibrium is reached when the depletion region is formed. However, the depletion region will be extremely narrow for the ZnO region if the ZnO is highly doped with donor element such as Aluminium. The carriers' diffusion will stop when the equilibrium is reached at zero bias condition. Under non-illumination and forward biasing, the current density is dominated by the majority carriers of the n-ZnO. Similarly, when the junction is reverse biased in non-illumination, the current density will be dominated by minority of the p-Si. The energy-band structure of p-ZnO/n-Si heterojunction is shown in Figure 2.9. The basic principle of p-ZnO/n-Si is similar to the n-ZnO/p-Si However, the majority carriers of ZnO is hole in p-ZnO, and electrons in n-Si.

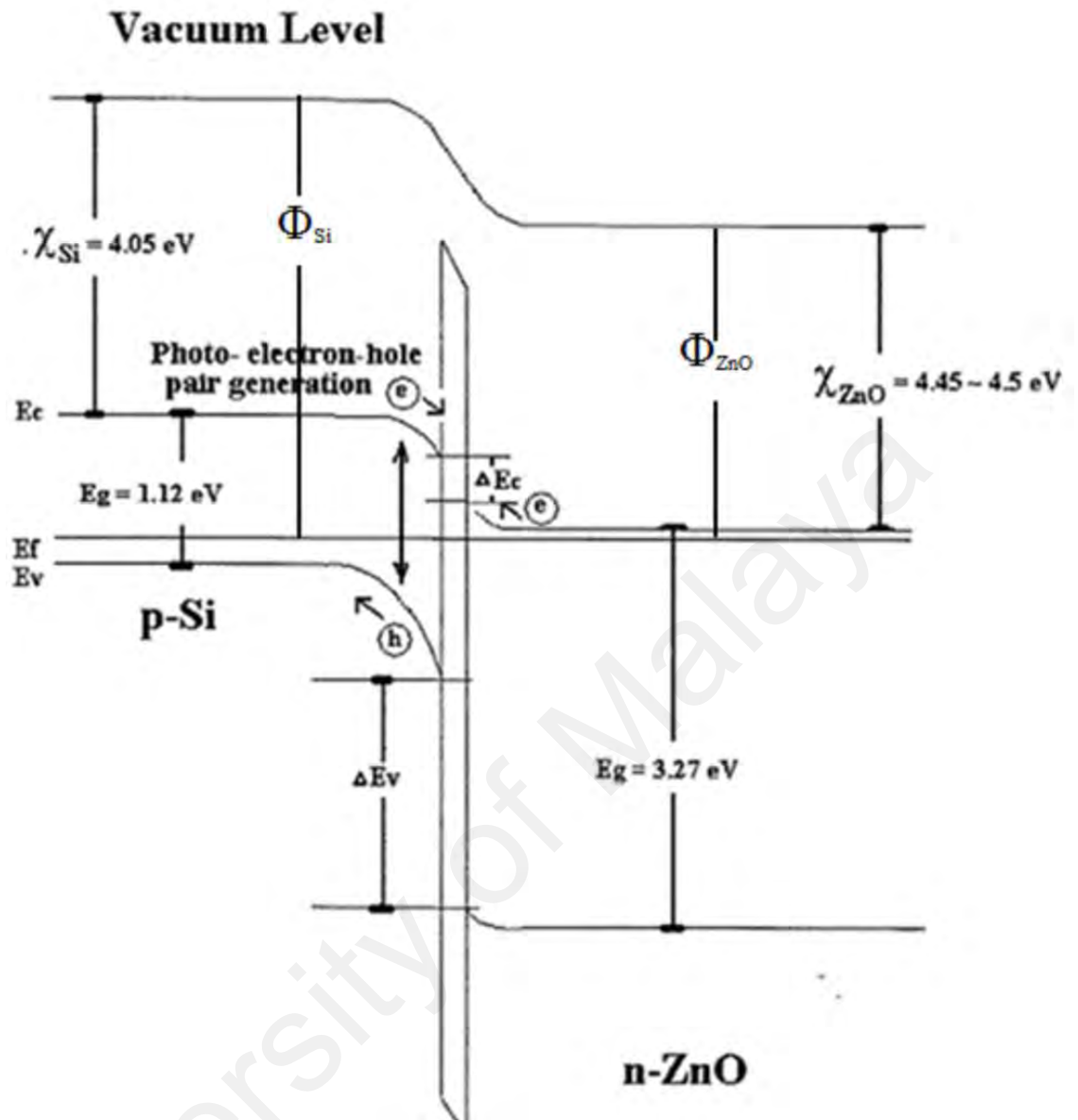


**Figure 2.8:** n-ZnO/p-Si heterojunction energy diagram in zero bias and non-illuminated (Jeong et al., 2003).

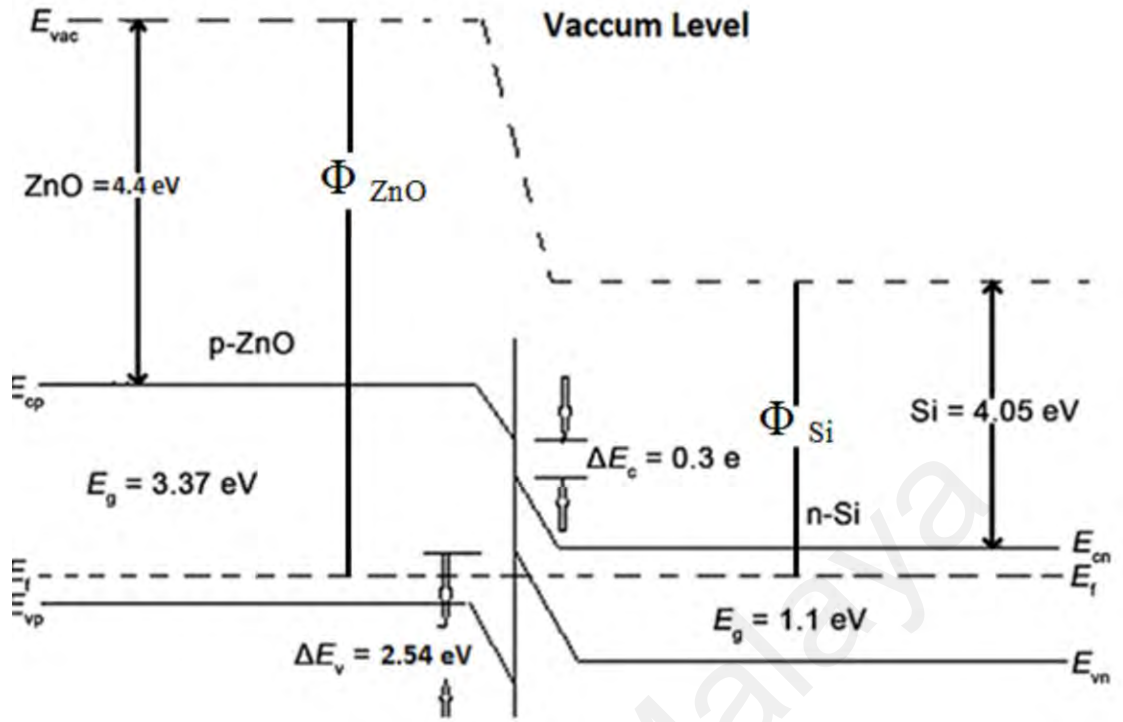


**Figure 2.9:** p-ZnO/n-Si heterojunction energy diagram in zero bias and un-illumination (Dutta & Basak, 2008; Kabra et al., 2014; Majumdar & Banerji, 2009).

The discontinuity in the conduction band edges  $\Delta E_c$  shown in Figure 2.8 and 2.9 are equal to the different between the electron affinities of ZnO and electron affinities of Si. The total built in voltage  $V_d$  on the both side of semiconductor is equal to the different between the work function of ZnO ( $\Phi_{ZnO}$ ) and work function of Si ( $\Phi_{Si}$ ).

Based on the work of Kumar et al., 2006, the relationship between the Current-Voltage and the heterojunction is given by:

$$I = A \exp \left[ \frac{-q(\Delta E_c + V_d)}{kT} \right] \times \left[ \exp \left[ \frac{qV}{kT} \right] - 1 \right], \quad A = aqXN_d (D_n/\tau_n)^{1/2}. \quad (2.2)$$

where  $q$  is the electron charge,  $K$  is the Boltzman constant,  $T$  is the temperature,  $a$  is the area,  $X$  is the transmission of electron across the interface  $D_n$ ,  $V_d$  is the total built in voltage and  $\tau_n$  is the lifetime of electron in p-type material.

The charge transport mechanism for n-ZnO/p-Si heterojunction under UV illumination in forward and reverse bias are shown in Figure 2.10. Based on the reports by Mridha & Basak, 2007; Baydogan et al., 2012a and Bai et al., 2013, UV photons are mainly absorbed in ZnO under illumination, due to the large bandgap of ZnO. The photogenerated electrons drift toward the positive electrode through the depleted ZnO region. Therefore, under UV illumination, the current linearly increases under reverse-bias condition. The energy bandgap of the ZnO is larger than the visible photons energy; therefore, under the visible illumination (400 nm to 700 nm, wavelength) the n-ZnO film acts as an antireflection layer or transmittance window. All of the visible photons energy passes through the ZnO film and absorbed primarily in the underlying p-Si layer. Consequently, under visible illumination, electron-hole pairs are generated and they are responsible for the observed photocurrent under reverse bias condition. However, due to the penetrated of the visible light, the photocurrent will become saturated when the depletion layer width of p-Si increases.

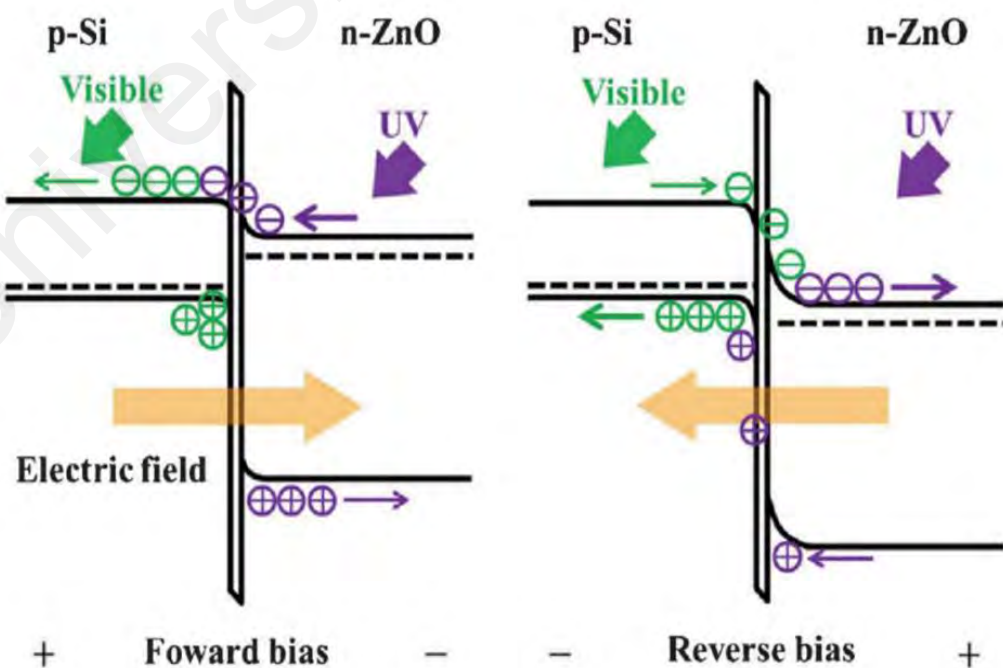


**Figure 2.10:** Energy band diagram and charge transport mechanism of n-ZnO/p-Si heterojunction under reverse and forward bias (Bai et al., 2013; Baydogan et al., 2012a).

Al-doped Zinc oxide (AZO) thin films have been deposited on the p-Si to form AZO/p-Si heterojunction (references). Because of the optical transparency and conductivity, AZO acts as a photo-window while causing a depletion region in the pn heterojunction. Furthermore, Yang et al., 2009 reported that low resistivity AZO contact layer can efficiently improve the photo-response of the pn heterojunction due to its metal-like properties.

### **2.3.1 Effect of different percentage of Al-dopant AZO/Si heterojunction**

The current-voltage (I-V) characteristics of the AZO/p-Si heterojunction with different percentage of Al dopant as shown in Figure 2.11. Figure 2.11(a) shows the I-V characteristics of the AZO/p-Si heterojunction measured in dark and Figure 2.11(b) shows the AZO/p-Si heterojunction under illumination (340 nm). As the forward voltage increased, the forward current increase because of the decrease in the width of depletion region. In addition, the forward current increase with the increase of doping concentration (1 % to 5 %) as compared to undoped ZnO. The increase of forward current with the doping is due to the increase in the carrier concentration.

In the same Figure 2.11, when illuminated with 340 nm light, higher forward and reverse current are obtained for all the samples. More carriers are generated in the AZO samples and forward current increase under illumination. The reverse current increase is due to the electron-hole pair generation in the depletion region when the incident photon energy is greater than the smallest direct-bandgap of the heterojunction.

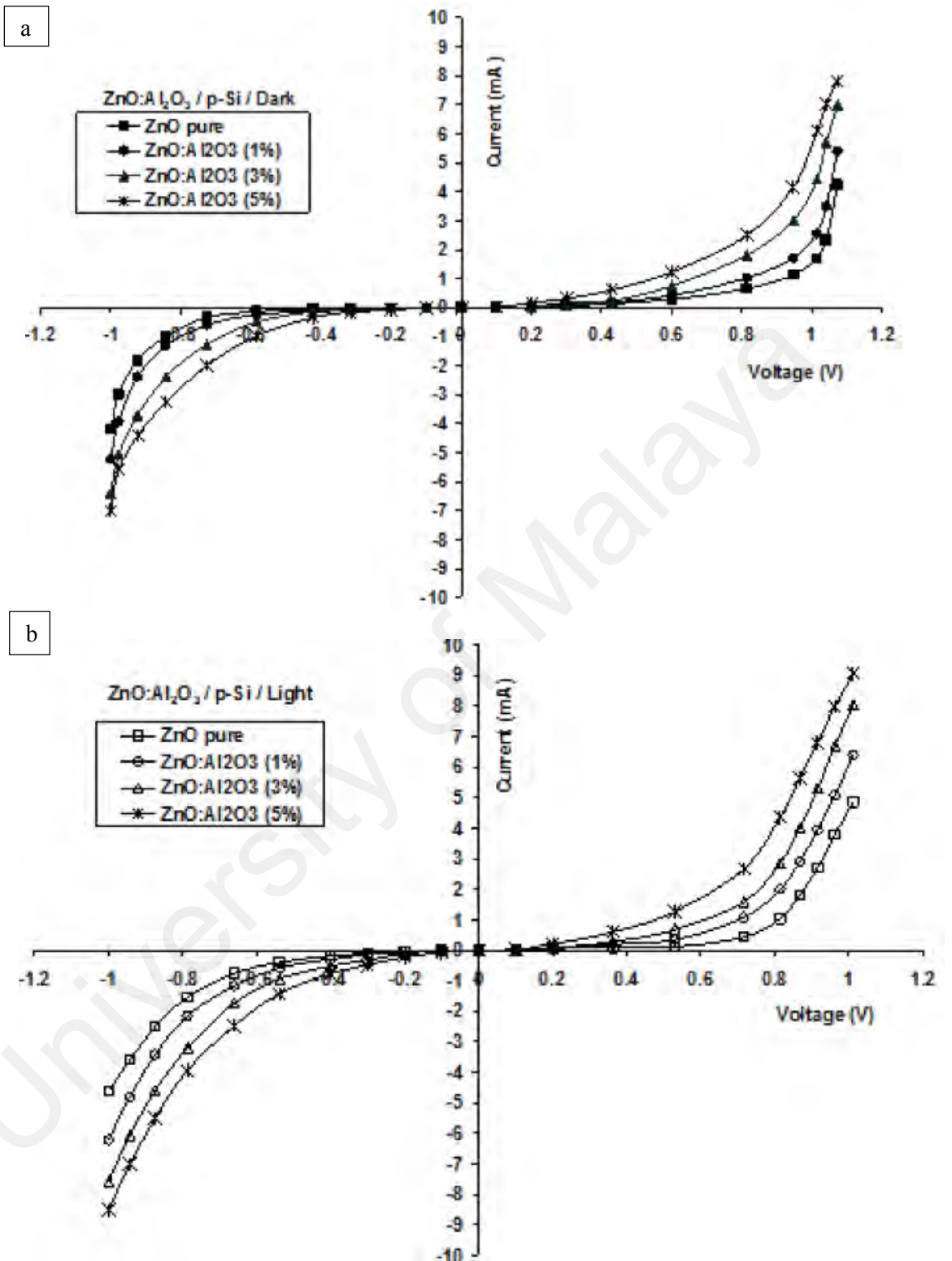


**Figure 2.11:** I-V characteristics of the undoped and Al-doped ZnO/p-Si heterojunction at different Al concentration: (a) dark and (b) under illumination (340 nm light wavelength, 2mW), (Yousif, 2014).

Figure 2.12 shown the current density-voltage (J-V) characteristic of AZO/p-Si with different doping percentage, measured at room temperature and illuminated by UV light (Baydogan et al., 2012b). As shown in Figure 2.12, under UV illumination, all of the sample show photoresponse to the UV and UV illumination improves the current in the AZO-p-Si junction especially in the forward bias. The photogenerated current is slightly larger than the dark current in the reverse bias. In reverse bias, the AZO/p-Si heterojunction with highest doping percentage (1.6 % Al-doped) shows the largest different between the dark current and photocurrent. The I-V characteristics in Figure 2.12 indicates that the increase of Al concentration (0.8 ~ 1.2 %) contributed to the slight increase on current density.

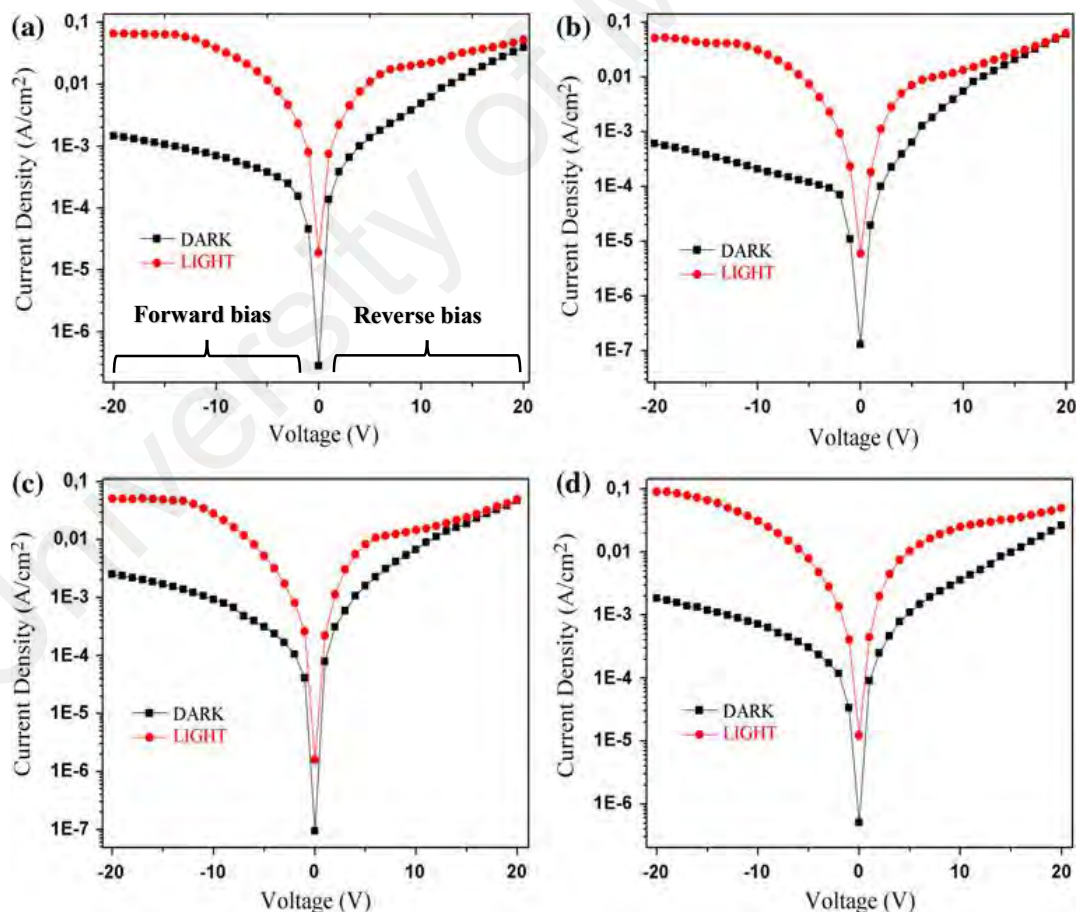
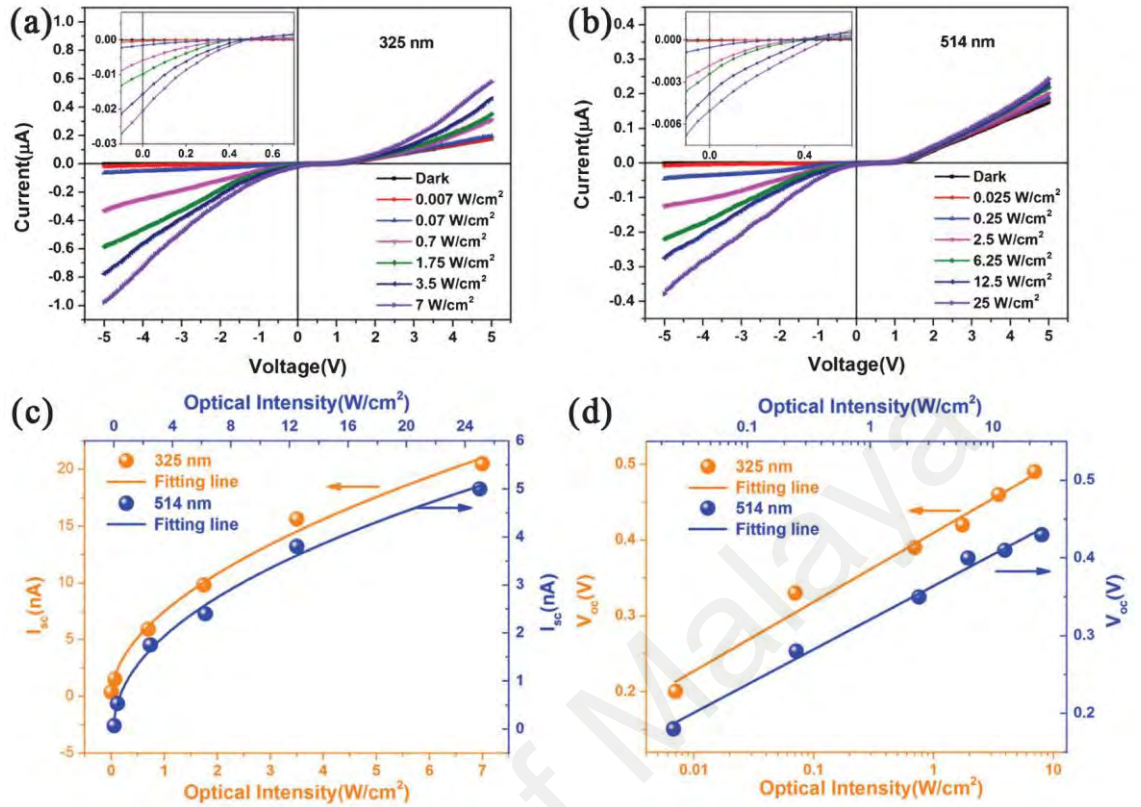


**Figure 2.12:** Current density-voltage (J-V) characteristics of Al-doped ZnO/p-Si heterojunctions at different Al-doping percentage: (a) 0.8 %, (b) 1.0 %, (c) 1.2% and (d) 1.6 % (Baydogan et al., 2012b).

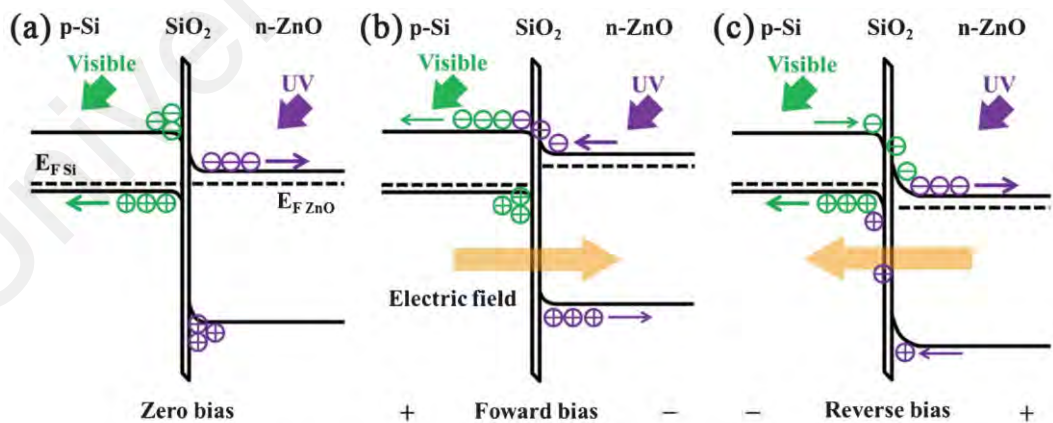
### 2.3.2 Effect of UV and visible light in AZO/p-Si heterojunction

Figure 2.13(a) and (b) show the I-V characteristics of the ZnO/p-Si heterojunction illuminated by UV (325 nm He-Cd laser) and visible light (514 nm Ar-ion laser) at different power density (Bai et al., 2013). As shown in Figure 2.13, the heterojunction responded to the UV and visible light in reverse bias. As the incident power density increased, the photocurrent increases in both visible and UV, and the increase was higher for UV illumination. In forward bias, the heterojunction responded to the UV light, but only showed a slight response to the visible light. Under the illumination of visible light in forward bias, the photo-generated carriers are confined in depletion region at p-Si by the large valence bandgap offset as shown in Figure 2.14(a). Therefore, under visible illumination in forward bias, the photocurrent is dominated by the flow of the minority carries (photo-generated electron), resulting in the small response in forward bias under visible illumination. However, under UV illumination in forward bias, the photogenerated electrons in n-ZnO side are able to tunnel through the barrier due to the small conduction band barrier as shown in Figure 2.14(b). In addition, the photo-generated hole in the depletion region drift to the n-ZnO and resulting in high photo-response to UV illumination.

Under reverse bias, the heterojunction responses to UV and visible light. The photogenerated minority carriers in both side (n-ZnO and p-Si) are able to pass through the depletion region, swept by the strong electric field and combine with the majority carrier as shown in Figure 2.14(c). As a result, the photocurrent generated is higher than the photocurrent generated in forward bias. Another mechanism that can lead to high photoreponse to the visible light in reverse bias has been explained in the report by Jeong et al., 2003. According to the report, the low energy photons passed through the AZO layer due to the wide bandgap of AZO, and absorbed in the depletion region of p-Si.



**Figure 2.13:** I-V characteristics of the n-ZnO/p-Si heterojunction in the dark and illumination with (a) UV light (325 nm) and visible light (514 nm). The effect of the light intensity in (c)  $I_{sc}$  and (d)  $V_{oc}$  (Bai et al., 2013).



**Figure 2.14:** Energy band diagram and carriers transport mechanism of n-ZnO/p-Si heterojunction under (a) zero bias (b) forwards bias and (c) reverse bias (Bai et al., 2013).

### 2.3.3 Effect of different pressure in growth heterojunction

The morphology and the structure of the thin films are highly dependence on the background gasses and pressure. Figure 2.16 shown the morphology and the I-V curve of the n-ZnO thin films deposited on the p-Si to form heterojunction by PLD (Qi et al., 2007). In Figures 2.16(a) and 2.16(b), ZnO films are deposited at low pressure ((a)  $10^{-5}$  Torr, (b)  $10^{-4}$  Torr ) and in Figure 2.16(c) and 2.16(d) they are deposited at high pressure ((c)  $10^{-3}$ Torr and (d)  $10^{-2}$  Torr). When deposited at low pressure, the reverse current was smaller and when deposited at high pressure the IV results were inverted. In the study, the oxygen pressure affects the structure and morphology of the thin films which subsequently affect the fermi level of ZnO. The ZnO films deposited at low pressure (Figure 2.16(a) and 2.16(b)) have more oxygen vacancies ( $V_o$ ) and zinc interstitials ( $Z_{ni}$ ) defect so the Fermi level approaches the bottom of the conduction band of ZnO which is similar to a common pn junction band diagram as shown in Figure 2.15(a). However, the ZnO films deposited in high pressure (Figure 2.16(c) and 2.16(d)) have more zinc vacancies ( $V_{zn}$ ) and oxide antisite ( $O_{zn}$ ) defect.  $V_{zn}$  and  $O_{zn}$  which spike the energy at the interface between ZnO and Si as shown in Figure 2.15(b). Therefore, under the forward bias in Figure 2.16(c) and 2.16(d), the spiked-bottom conduction band of p-Si approaches the fermi level of ZnO to cause electrons easily from ZnO side to p-Si side, resulting the forward current increase rapidly. However, under reverse bias in Figure 2.16(c) and 2.16(d), the electrons are difficult from ZnO side to p-Si due to the spiked-bottom conduction band of ZnO is away from the conduction of p-Si.

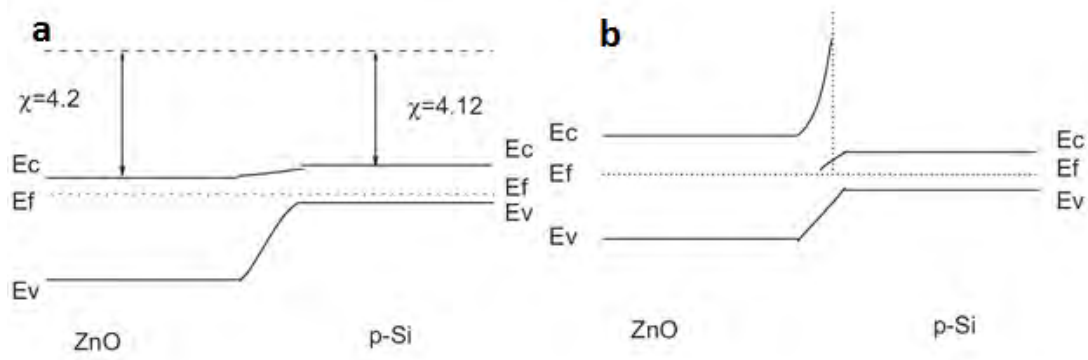


**Figure 2.15 :** The energy band diagram of the n-ZnO/p-Si heterojunction deposited with oxygen pressure of (a)  $10^{-5}$  Torr and  $10^{-4}$  Torr, (b)  $10^{-3}$  Torr and  $10^{-2}$  Torr (Qi et al., 2007).

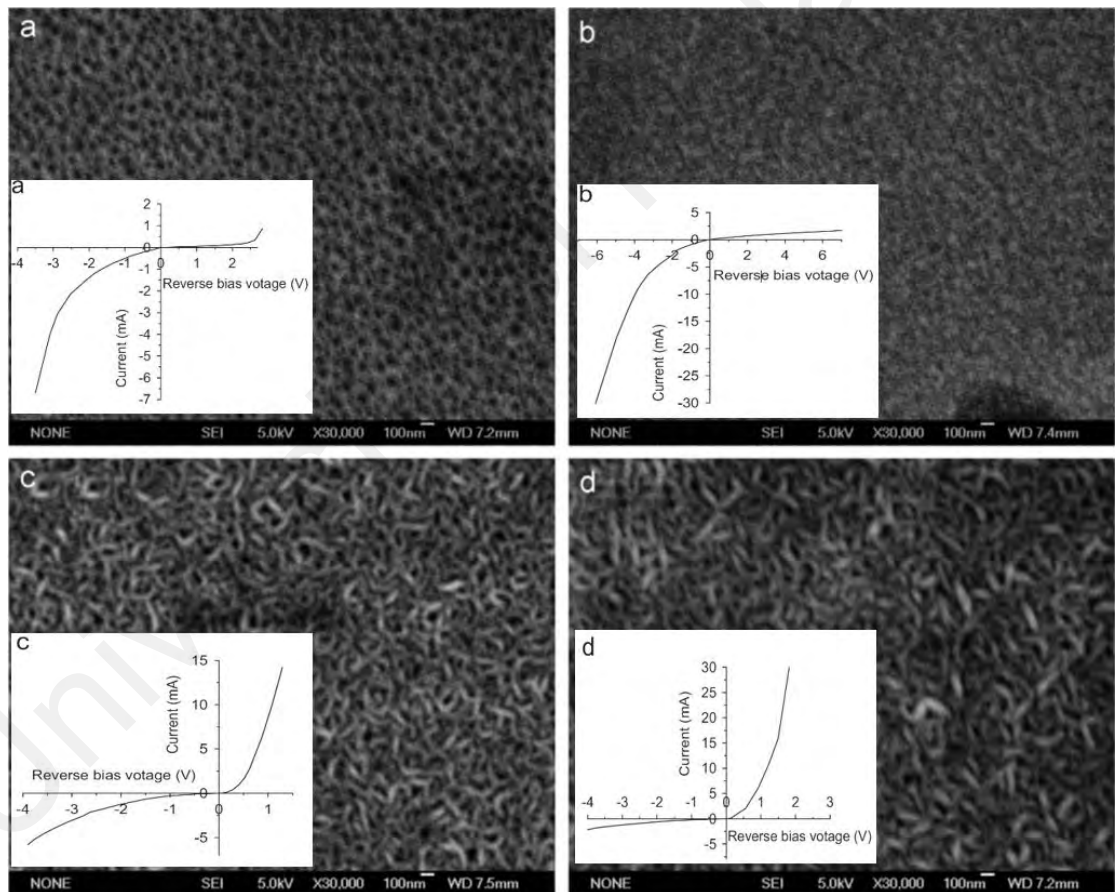


**Figure 2.16:** SEM image of ZnO and the I-V characteristics of the n-ZnO/p-Si heterojunction deposited by PLD with different oxygen pressure (a)  $10^{-5}$  Torr, (b)  $10^{-4}$  Torr (c)  $10^{-3}$  Torr and (d)  $10^{-2}$  Torr (Qi et al., 2007).

## CHAPTER 3: METHODOLOGY

### 3.1 Introduction

In this Chapter 3, the experimental set-up, deposition parameters of AZO films, plasma diagnostic techniques and the characterization techniques are presented. This is followed by the fabrication process and measurement of AZO/p-Si heterojunction.

### 3.2 PLD System

The PLD system consist of 3 most important parts; Nd-YAG laser, laser beam delivery and deposition chamber as shown in Figure 3.1.

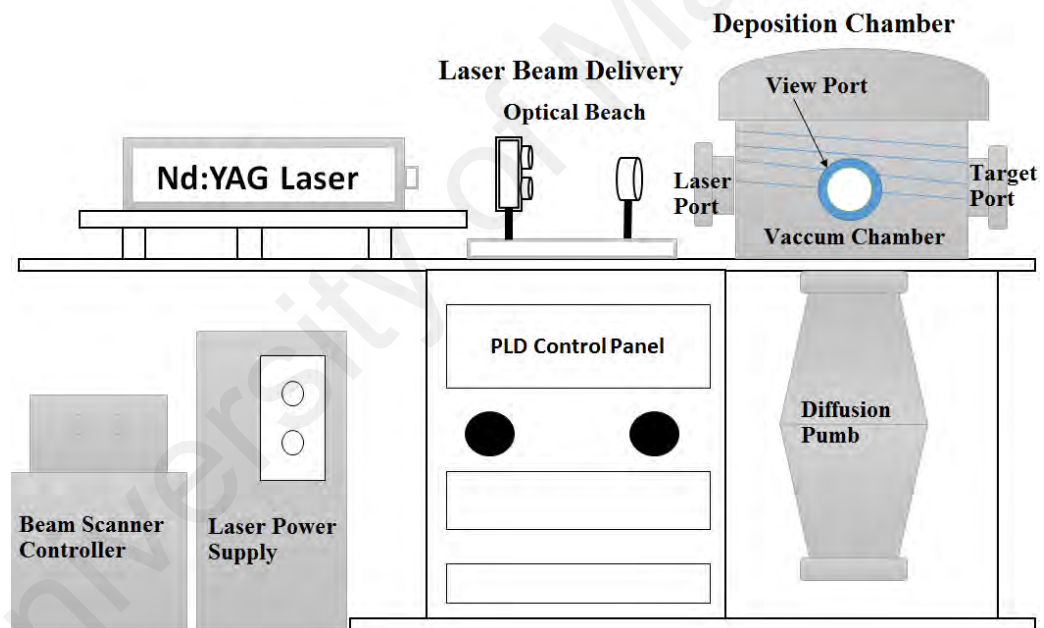


**Figure 3.1:** Schematic diagram of Pulsed Laser Deposition System.

#### (A) Nd-YAG Laser

Nd-YAG laser (EKSPLA-NL301) with a fundamental wavelength of 1064 nm, frequency doubled to 532 nm and frequency tripled to 355 nm is used for the deposition of AZO thin film. In the current work, laser wavelengths of 355 nm and 532 nm are used. The pulse duration of the laser is 4.7 ns and the repetition rate is fixed at 10 Hz. The laser

beam has a ‘top-hat’ profile and the diameter of the laser beam is 6 mm. The maximum laser energy is  $\sim 30$  mJ for both 532 nm and 355 nm and can be controlled by adjusting the voltage setting. The pulse energy is measured by using a photo-detector (Oriel 70721) which is connected with an energy meter (Oriel 70260).

### (B) Laser Beam Delivery Optics

The laser beam is guided onto the target placed in the deposition chamber by using a series of optics which include two mirrors, a focusing lens and an aperture. The second mirror is mounted onto a x-y motorize stage that scan the laser beam in x-y direction on the target. This results in a scanned area of  $6 \times 10$  mm on the target. The overall set-up is shown in Figure 3.2. Laser beam is focused using a focusing lens to produce a beam size of laser beam is focused using a focusing lens to produce a beam size of  $\approx 0.0005$  cm<sup>2</sup> on the target. The laser fluences were about 0.6 to 4.7 J/cm<sup>2</sup>.

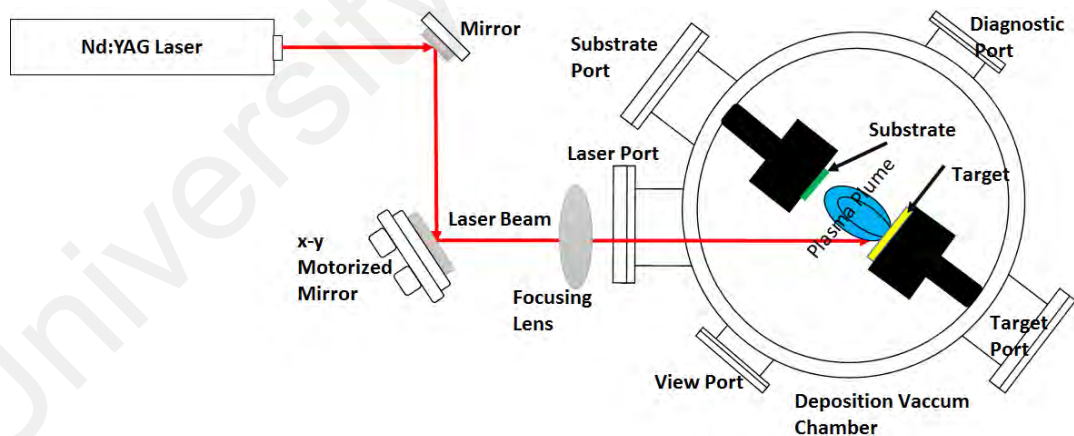


**Figure 3.2:** Schematics diagram of laser beam delivery optics system.

### (C) Deposition Chamber

A stainless steel deposition chamber is used and it is pumped by a rotary rouging pump and a diffusion pump as shown in Figure 3.2. This results in a base pressure of  $10^{-6}$  Torr. After achieving the base pressure, oxygen gas (99.99 %) purity is introduced to the

chamber with a flow rate of 0.4 ~ 1 sccm during deposition. Plasma diagnostics are performed by using the available viewports and vacuum feedthrough of the chamber.

### 3.3 Deposition parameters of AZO thin films

Laser alignment and energy measurement are performed prior to deposition. The substrates: p-type (100) silicon and corning glass (Corning #26003) were cleaned by acetone, IPA and DI water in ultrasonic bath (B1510E-DTH, 230V) for 10 min respectively. The cleaned substrates were blown dried by nitrogen gas. After the cleaning process, the substrates were placed in the deposition chamber. The distance between the AZO target to the substrate was fixed at 5 cm in all the experiments. The deposition chamber was then pumped down to a base pressure of  $10^{-6}$  Torr by using the diffusion pump. Subsequently, oxygen gas was pumped into the chamber until 16 mTorr. Deposition was carried when the oxygen pressure was stable, and deposition was performed for a duration of 90 min. The deposition parameters are summarized in Table 3.1

**Table 3.1:** AZO thin film deposition parameter.

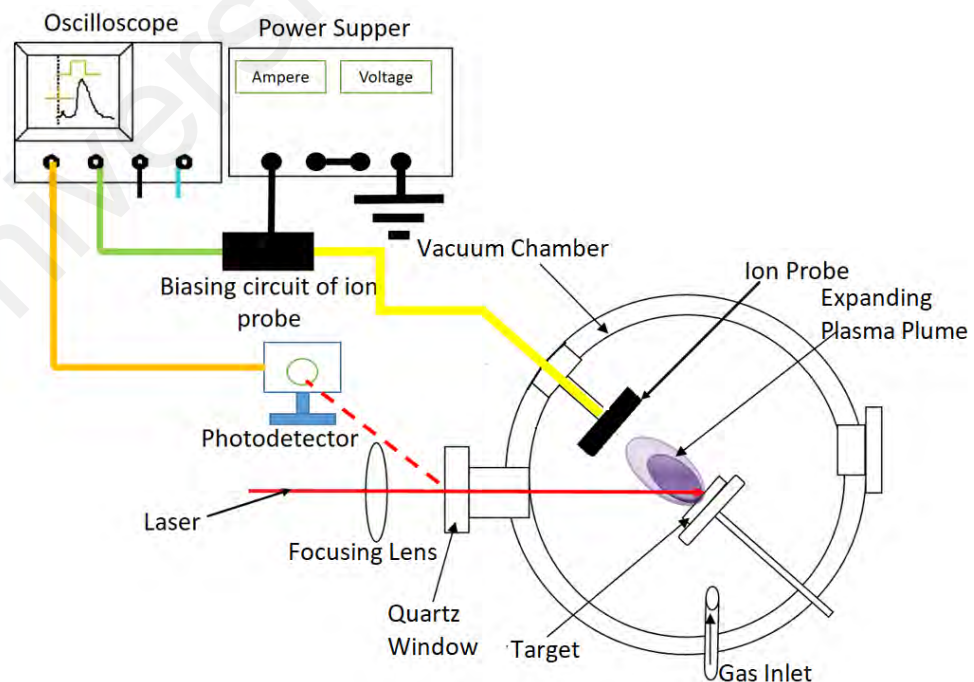
Parameter	Type, value or size	
Laser	Type	Q-switched Nd:YAG pulsed laser
	Wavelength	532 nm (2 <sup>nd</sup> harmonic) 355 nm (3 <sup>rd</sup> harmonic)
	Laser pulse duration	4.7 ns
	Repetition rate	10 Hz
	Laser Fluence	2 J/cm <sup>2</sup> . 4 J/cm <sup>2</sup>
Target	AZO	98 wt % ZnO and 2 wt % Al <sub>2</sub> O <sub>3</sub>
	Purity	99.99 %
Substrate	Materials	# 26003 corning glass p-type silicon (100)
	Substrate-target distance	5 cm
	Temperature	Room temperature
	Deposition duration	90 min
Gas	Type	Oxygen gas
	Gas pressure	16 mTorr
	Flow rate	0.4 to 1 sccm

### 3.4 Plasma diagnostics

Techniques such as optical emission spectroscopy, spectroscopy of X-rays, charge collectors and ion probe measurement are used to characterise plasma. Ion probes measurement and optical emission spectroscopy are used in this experiment to analyse plasma constituents while ion probes measurement is used to obtain the time-of-flight information.

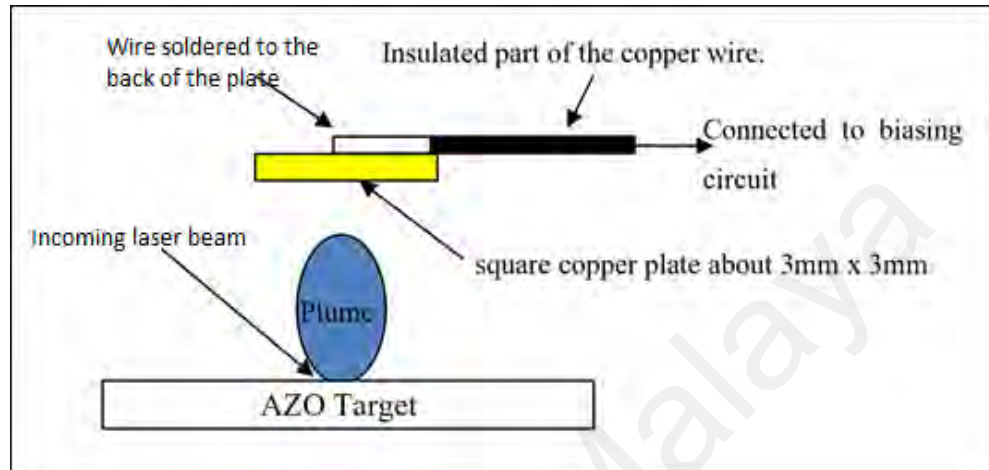
#### 3.4.1 Ion probe measurement

Figure 3.3 shows the set-up of the ion probe measurement where the ion probe is triggered by the reflected laser beam onto the photodiode and the signal is captured by an oscilloscope. The laser is incident at an angle of  $45^\circ$  to the AZO target and the ion probe is perpendicular to the AZO target, at the position of the substrate. With the setup, time-of-flight signal is captured at fixed distance given by the distance between the ion probe and the target (5 cm).



**Figure 3.3:** Experiment set up for ions probe measurement.

An ion probe (Langmuir probe) is made with copper plate with a dimension of 3 mm × 3 mm. It is connected to the biasing circuit. An ion probe (Langmuir probe) is positioned perpendicular to the AZO target as shown in Figure 3.4.



**Figure 3.4:** Schematics diagram of the ion probe set-up (Top View).

### 3.4.2 Optical Emission Spectroscopy (OES)

Optical Emission Spectroscopy (OES) is used to analyse the AZO plasma plume. The species and their line intensities, as well as the presence of impurities in the AZO ablated plasma plume are determined. The optical emission spectra emitted by the AZO plasma plume are recorded with the fibre optic spectrometer (Avaspec-3648). The spectra response range are from 183 nm to 753 nm wavelength. The AZO plasma plume, focusing lens and the detector are arranged according to the Equation 3.0:

$$\frac{1}{f} = \frac{1}{u} + \frac{1}{v} \quad (3.0)$$

where the  $f$  is the focal length (focusing lens),  $u$  is the object distance (the distance between the focusing lens and the AZO laser-produced plume) and  $v$  is the image distance (the distance between the focusing lens and the detector). The measurement set-up is shown in Figure 3.5; the optical emission collects through the single-core quartz fibre recorded by spectrometer.

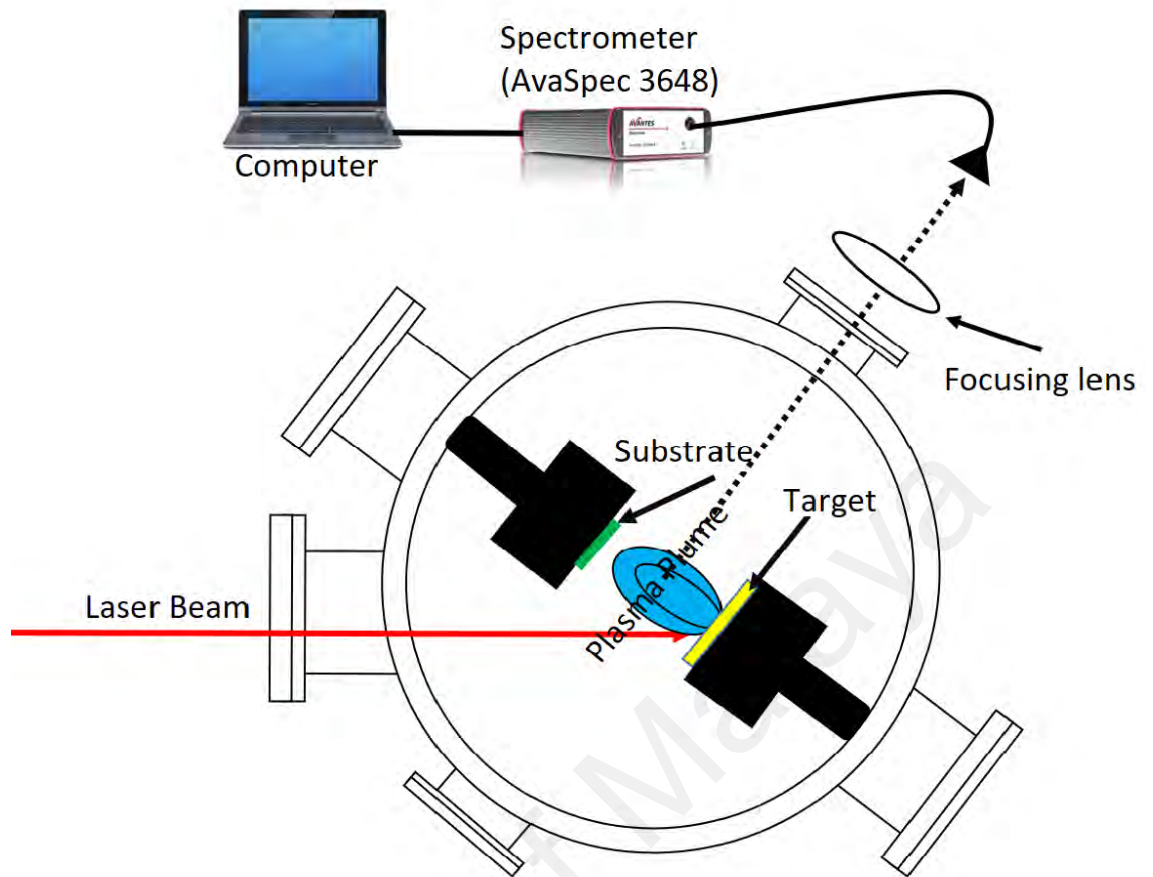


**Figure 3.5:** Schematics diagram of the optical emission spectroscopy set-up.

### 3.5 AZO Thin Film Characterisation Techniques

The AZO thin films are characterised by using Stylus Profilometer, Scanning Electron Microscope (SEM), Atomic Force Microscopy (AFM), UV-Vis Spectrometer and Four-point Probe for their morphology, structures, optical and electrical properties .

#### 3.5.1 Stylus Profilometer

A profilometer (Mahr Perthometer 32) is used to measure the thickness of the deposited thin films in this experiment. The stylus is aligned to travel across the edge of the step that is created by the mask on substrate. It measures the thickness of the thin films by variation of the vertical displacement across the edge which is between the surface of AZO thin films and the surface of the substrate.

### 3.5.2 Scanning Electron Microscope (SEM)

Scanning electron microscope scans the sample by electron beam instead of light, thus is able to provide high resolution images of the sample. The electron beam is produced by the electron gun at the top and emission vertically to the sample typically in vacuum environment. Amount of signal will be produced when the electrons incident across the sample as primary backscatter electrons, X-ray, Auger electron and the secondary electrons. Secondary electron is knocked out from the sample by the incident electrons while backscattered electrons scattered from the sample atom nucleus. They are commonly used in SEM for sample image. The secondary electrons are detected by the secondary electrons detector whereas the backscattered electrons are detected by the backscattered electrons detector as shown in Figure 3.6. Basically, secondary electrons are used for analysis of morphology of the sample. Backscattered electrons normally used in analysis of composition in multiphase of the sample.

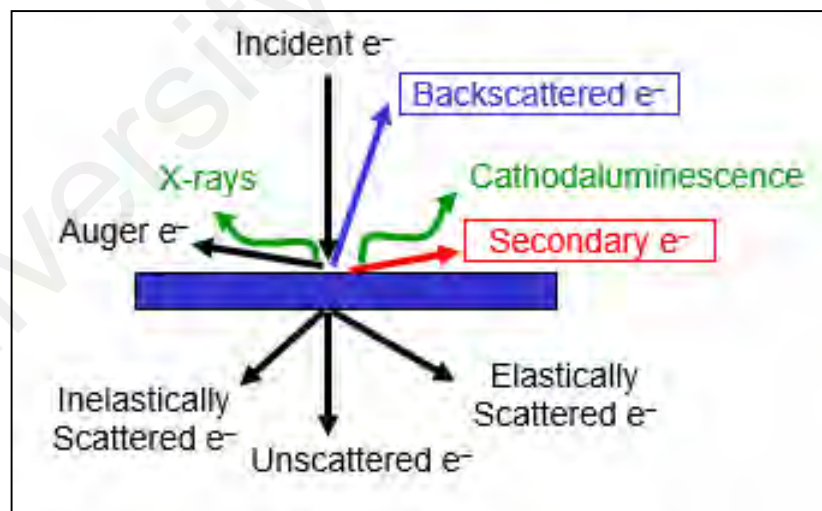


**Figure 3.6:** Electron-sample interaction mechanism.

Energy-dispersive X-ray Spectroscopy (EDS) is an addition part for SEM. When electron beam hits the sample, the electron in low level energy or inner shell (K-shell) will be knocked out. Energy will be released in the form of X-ray when the electron from

the outer shell (L-shell) moves to an inner shell (K-shell) to fill the hole. Therefore, the EDS measured the atomic structure and chemical composition of the sample through the X-rays emitted.

In this work, SEM (Hitachi Tabletop TM 3030) with EDX detector (Bruker Quantax 70) are used for sample analysis. The typical operating voltage is 15 KV.

### **3.5.3 Atomic Force Microscopy (AFM)**

AFM measures the morphology of the surface material and provides surface image in both three dimensions (3D) and two dimensions (2D). The height and width of the grain size of the surface film can be obtained from the 3D topology of the samples. Sharp ceramic or semiconductor tips of AFM scans over a surface of the thin films. The feedback system of the AFM consist of a laser and a photodetector, they work together to obtain the morphology of the thin films surface. During the scanning, the tip will be repelled or attracted by the AZO thin film. The laser beam point to the cantilever will be deflected and the deflected magnitude and the angle will be detected by the photodetector. In contact mode, the force of the probe is kept contact and directly follows the topography of the surface during scanning. Non-contact mode so-called vibrating mode which is used the concept of the attractive Van der Waals forces acting between the tip and the surface of film whereas the tapping mode is implemented by the concept of oscillating the cantilever at the cantilever's resonant frequency by piezoelectric crystal.

Atomic force microscope (Nanosurf, Liestal, Switzerland) which can work in static mode and dynamic mode is used to measure the surface morphology of the samples.

### 3.5.4 UV-VIS Spectrophotometry

The transmittance of AZO thin films is measured by using a deuterium-halogen light source (Avalight-DHc) and a spectrometer (Avaspec-3648) that response to the wavelength range of 180 nm to 750 nm. Figure 3.7 shows the general set-up of the UV-VIS spectrophotometer system. Transmittance is obtained based on:

$$\%T_{\lambda} = \frac{S_{\lambda}-D_{\lambda}}{R_{\lambda}-D_{\lambda}} \times 100 \quad (3.1)$$

where  $\%T_{\lambda}$  is percentage of transmittance,  $S_{\lambda}$  is intensity of the sample intensity,  $R_{\lambda}$  is intensity of the reference and the  $D_{\lambda}$  is background intensity as a function of wavelength ( $\lambda$ ). In absorbance mode:

$$\%A_{\lambda} = -\log \frac{S_{\lambda}-D_{\lambda}}{R_{\lambda}-D_{\lambda}} \quad (3.2)$$

From the optical properties of the thin film in transmittance and absorbance, the optical energy bandgap of thin film can be estimated by Tauc Plot. The equation of the Tauc Plot for optical direct bandgap can be written as:

$$(\alpha hv)^2 = A(hv - E_g) \quad (3.3)$$

where  $A$  is the constant magnitude for direct transition bandgap,  $hv$  is the photo energy and  $E_g$  is the optical bandgap.

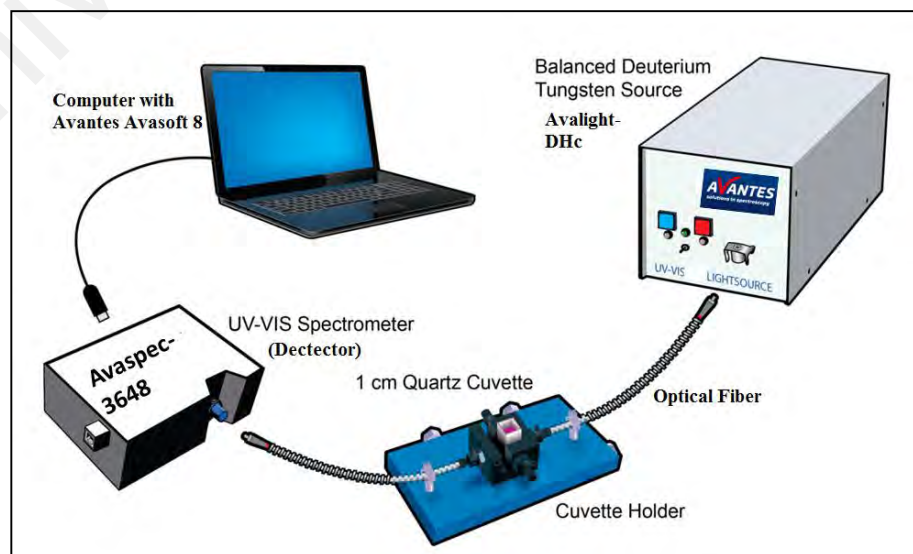


Figure 3.7: UV-VIS spectrophotometer set-up.

### 3.5.5 Four Point Probe

Four-point probe technique is used to measure the average resistance of a thin layer or sheet. Current is passed through the two outer probes while voltage drop across the two inner probes are measured (Figure 3.8). The sheet resistance of the thin layer,  $R_s$  is the unit of ohm/cm<sup>2</sup> is given by:

$$R_s = C.F \frac{V}{I} \quad (3.4)$$

where C.F is correction factor which is depends on the probe and sample geometry. In the condition of infinitely thin film with constant spacing (S), and the conducting film thickness is less than 40 % of the spacing; the value of C. F = 4.53. Hence,

$$R_s = 4.53 \times \frac{V}{I} \quad (3.5)$$

The resistivity  $\rho = R_s \times d$  where  $d$  is thickness.

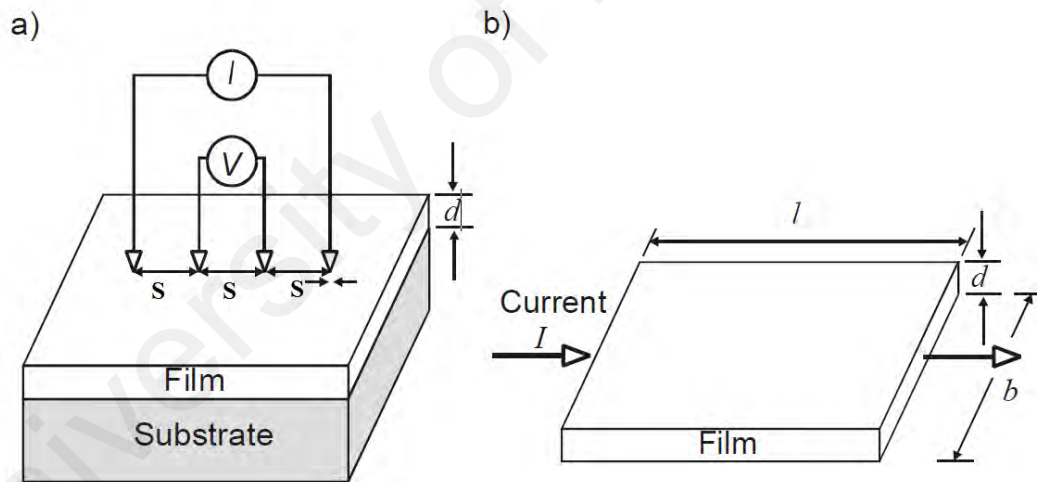


**Figure 3.8:** (a) Schematic diagram of 4 point probe and (b) Geometry of thin film which define the relationship between the sheet resistances.

In this work, the measurement is performed by using source measuring unit (Keithkey SMU236) connected to a probe station (Ohio). The sheet resistance is measured for thin films on corning glass.

### 3.5.6 X-Ray Diffraction (XRD)

X-ray diffraction (XRD) with CuK $\alpha$  line at 1.5418 Å (Bruker, Massachusetts, D5000) is used to measure the AZO thin films crystallinity in this work. XRD is an analytical method that used to identify the crystalline material and provided the detail of unit cell dimensions or atoms arrangement. The basic working principles of XRD is based on the constructive or destructive interference of monochromatic X-rays and a crystalline sample. During the measurement, X-ray beam being radiated by atom's electron when high energy beam bombard on the sample. According to Bragg's Law, the diffraction from the crystal of the sample could be obtained by the equation below:

$$n\lambda = 2 d \sin\theta \quad (3.6)$$

where  $\lambda$  is the X-ray wavelength,  $d$  is the atomic spacing,  $n$  is an integer for the order of scattering and  $\theta$  is the diffraction angle. Besides, the crystalline size of the sample can be determined by the full width half maximum (FWHM). According to the Debye-Scherrer's equation, the crystallite size of material along the c-axis can be calculated by using the Equation 3.7:

$$D = \frac{0.9\lambda}{\beta \cos\theta} \quad (3.7)$$

where  $\lambda$  is the wavelength of the incident X-ray,  $\beta$  is the half intensity width of the peak,  $D$  is the crystallite size and  $\theta$  is the diffraction angle.

### 3.5.7 Room Temperature Photoluminescence

Photoluminescence of AZO thin films are measured by using a pulsed laser source at 266 nm (Lotis) as an excitation source at room temperature. The laser beam is incident onto the sample at 45°, and photoluminescence is detected by using a spectrometer (Advantes, AvaSpec 3648) at 90° to the sample surface as shown in Figure 3.9.

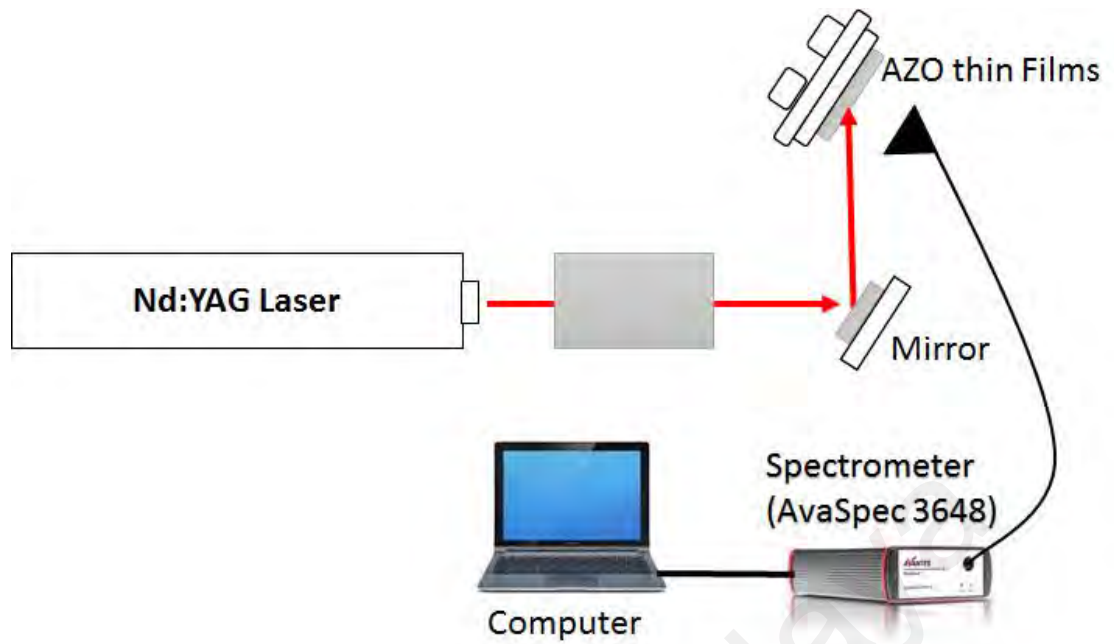


**Figure 3.9:** Experiment set up for PL measurement.

### 3.6 Fabrication and Characterization of AZO/p-Si Heterojunction

In this section, the fabrication characterization of AZO/p-Si heterojunction will be discussed. I-V measurement is used to measure the I-V characteristic of the AZO/p-Si heterojunction in dark and under illumination. UV and visible light source are used as the light source in all the illumination measurement respectively.

#### 3.6.1 Fabrication for AZO/p-Si Heterojunction

AZO thin films are deposited onto p-Si substrates (0.3 mm, 0.7  $\Omega$ cm, Boron-doped) in order to obtain the heterojunction structure as shown in Figure 3.10. Subsequently, gold layer is deposited onto AZO sample and aluminium contact is placed below p-Si. The top gold layer is coated from gold wire (99.99 %) by using a thermal evaporator (Edwards, Auto 360). The thickness of the gold layer is  $\approx$  30 nm, which gives transmittance of 75 % in the visible range.

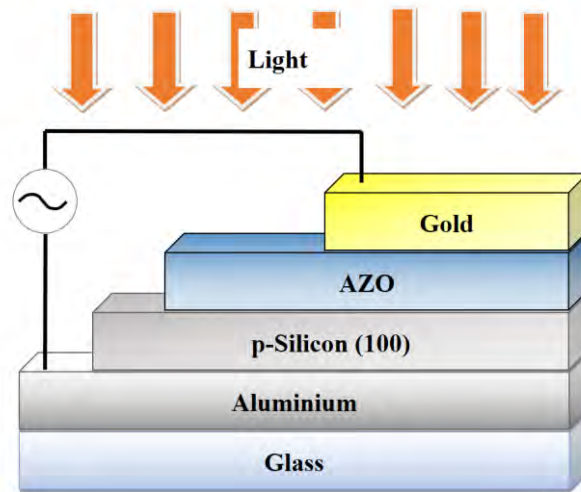


**Figure 3.10:** Schematics diagram of the Ag/AZO/p-Si/Al structure.

### 3.6.2 Characterization of AZO/p-Si heterojunction

I-V measurements are performed based on the schematic in Figure 3.11, by using I-V source measuring unit (Keithley 236) and 2 probes (tungsten tip). I-V characterization was measured in the dark and under illumination. Visible light source (24 V, 250 W, OSRAM) and UV light source (R838, VLARSUN) are used as the light source in all the illumination measurement respectively. The light source is perpendicular to the sample and the distance between the sample and the light source is 3 cm for visible light as shown in Figure 3.11(a) and 2.5 cm for UV light source. The spectrum of the visible light source and UV light source are measured by UV-Vis spectrometer (Avaspec-UL2048, 220-1100 nm), and their spectrum are shown in Figure 3.11(b) for visible and Figure 3.11(c) for UV illumination respectively.

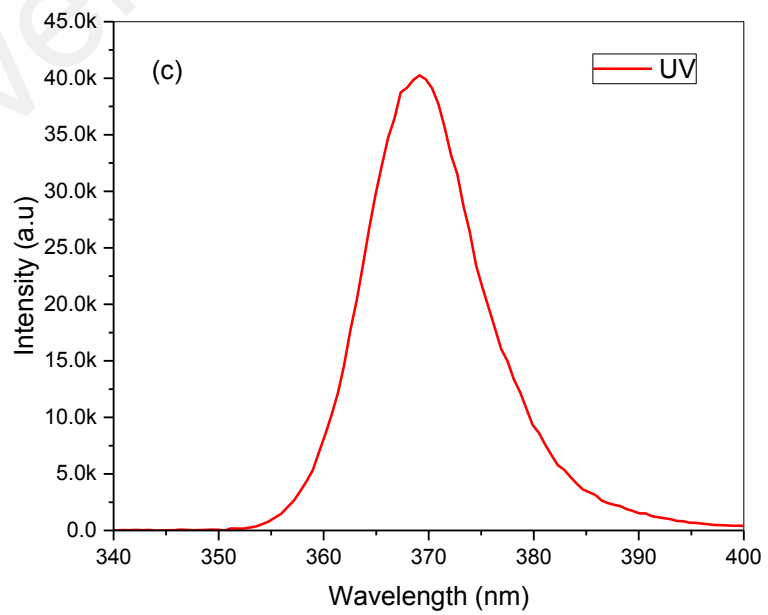
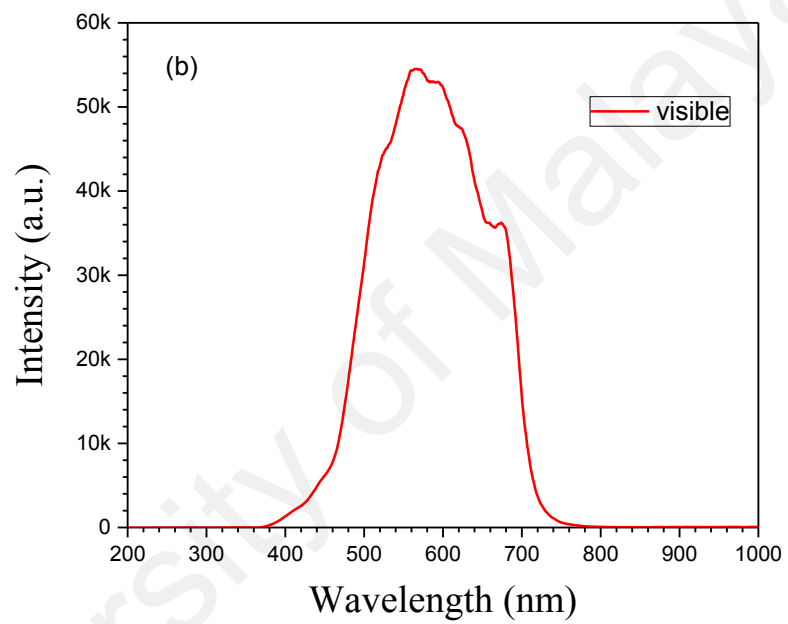
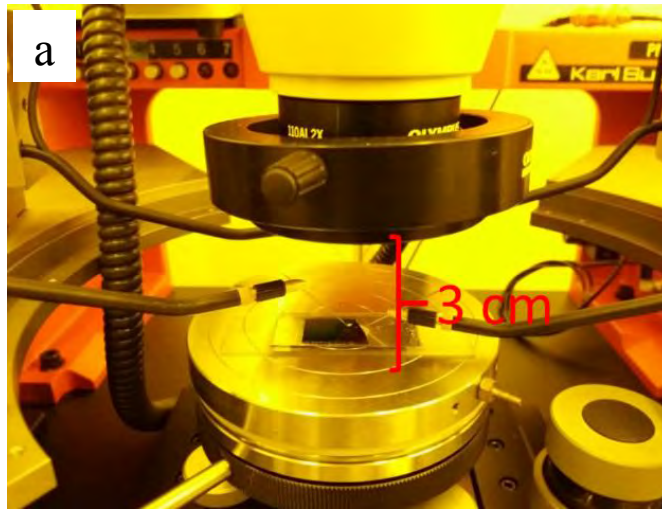


**Figure 3.11:** (a) Diagram of the illumination system, (b) Spectrum of the visible light and (c) Spectrum of the UV light.

## **CHAPTER 4: PLASMA CHARACTERISTICS AND THE PROPERTIES OF AZO FILMS BY PLD**

### **4.1 Introduction**

In PLD, the quality or the material growth is affected by the energetic plasma plume formed. In this section, the effect of the laser energy and the laser wavelength in the laser-produced plasma are discussed. PLD process started with laser ablation of the target, followed by plasma formation and expansion, and finally materials growth on the substrate. Therefore, the laser parameters are the factors that influence the species formed inside the plasma, which in turn influences the growth of thin films. In the current work, the beam size of the laser was kept to 6 mm<sup>2</sup> and the samples were positioned 5 cm from the target. The growth of AZO films was performed in O<sub>2</sub>. The effects of laser wavelengths and fluences are studied by using the laser at 355 nm and 532 nm and varying the laser fluences.

### **4.2 The effects of laser wavelength and fluence on the plasma characteristics**

The effects of the laser wavelength and laser fluence in the laser-produced plasma will be discussed in this section. Optical emission spectra (OES) and time of flight measurement are used to characterise the species of the laser-produced plasma.

#### **4.2.1 Optical emission spectra**

The optical emission spectra of 355 nm and 532 nm ablation of AZO are shown in Figure 4.1. The atomic lines of Zn, Al and O were identified based on the atomic spectra database (Kramida et al., 2015). Zn I (472 nm, 481 nm) was emitted at the threshold laser fluence of ~ 0.9 J/cm<sup>2</sup> for 355 nm laser; in agreement with those reported by the same laser (Joshy et al., 2008). When 248 nm laser was used (Claeyssens et al., 2002), Zn I at 637 nm were commonly observed. These lines remained as the brightest as laser fluence

increased. On the other hand, Zn I (637 nm) was the first species detected at  $\sim 0.6 \text{ J/cm}^2$  for 532 nm ablation while Zn I (472 nm, 481 nm) were detected above  $2 \text{ J/cm}^2$ . Emission from Al I was detected at 396 nm at laser fluence above  $\sim 2 \text{ J/cm}^2$  for both laser wavelengths.

355 nm laser produced higher ionized species such as Zn II (492 nm, 589 nm, 610 nm) at lower fluence as compared to 532 nm laser ascribed to the higher photon energy of 355 nm. It is noted that 532 nm laser ablation induced a broad emission band centred at  $\sim 700 \text{ nm}$  due to the presence of O. The presence of O is concluded to be originated from the AZO target than from the  $\text{O}_2$  in the background because the same emission band was also observed when ablation was performed in  $10^{-6}$  Torr. The normalized intensity of the characteristic lines is extracted and plotted against laser fluence in Figure 4.2. The emissions from the dominant Zn I lines were consistent and follow the same trend for 355 nm and 532 nm respectively.

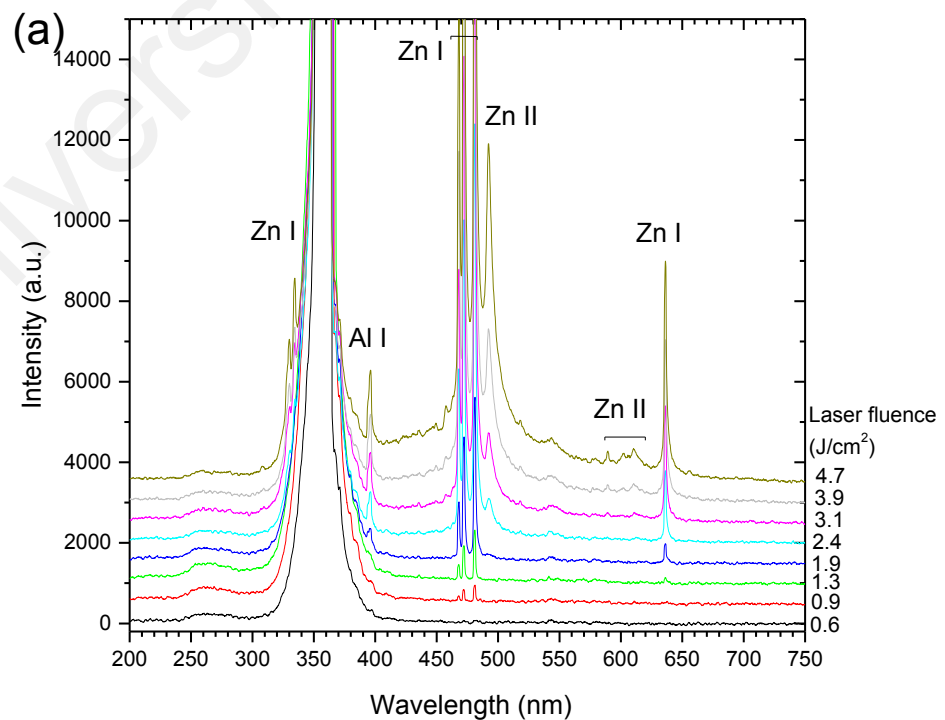


**Figure 4.1:** Optical emission spectra of the ablation of AZO target with (a) 355nm laser wavelength and (b) 532 nm laser wavelength.

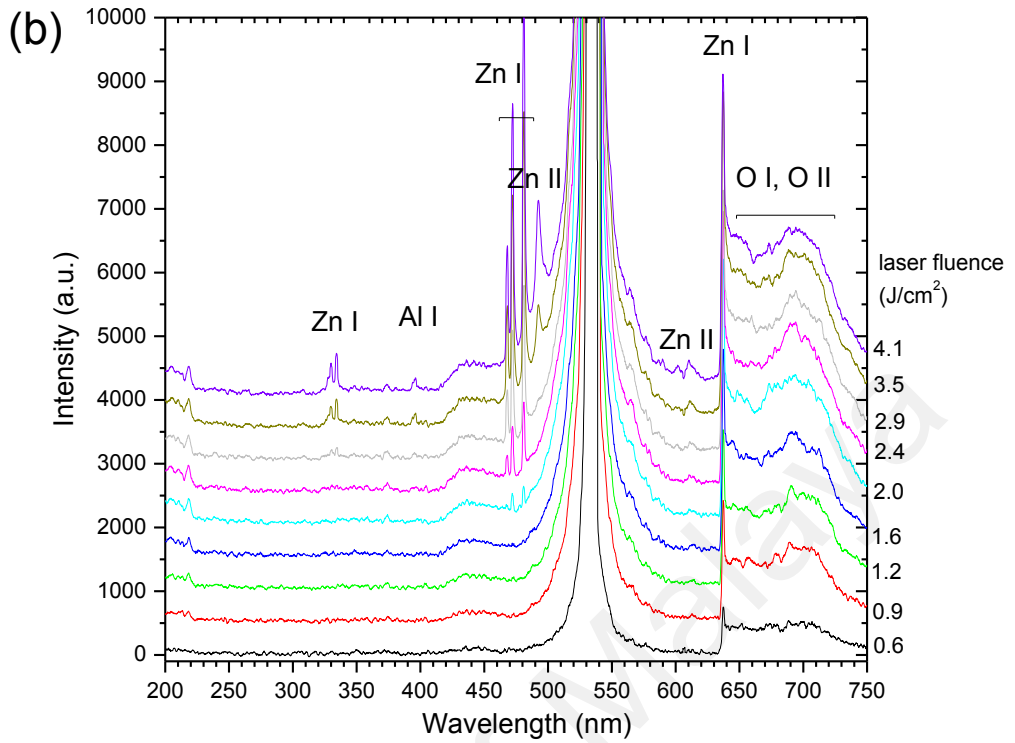


Figure: 4.1, continued.

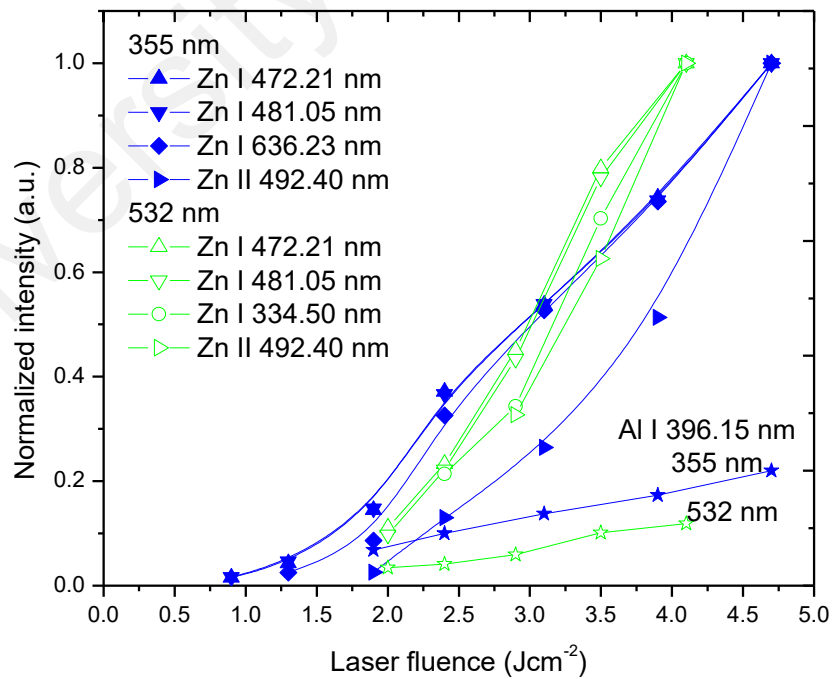
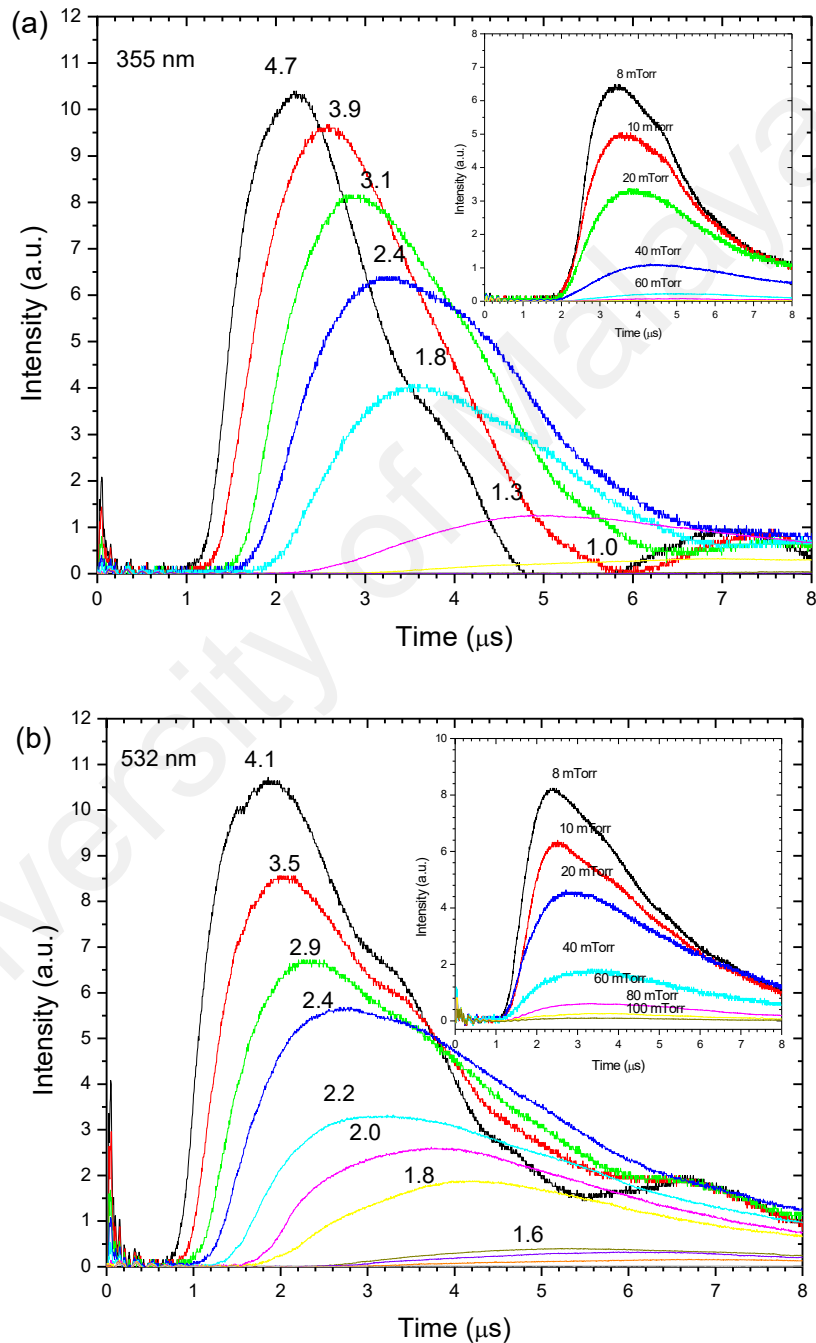


Figure 4.2: The normalized intensity of the characteristics line of Zn I (334.50nm, 472.21 nm, 481.05 nm, 636.23 nm) , Zn II (492.40 nm) and Al I (396.15 nm).

## 4.2.2 Time of flight measurement

The time of flight ion signals obtained in the experiments of 355 nm and 532 nm laser ablation of AZO are shown in Figure 4.3. Measurement was performed for laser fluences ranged from 0.6 to 4.7 J/cm<sup>2</sup>. Based on the values obtained from the graph, velocity and energy of the detected species is calculated and are shown in Table 4.1.



**Figure 4.3:** Time of flight signals of (a) 355 nm and (b) 532 nm laser ablation of AZO target at different laser fluence. Inserts show the ions signal measured at 2 J/cm<sup>2</sup> at different O<sub>2</sub> background pressure.

**Table 4.1:** Detailed parameters were used in Laser-produced plasma.

Laser Wavelength (nm)	Laser Fluence (J/cm <sup>2</sup> )	Time of species from target to substrates (us)	Velocity (km/s)	Average Energy (eV)
355	0.6	8.00	6.2	13.2
	0.9	6.89	7.26	17.9
	1.3	4.85	10.3	36.0
	1.9	3.51	14.2	68.0
	2.4	3.19	15.7	83.6
	3.1	2.81	17.8	107
	3.9	2.55	19.6	130
	4.7	2.22	22.5	172
532	0.6	7.20	6.94	16.3
	0.9	6.82	7.33	18.2
	1.2	5.93	8.43	24.1
	1.6	5.24	9.54	30.8
	2.0	4.00	12.5	52.9
	2.4	3.69	13.6	62.4
	2.9	2.68	18.7	119
	3.5	2.24	22.3	169
	4.1	2.01	24.9	210

The extracted ions velocity and energy are shown in Figure 4.4. The ions velocity and energy measured in O<sub>2</sub> were lower as compared to those measured in vacuum (10<sup>-6</sup> Torr). In the presence of O<sub>2</sub>, the velocity was 6 to 22 km/s. As laser fluence increased, faster ions were emitted in both cases and the velocity saturated at high laser fluence. In contrast to the effects of laser fluence, the change of O<sub>2</sub> pressure during ablation did not alter the ion energy significantly (inset of Figure 4.3). The O<sub>2</sub> pressure was varied from 5 mTorr to 100 mTorr, which is the typical range of thin film growth. When the background pressure decreased, only the intensity of the ions peak was increased; indicate that only the density of ions reaching the probe was changed. The velocity and thus the ions energy in 355 nm and 532 nm were comparable at low fluence (< 2 J/cm<sup>2</sup>) but it was higher for

532 nm ablation at high laser fluence. The measured ions energy in this work was below 500 eV which can cause defects in the growing films (Perrière et al., 2002).

As shown in Figures 4.4(a) and 4.4(b), as the laser fluence increased the velocity of the species increased too in both laser wavelength 355 nm and 532nm. However, in low fluency ( $< 2 \text{ J/cm}^2$ ), the velocity of species of the 355 nm are higher than the 532 nm. This is because, compared to the 532 nm laser, the photon energy of the 355 nm (3.49 eV) is higher and near to the bandgap of AZO. The higher photo energy by 355 nm able to ionize and to produce ions with higher velocity. At the same time, compare to the 532 nm, the higher photon energy of 355 nm produced higher intensity of the ions as shown in the Figure 4.4(c). In high fluence ( $> 2 \text{ J/cm}^2$ ), the total velocity and energy of the ions of 532 nm are higher than the species in 355 nm. That is because, as shown in Figure 4.4(c), the intensity of the ablated practices or ions increased with the laser fluence and the intensity of the ions is higher in 355 nm. Therefore, after the intensity in 355 nm is over a certain threshold, the probability of the ions scattering is higher in 355 nm. The high ions scattering reduced the total velocity of the ions in 355 nm and decreased the mean free path of the ions in 355 nm too. Overall, the total energy and velocity of the ablated practices in 532 nm laser is higher than the 355 nm.

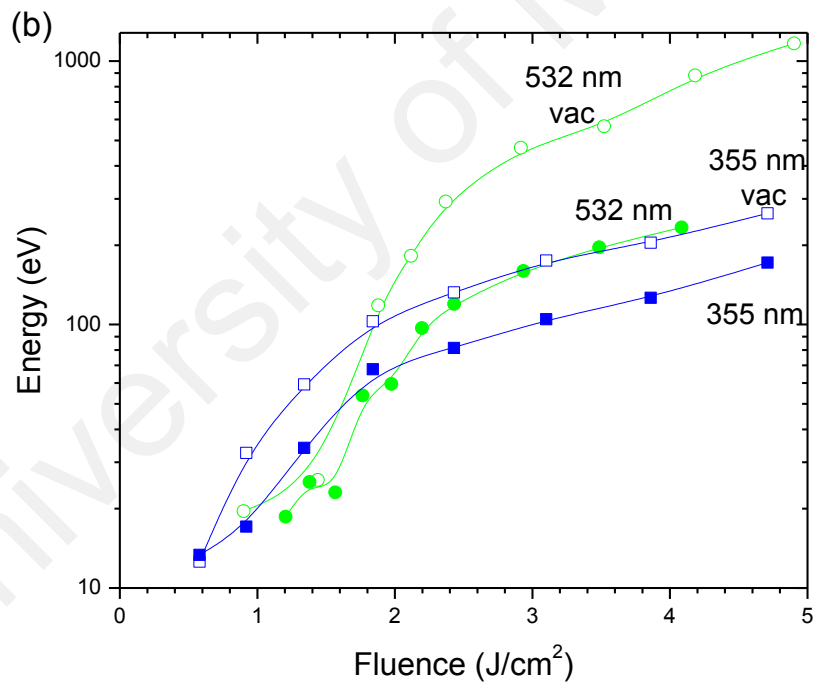
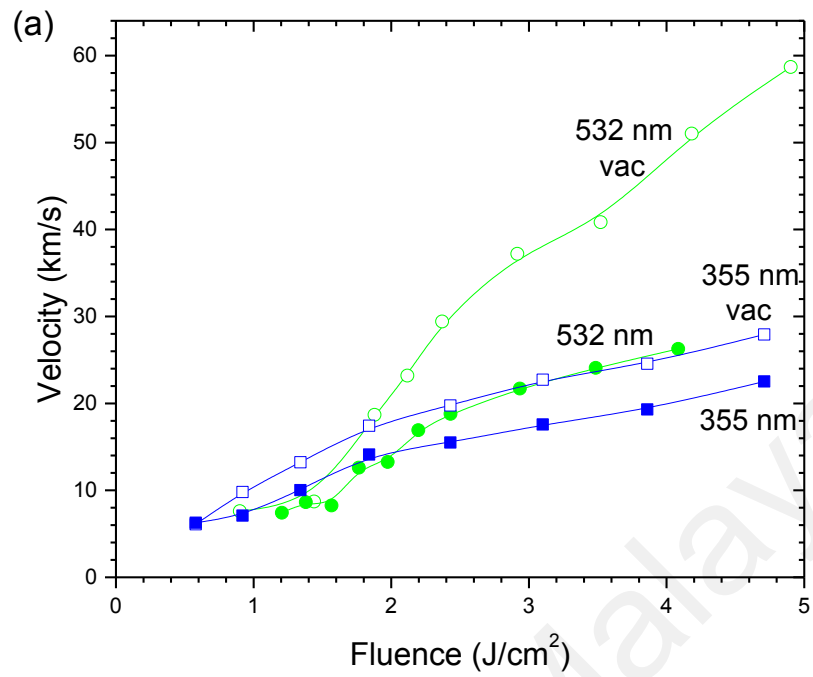


**Figure 4.4:** The 355 nm and 532 nm laser wavelength with different laser fluence: (a) Ion velocity, (b) Ion energy and (c) Ion intensity.

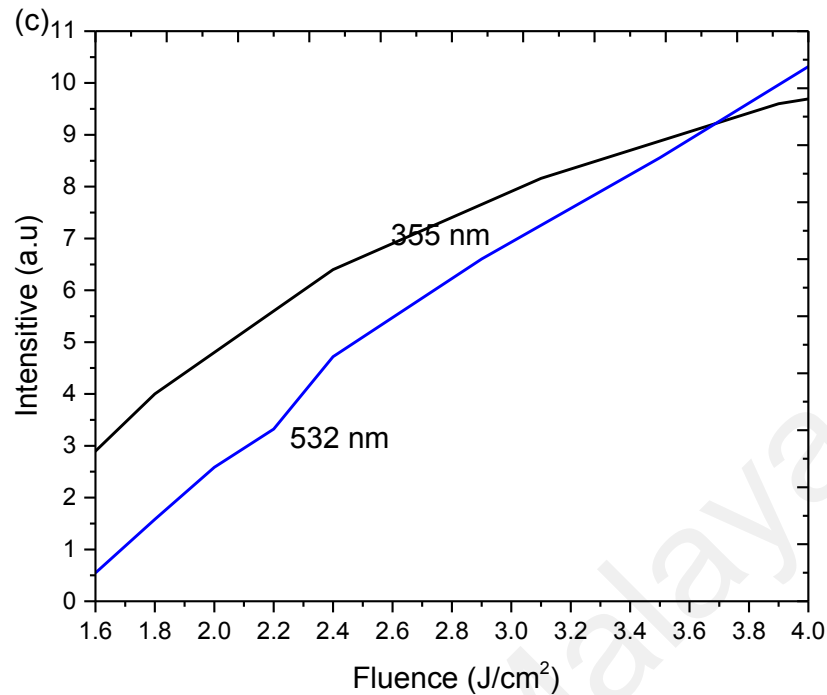


Figure 4.4, continued.

### 4.3 The Effects of Laser Fluence and Laser Wavelength on the properties of AZO films

AZO films are deposited by 355 nm and 532 nm at 2 J/cm<sup>2</sup> and 4 J/cm<sup>2</sup>, where Al species were detected in the optical emission spectra. The corresponding ions energy are summarized in Table 4.2.

#### 4.3.1 Ablation rate and growth rate

The depth of the ablation area created by different laser parameters and the thickness of the AZO films were measured by using a profilometer (Table 4.2). Based on the Dong et al., 2007, low resistivity ( $\approx 10^{-3}$  to  $10^{-4}$   $\Omega\text{cm}$ ) AZO thin films were obtained when the thickness of the AZO films were above 120 nm. However, the transmittance of the AZO films decreased as the AZO films becomes very thick. The ablation rate was 2 to 3 times higher for the ablation with 532 nm laser because the penetration depth of 532 nm laser is higher.

**Table 4.2:** The ablation rate and thickness of the AZO thin films.

Laser wavelength (nm)	Laser Fluence (J/cm <sup>2</sup> )	AZO target	AZO films	
		Ablation Rate (μm/min)	Thickness (nm)	Growth rate (nm/min)
355	2	1	90 ± 5 %	2.0 ± 5 %
	4	1.3	132 ± 5 %	2.9 ± 5 %
532	2	2.2	100 ± 5 %	2.2 ± 5 %
	4	3.3	191 ± 5 %	4.2 ± 5 %

### 4.3.2 Surface Morphology

Figures 4.5 to 4.8 show the AFM images of the AZO thin films deposited at 2 J/cm<sup>2</sup> and 4 J/cm<sup>2</sup> by 355 nm and 532 nm lasers. The AFM images were obtained for AZO films on p-Si (100) substrate. Nanostructural surface were observed, where the size of nanostructures increased with laser fluence and wavelength. The roughness of AZO thin film is shown in Table 4.3. The roughness of AZO thin film deposited by 532 nm is higher than the 355 nm. The high penetration depth of 532 nm laser results in severe melting and splashing of large droplet instead of atomizing the AZO target (Kek et al., 2016). 355 nm laser produced more ionized and atomized species as shown in the Section 4.1. Longer laser wavelength also leads to high plasma attenuation and radiation heating. In the report by Tunna et al., 2001, radiation heating of the plasma was higher in 532 nm than 355 nm. The heat can be transferred to the surface of the material and contribute to melting of the surface.

The AZO films deposited at 2 J/cm<sup>2</sup> (Figure 4.5) is smoother as compare to 4 J/cm<sup>2</sup> (Figure 4.6). The same trend was observed for 532 nm laser deposition where AZO film in Figure 4.7 is smoother than Figure 4.8. Both of the laser wavelength (355 nm and 532 nm) have shown that 2 J/cm<sup>2</sup> laser fluence produced smoother AZO thin film than 4 J/cm<sup>2</sup>.

In the report by Girtan et al., 2013, the roughness of the thin films increases as the laser fluence increases because thermal effect and the deposition rate. In the Chapter 4.1, the ablation rate and the kinetics of the ablated species are higher in  $4 \text{ J/cm}^2$  as compare to the  $2 \text{ J/cm}^2$ , the higher kinetics of the ablated species introduced the higher deposition rate. The higher deposition rate increases the roughness of the thin film, this explained in the research of Girtan et al., 2013 also. The thermal effect at the higher fluence may influence the thin film roughness too.

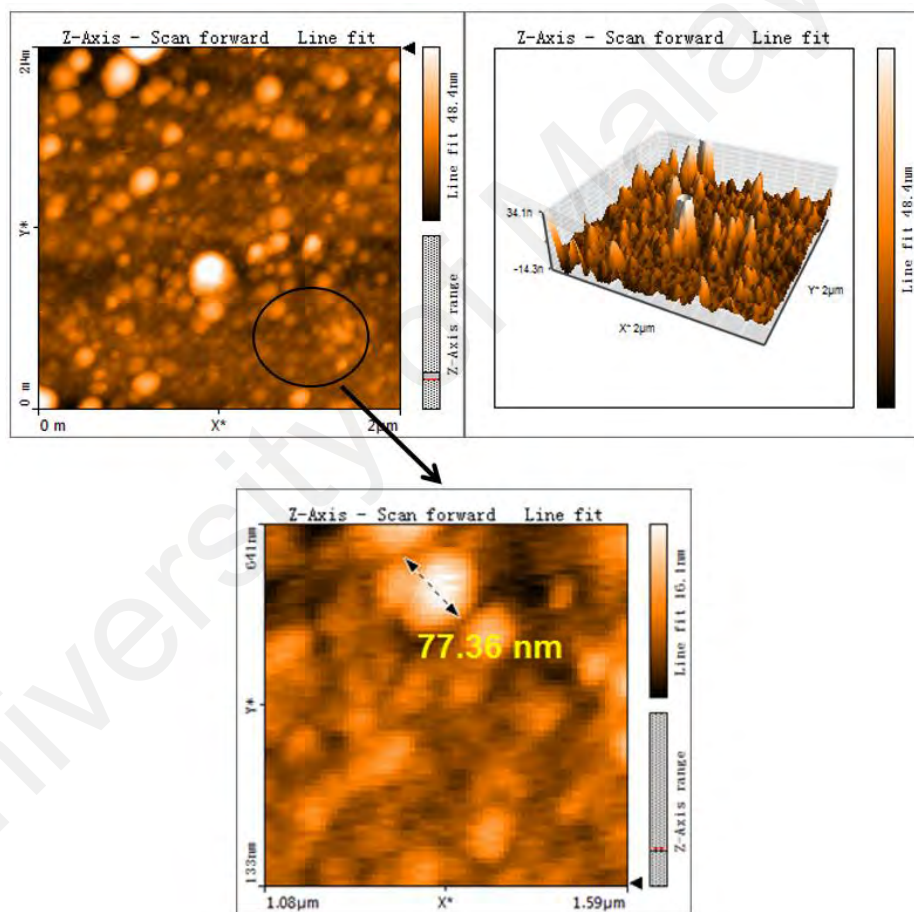


**Figure 4.5:** AFM images of the AZO thin Films deposited in 355nm ( $2 \text{ J/cm}^2$ ).

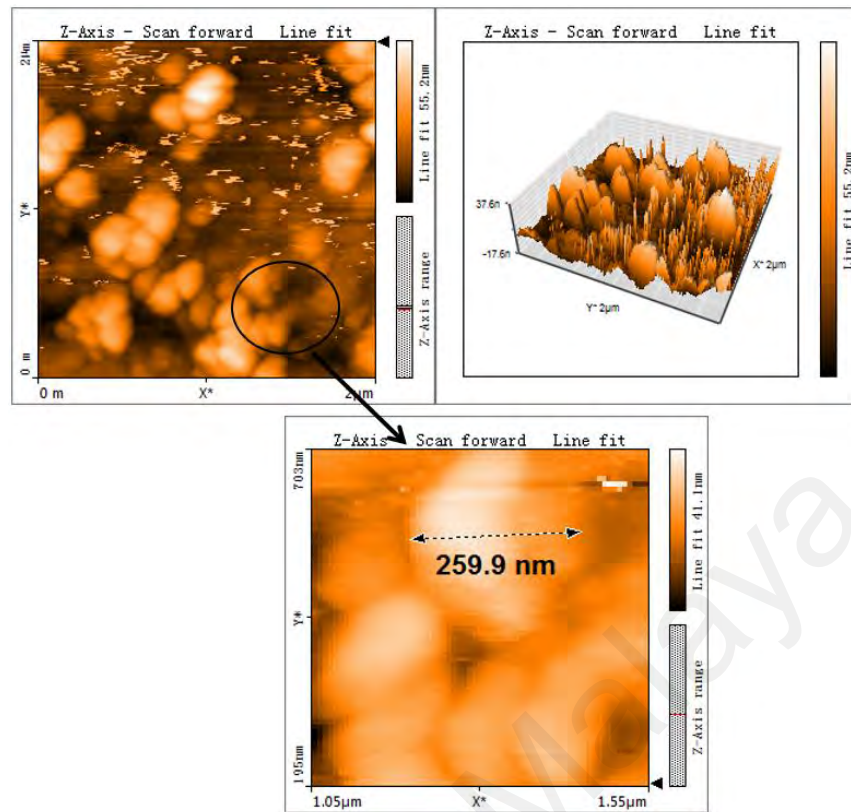


**Figure 4.6:** AFM images of the AZO thin Films deposited in 355nm ( $4 \text{ J/cm}^2$ ).

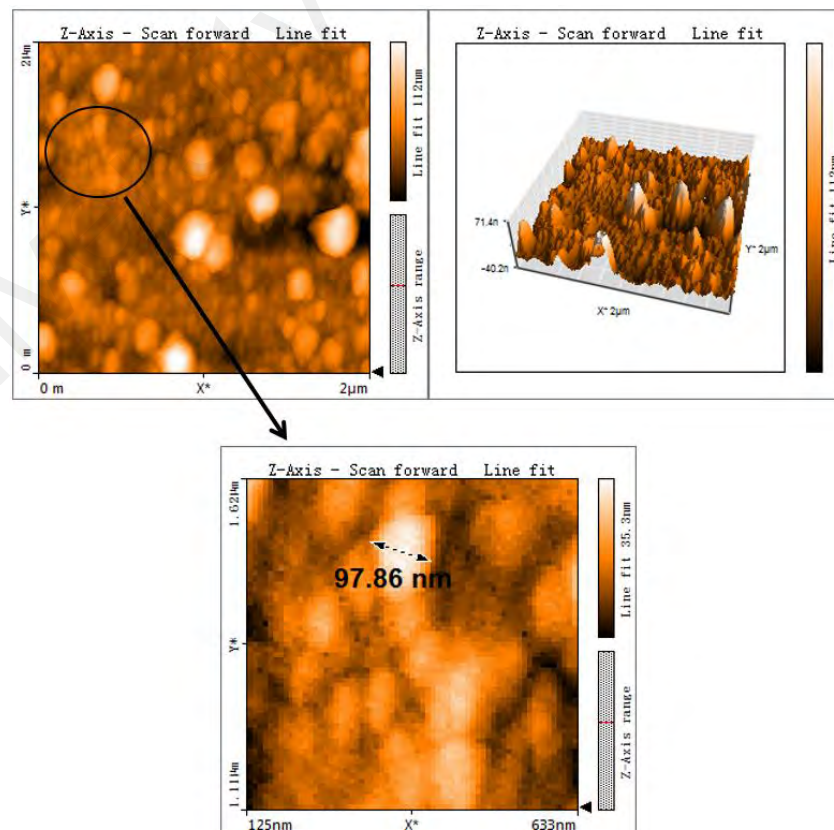


**Figure 4.7:** AFM images of the AZO thin Films deposited in 532 nm ( $2 \text{ J/cm}^2$ ).

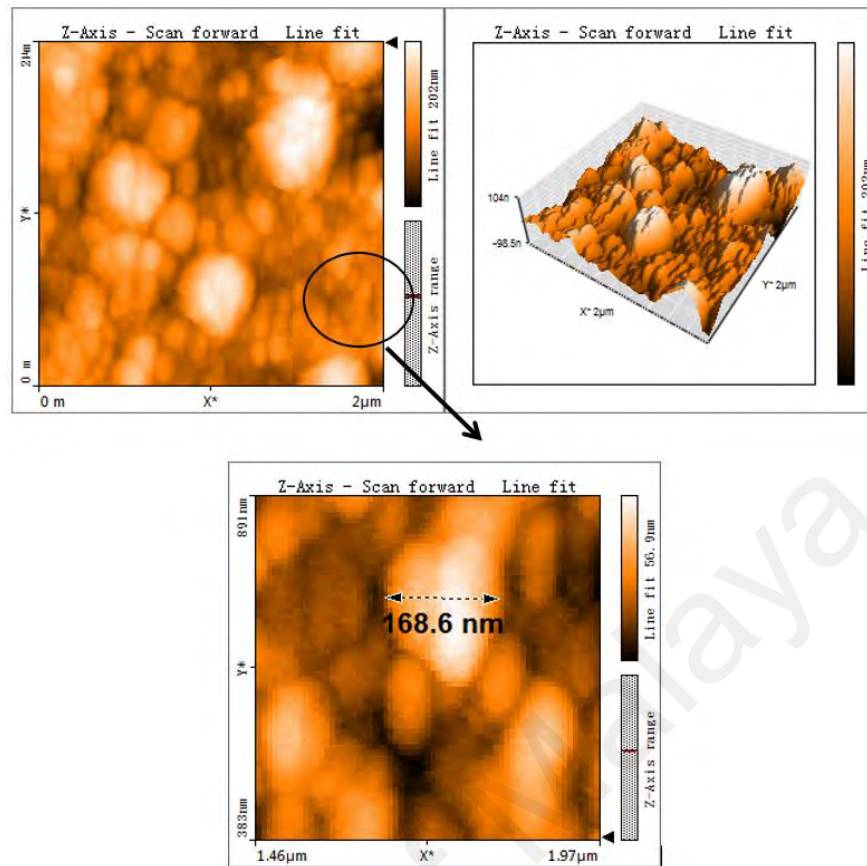


**Figure 4.8:** AFM images of the AZO thin Films deposited in 532 nm ( $4 \text{ J/cm}^2$ ).

**Table 4.3:** Detailed of the AZO thin films roughness in different laser parameter.

Laser wavelength (nm)	Laser Fluence ( $\text{J/cm}^2$ )	Root Mean Square Roughness (nm)	Mean Roughness (nm)	Grain Size (nm)
355	2	$6.3 \pm 5 \%$	$4.2 \pm 5 \%$	$77.36 \pm 10 \%$
	4	$10.3 \pm 5 \%$	$8.3 \pm 5 \%$	$259.9 \pm 10 \%$
532	2	$14.8 \pm 5 \%$	$10.2 \pm 5 \%$	$97.9 \pm 10 \%$
	4	$33.6 \pm 5 \%$	$25.9 \pm 5 \%$	$168.6 \pm 10 \%$

SEM images of the AZO films are shown in Figures 4.10 to 4.13. Particulates were observed on the samples. The EDX spectra are shown in Figure 4.10(b) to 4.13(b). Al, Zn and O elements were detected indicating the incorporation of the element in the films. The intensity of Al in the films are shown in Figure 4.9. As shown in Figure 4.9, the percentage of the Al in the thin films will lower than target (Liu & Lian, 2007) .

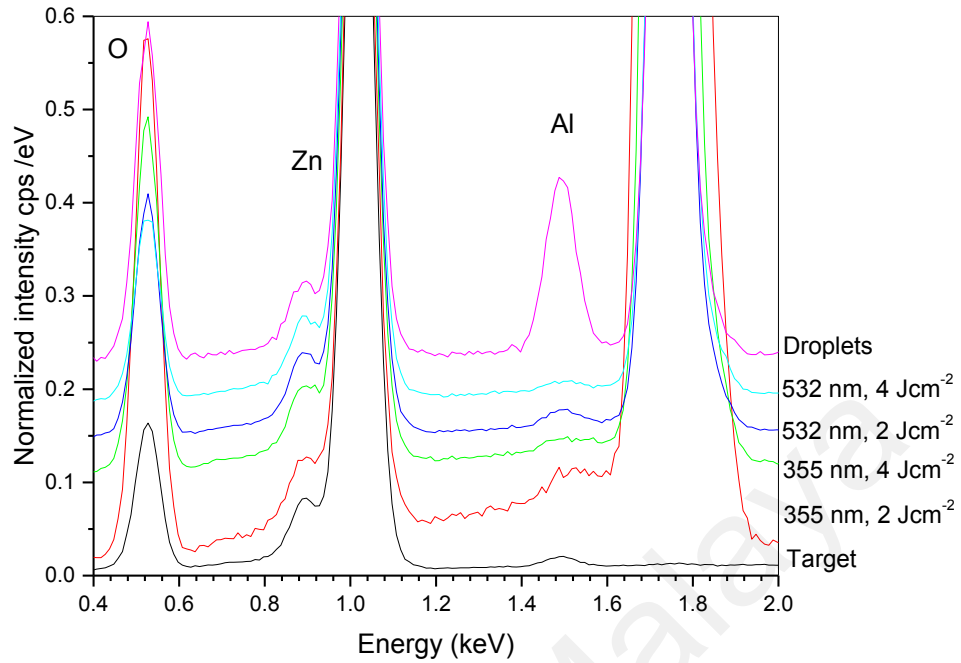


**Figure 4.9:** Intensity of Al in the film

However, EDX mapping shows the micro-sized particles contained high density of Al (Figures 4.10(c), 4.11(c), 4.12(c), and 4.13(c)). The AZO films deposited by 532 nm laser are rougher and contained higher density of Al-rich droplet as shown in Figure 4.12(c) and 4.13(c). The formation of the Al-droplets maybe related to the lower efficiency of the laser source to atomize Al elements; the Al-rich droplets were directly ejected by 532 nm laser where melting occurred. The aggregation of Al in the droplets indicates the consumption of the elements from the target during ablation into the form of droplets, which would result in non-homogeneous distribution of Al in the final films. The AZO films deposited in 355 nm laser wavelength and 2 J/cm<sup>2</sup> shown the smoothest and distributed elements films.

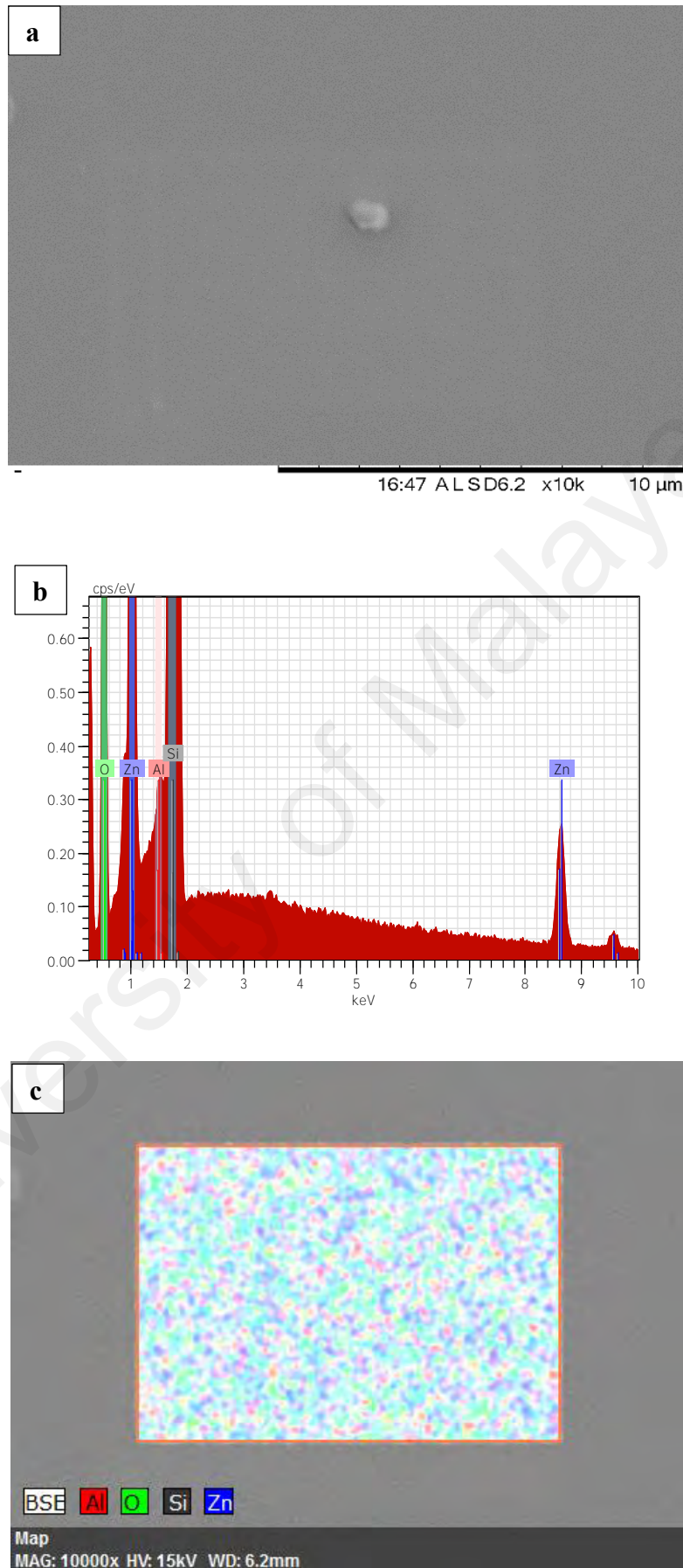


**Figure 4.10:** (a) SEM image (b) EDX spectra of AZO films and (c) AZO mapping image from EDS analyst of the AZO films deposited at  $2 \text{ J/cm}^2$ , 355 nm laser wavelength.

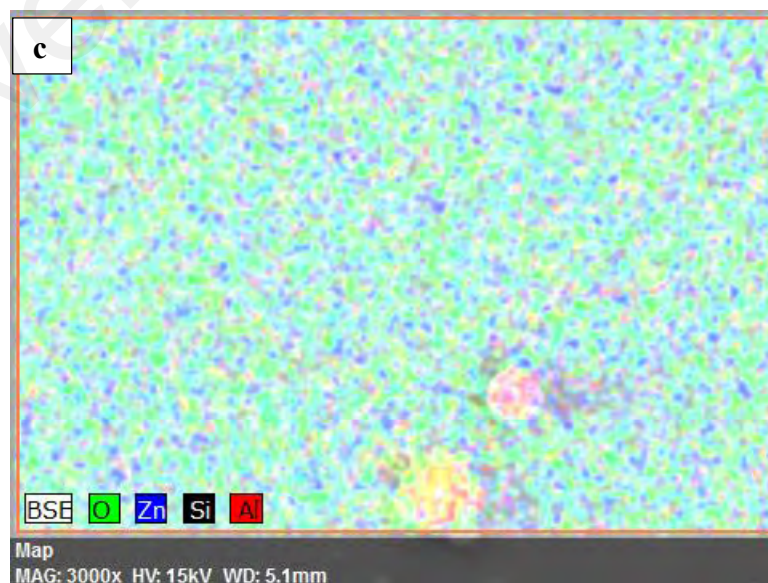
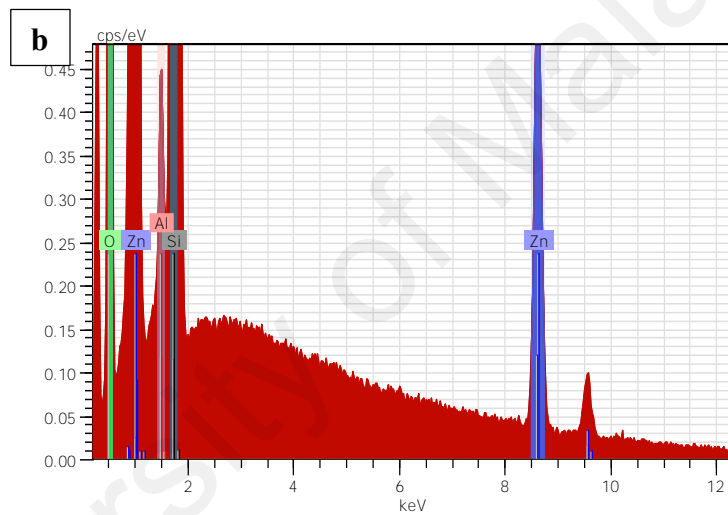
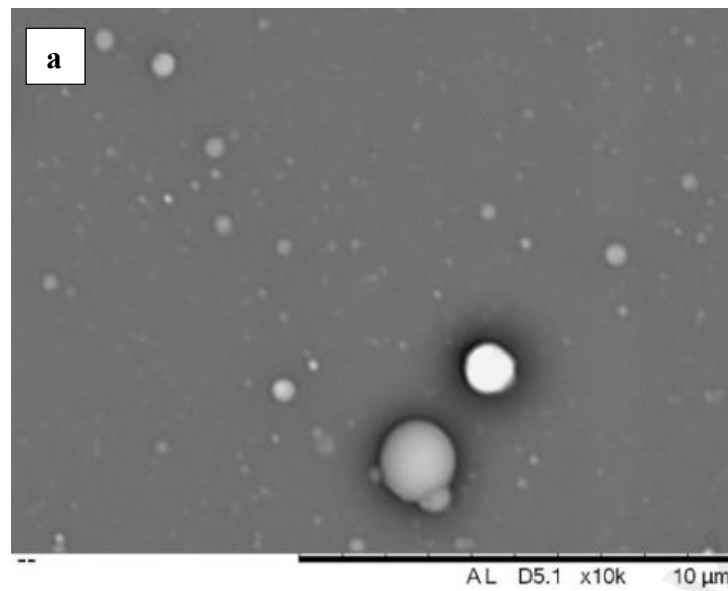


**Figure 4.11:** (a) SEM image (b) EDX spectra of AZO films and (c) AZO mapping image from EDS analyst of the AZO films deposited at  $4 \text{ J/cm}^2$ , 355 nm laser wavelength.

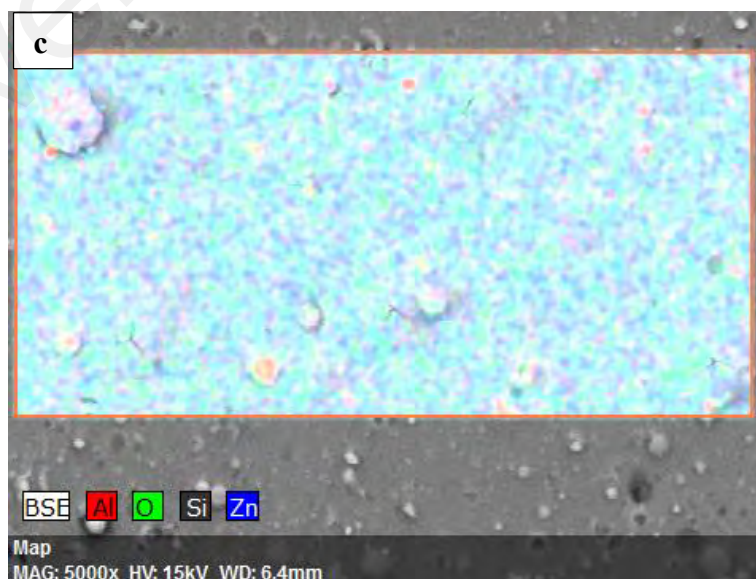
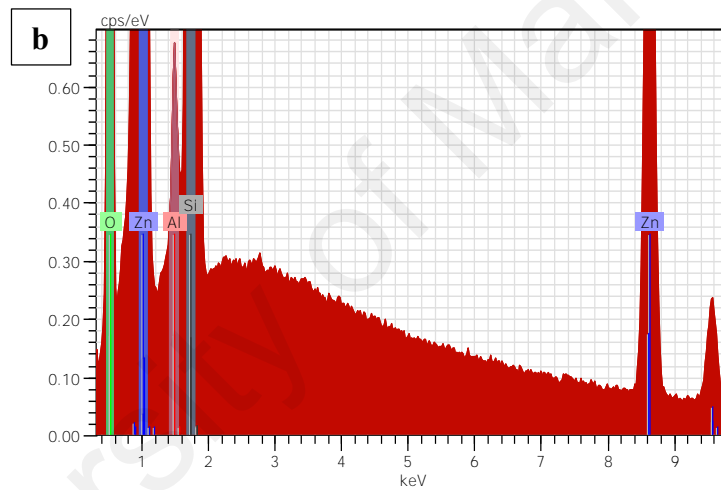
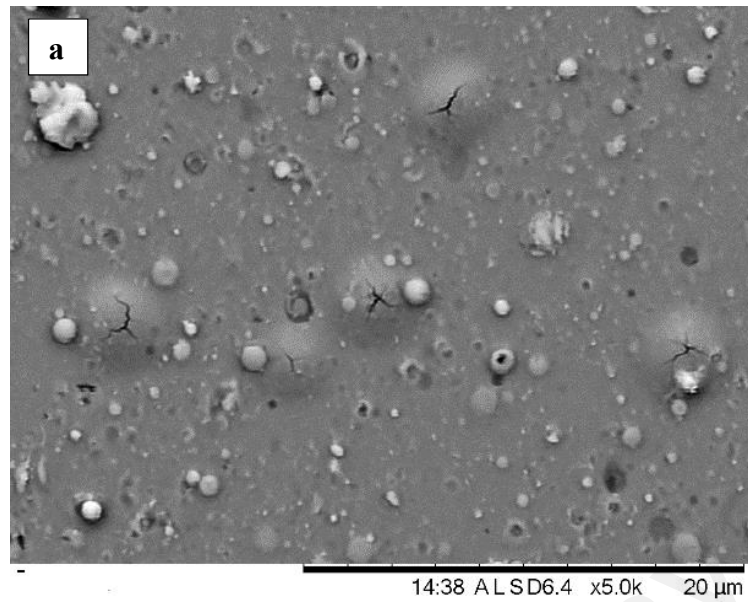


**Figure 4.12:** (a) SEM image (b) EDX spectra of AZO films and (c) AZO mapping image from EDS analyst of the AZO films deposited at  $2 \text{ J/cm}^2$ , 532 nm laser wavelength.

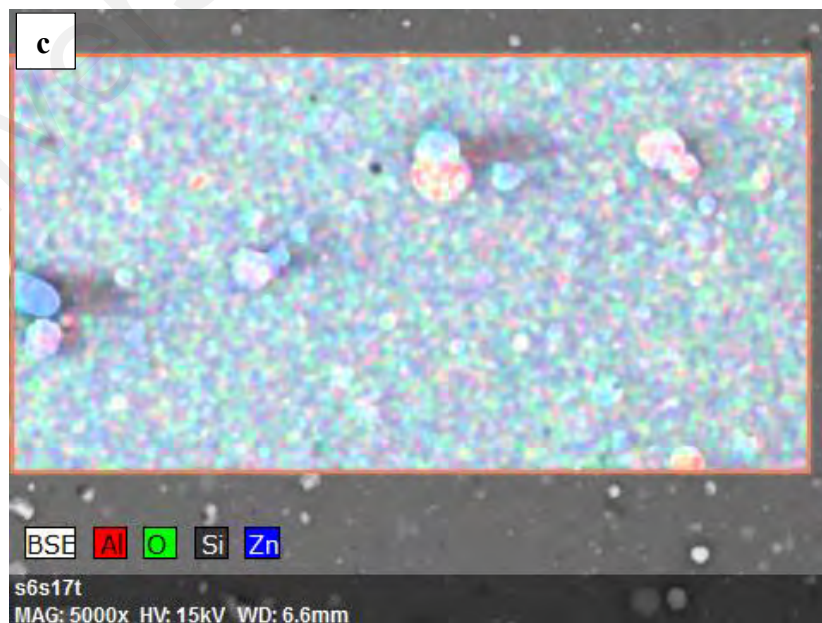
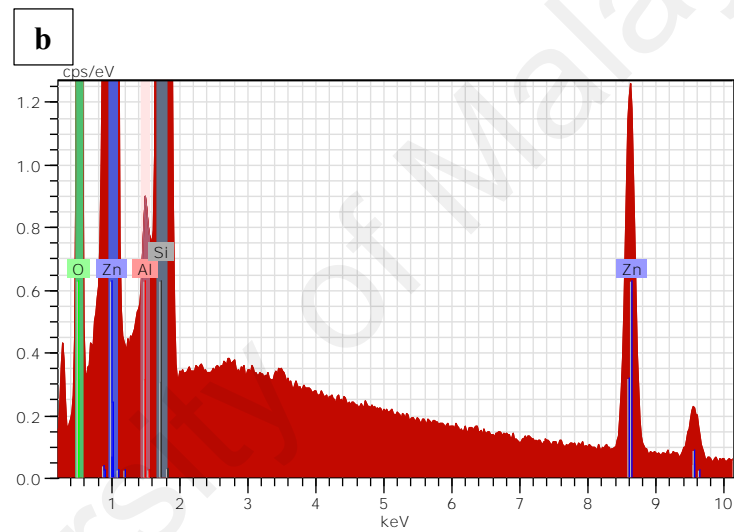
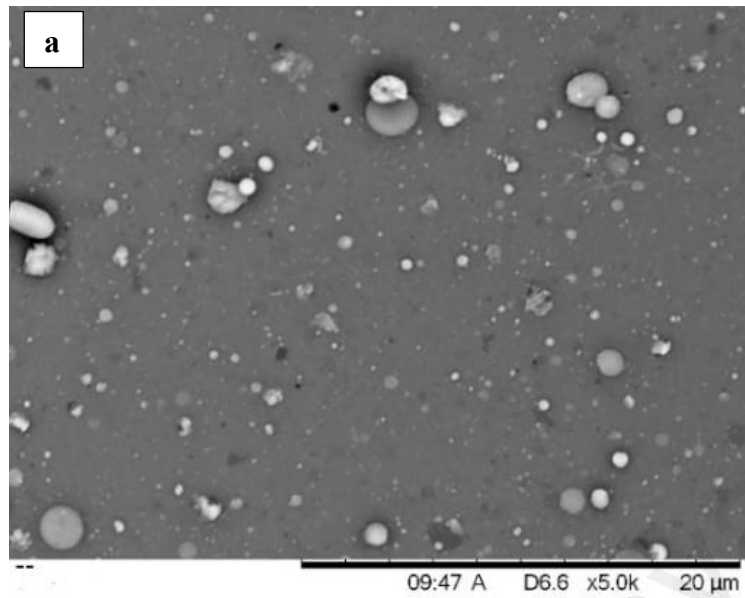


**Figure 4.13:** (a) SEM image (b) EDX spectra of AZO films and (c) AZO mapping image from EDS analyst of the AZO films deposited at  $4 \text{ J/cm}^2$ , 532 nm laser wavelength

### 4.3.3 Crystallinity

XRD was used to measure the crystal structure properties of AZO from  $30^\circ$  to  $70^\circ$ . As shown in Figure 4.14, all the AZO films show the (002) peak at  $34^\circ$  in XRD, (002) peak of the AZO films indicate that all the films are c-axis oriented crystal structure. Additional peaks of (101) at  $36^\circ$  and (103) at  $62^\circ$  are also detected but less intense than that of the (002) peak, indicating a preferential c-axis oriented crystal structure. The presence of sharp peaks indicated the crystalline domains, as shown in Figure 4.14.

Smaller FWHM originated from better crystalline AZO with uniformly c-axis orientation direction (Garcés et al., 2015). Therefore, AZO films deposited in  $2 \text{ J/cm}^2$  (355 nm) shown the best crystalline quality when compare to other samples in this experiment.

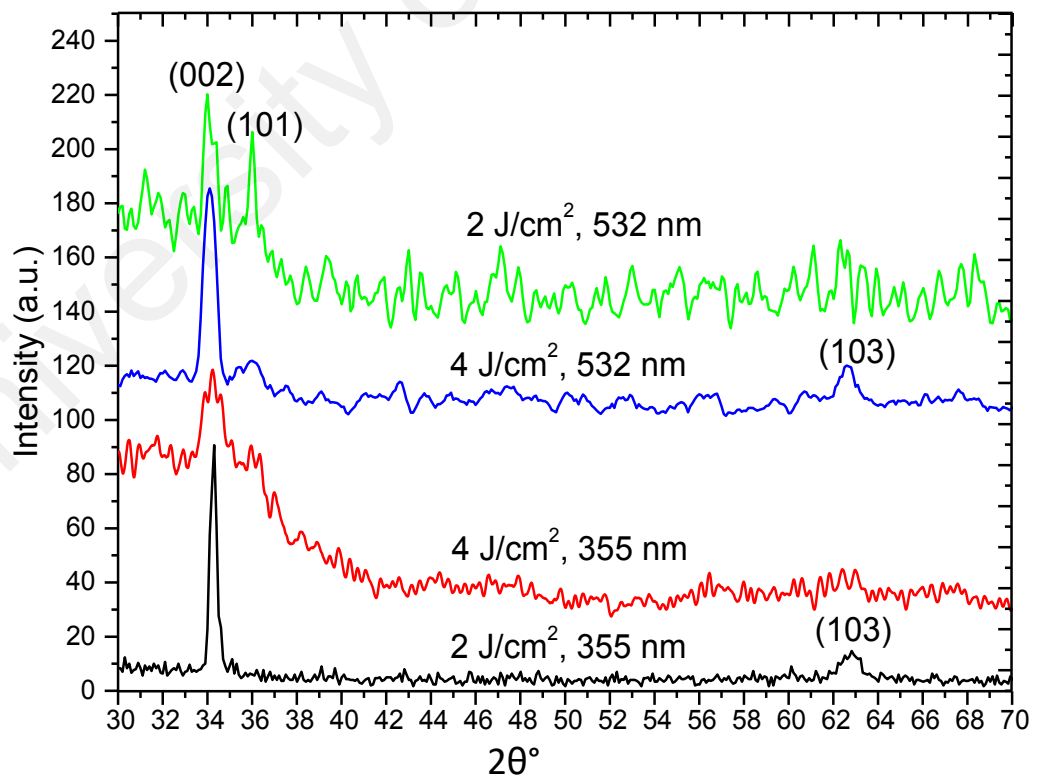


**Figure 4.14:** XRD spectra of AZO films deposited on glass with different laser parameters.

#### 4.3.4 Optical Properties

Figure 4.15 shows the effect of laser wavelength and the laser fluence on the optical transmittance and optical absorbance of the AZO. Comparing the transmittance of AZO produced in 355 nm and 532 nm, it is found that the average transmittance of AZO thin films in 532 nm was above 60 % whereas the average transmittance of AZO thin films in 355 nm was above 80 %. The average of the transmittance of 355 nm is higher than the 532 nm, due to the smoother morphology of the 355 nm. As fluence increased, the transmittance deteriorated too as shown in Table 4.3, the roughness of the AZO film in 4 J/cm<sup>2</sup> is two times higher than the film 2 J/cm<sup>2</sup>.

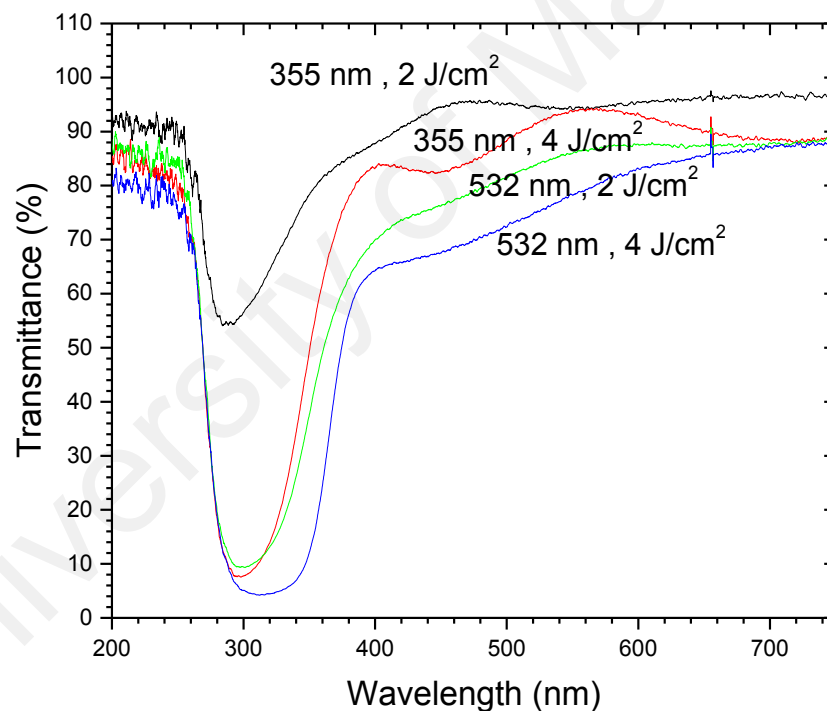


**Figure 4.15:** Optical transmittance of AZO thin films deposited in different laser parameters.

The optical bandgap of AZO films in this report are determined by the Tauc plot with the data obtained from UV-vis spectrophotometry. In the Tauc plot (Tauc, 1969) method, the optical bandgap for the AZO can be obtained by using the Equation 4.1:

$$(\alpha h\nu)^2 \approx (h\nu - E_g) \quad (4.1)$$

where  $h\nu$  is photo energy and  $\alpha$  is absorption coefficient and it can be expressed as:

$$\alpha = -\ln(T)/d \quad (4.2)$$

From the Equation 4.2, the absorption coefficient  $\alpha$  is related to the thickness of the thin film  $d$  and optical transmittance  $T$ . The absorption coefficient of the four samples are plotted according to the Tauc plot method based on the Equation 4.1 as shown in Figure 4.1. The optical bandgap of the samples is obtained by extrapolating linear line gradient of the curve to the zero absorption ( $\alpha h\nu = 0$ ) as shown in the Figure 4.16. In  $2 \text{ J/cm}^2$ , the optical bandgap of AZO produced by 355 nm obtained is  $\approx 3.45 \text{ eV}$  and the optical bandgap of AZO produced by 532 nm obtained is  $\approx 3.52 \text{ eV}$ . In  $4 \text{ J/cm}^2$ , optical bandgap of AZO are  $\approx 3.6 \text{ eV}$  for 355nm and  $\approx 3.38 \text{ eV}$  for 532 nm. These values are higher than the optical bandgap of the pure ZnO in room temperature which is  $3.3 \text{ eV}$ , indicating that the films are successfully doped with Al.

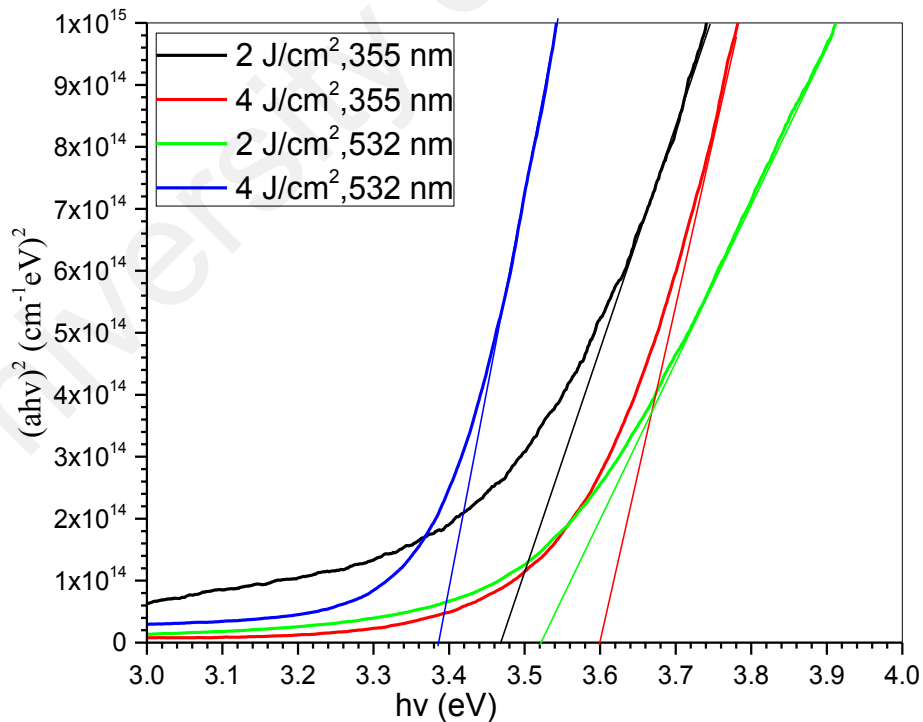


**Figure 4.16:** Optical absorption coefficients of AZO thin films in function of photon energy for different laser parameters.

### 4.3.5 Electrical Resistivity

Resistivity of the films are measured by four-point probe, the working principle and related equations had been explained in Chapter 3.4.5. Table 4.4 shown the resistivity result in this experiment:

**Table 4.4:** The detailed of the resistivity of the AZO thin films.

Laser Wavelength (nm)	Laser Fluence (J/cm <sup>2</sup> )	Resistivity ( $\Omega$ cm <sup>-1</sup> )	Thickness (nm)
355	2	$1.3 \times 10^{-3}$	$90 \pm 5$ %
	4	1.9	$132 \pm 5$ %
532	2	$1.5 \times 10^{-2}$	$100 \pm 5$ %
	4	$5.8 \times 10^{-1}$	$191 \pm 5$ %

Compare the effect of laser wavelength in the resistivity of the films, both 355 nm and 532 nm shown the almost same result but 355 nm 2 J/cm<sup>2</sup> is the lowest. This can be explained according to the equation  $\sigma = n e \mu$ , the electrical resistivity of AZO thin films is depending on two competitive effect: carrier concentration and mobility of carrier. Based on the research of Dong et al., 2007 and Tanaka et al., 2004, carrier concentration increase with the thickness of the thin films. Therefore, in this experiment, the carrier concentration of the AZO thin films deposited in 532 nm laser wavelength may higher than the carrier concentration of the AZO films deposited in 355 nm due to the thickness of the AZO films deposited in 532 nm are thicker than the AZO films in 355 nm as shown in Table 4.4. However, due to the high roughness morphology and high quantity of the droplet of the AZO films in 532 nm, the mobility of the carriers in 532 nm may slower than the mobility of the carriers in 355 nm. The lower mobility of the carrier may due to the scattering of the carriers. The AZO films in 355 nm is smoother and thinner when compare to the AZO films in 532 nm. Therefore, according to the explanation of Dong et

al.,2007, less carrier concentration in thinner AZO films and due to the smoother morphology of AZO films in 355 nm, the mobility of carrier may higher.

Compare the effect of laser fluence in the resistivity of the AZO thin films, the resistivity of AZO thin films deposited in  $2 \text{ J/cm}^2$  was lower than the resistivity of the AZO films deposited in  $4 \text{ J/cm}^2$ , in both 355 nm and 532 nm as shown in Table 4.4. According to the research of Agura et al., 2003, the resistivity increase with the laser fluence increase. In the research of Holmelund et al., 2002, the lowest resistivity of ITO thin films were gained in the laser fluence  $1.5 \sim 2.1 \text{ J/cm}^2$ . Based on the results in Chapter 4.1, the Al-elements were ablated when the laser fluence was near  $2 \text{ J/cm}^2$ , and based on the Figure 4.5 and 4.10, the AZO thin films deposited in  $2 \text{ J/cm}^2$  shown the smoother and higher element distribution. The smoother and higher element distribution prove that the AZO films deposited in  $2 \text{ J/cm}^2$  is a higher quality films when compare to the  $4 \text{ J/cm}^2$ .

#### **4.4 Summary**

The ablation and deposition of AZO films from 355 nm and 532 nm differs in the plasma generation process and thus the films deposition. Our results show that the ablation rate of 532 nm was two times higher than in 355 nm. The optical absorption coefficient of AZO films by 355 nm laser was measured to be about 1 order of magnitude higher than that of a 532 nm. Thus, a smaller laser penetration depth and higher power density was obtained in 355 nm laser ablation. The growth rate of the films is usually proportional to the penetration depth, thus we observed the films deposited by 532 nm laser to be thicker. However, the films with 355 nm laser is thinner than typical 248 nm laser ablation (Park et al., 2006). The results suggest of an additional mechanism in the process which photons are absorbed to produce PL from the target. The laser photon with energy of 3.49 eV is close to the energy band gap of the AZO target induced optical

excitation with radiative emission (Jin et al., 2001; Thareja & Mitra, 2000). This was confirmed in a separate experiment performed in air. Room temperature photoluminescence were obtained perpendicular to the target with an unfocused 355 nm laser beam at an incident angle of 45° (Figure 4.17). Emission at ~ 375 nm to 380 nm is due to photoluminescence of AZO target. The threshold laser fluence the photoluminescence peak was fairly low ~ 0.01 J/cm<sup>2</sup>, thus the optical excitation reduced the growth rate by 355 nm laser. However, the higher photon energy by 355 nm laser produced species with higher ionized states at lower fluence. It is also able to produce ions with energy up to 200 eV.

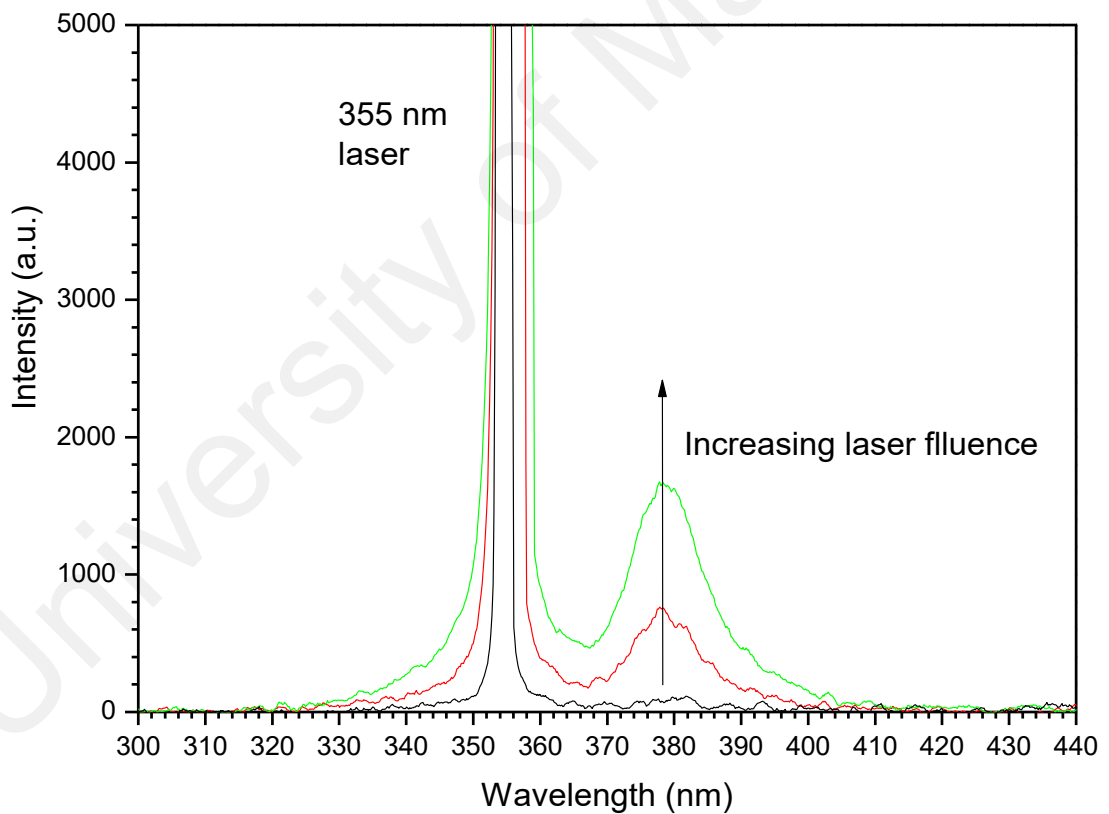


**Figure 4.17:** Photoluminescence spectra detected by 355 nm laser excitation of AZO target.

In terms of films properties, some conditions for optimized growth have been identified. It is required to keep the laser fluence and the penetration depth low to avoid micro-droplets generation. The presence of droplets does not only affect the films homogeneity as a whole, but the droplets also composed of the less-ablated element on the target such that the distribution of element in the films was affected. At the same time, the laser fluence should be sufficient to produce plasma from all the elements in the target. Congruent ablation ideally produced stoichiometry films but preferential ablation occurred. In 355 nm laser ablation, it was observed that at low fluence, ionized plasma with adequate kinetic energy can be produced. This has led to nanostructural AZO films growth at room temperature with the resistivity of  $10^{-3}$   $\Omega\text{cm}$ . The nanostructural films maybe useful to as it increases the surface area for contact as compared to a smooth surface. On the other hand, as the Al content in the films were lower than the ideal value because of the inefficiently in Al ablation, it is possible to use a AZO target with higher Al concentration such that even lower resistivity can be achieved.

**Table 4.5:** Summary of laser parameters, ions and thin films properties in this work.

Laser			Ion properties		Thin film properties			
Wavelength (nm)	Fluence ( $\text{J}/\text{cm}^2$ )	Ablation rate ( $\mu\text{m}/\text{min}$ )	Velocity (km/s)	Energy (eV)	Thickness (nm)	Resistivity ( $\Omega\text{ cm}$ )	Bandgap (eV)	Al/Zn ratio
355	2	1.0	14	64	90	$1.3 \times 10^{-3}$	3.45	0.020
	4	1.3	20	140	132	1.9	3.60	0.026
532	2	2.2	14	58	100	$1.5 \times 10^{-2}$	3.53	0.034
	4	3.3	26	230	191	$5.8 \times 10^{-1}$	3.40	0.035

Plasma characteristics of pulsed 355 nm and 532 nm laser were revealed in the deposition of AZO thin films. In typical grown conditions of laser fluence and  $\text{O}^2$  background gas at room temperature, the difference in laser wavelength affected the

ablation mechanisms and thus the deposited materials. Zn, Al and O species were detected above  $0.9 \text{ J/cm}^2$  for 355 nm laser ablation and above  $2 \text{ J/cm}^2$  for 532 nm laser ablation. At  $2 \text{ J/cm}^2$ , both 355 nm and 532 nm laser produced ion with similar kinetic energy ( $\sim 60 \text{ eV}$ ), but 355 nm laser ablation led to higher ionized species in the plasma plume for the growth of high transmittance nanostructured films while 532 nm laser resulted in nano and micro-particulates growth. In addition, increasing the laser fluence produced more droplets and ions with higher energy ( $> 200 \text{ eV}$ ) that is close to the defect generation limit of the films for 532 nm laser. Thus, despite a lower growth rate due to smaller penetration depth and some contribution of laser energy towards optical excitation, the AZO films deposited at 355 nm have better film homogeneity, larger optical bandgap and lower resistivity. For 532 nm laser deposition, the ablation process involves a dominant process of subsurface explosion that results in large particles and droplets generation in addition to energetic ions emission.

## CHAPTER 5: AZO/P-SI HETEROJUNCTION CHARACTERISTICS

### 5.1 Introduction

In this Chapter 5, the AZO thin films were deposited by PLD on p-Si (100) to form AZO/p-Si heterojunction. The J-V characteristics of the heterojunction and the response to illumination in UV and visible are discussed.

### 5.2 Properties of AZO samples and fabrication of AZO/p-Si structure heterojunction

Four samples consisting of AZO films deposited by 355 nm and 532 nm laser (S1, S2, S3 and S4) with different thickness (191 nm to 260 nm) are used in the fabrication of AZO/p-Si heterojunction. Figure 5.1(a) and 5.1(b) show the transmittance and absorption coefficient of the samples. Based on the Tauc plot in Figure 5.2, the optical bandgap are estimated. The properties of the samples are summarized in Table 5.1. The resistivity of the samples was measured by using 4-point probe. The results are shown in Figure 5.3 to 5.4.

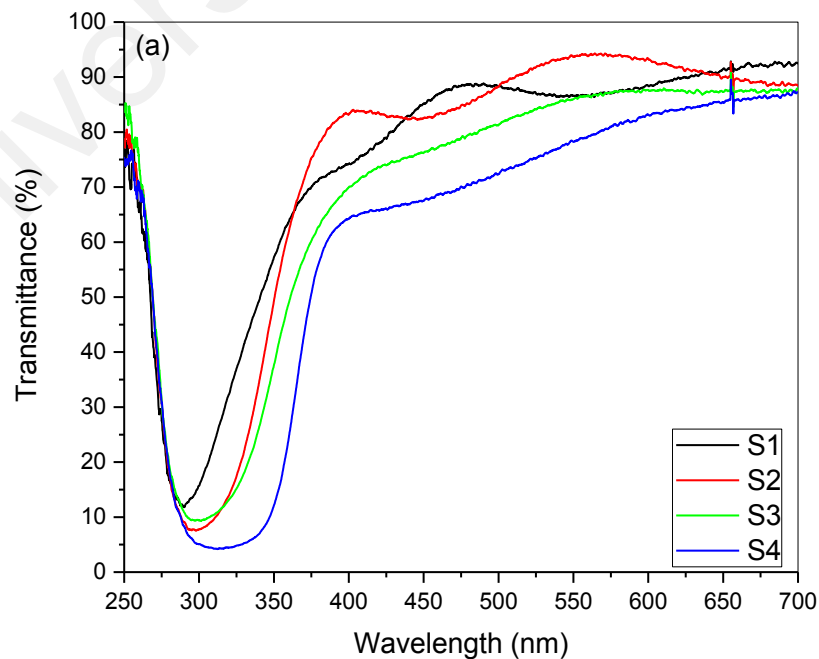


**Figure 5.1:** Optical properties AZO films deposited in different laser parameters: (a) Optical transmittance and (b) Optical absorption.

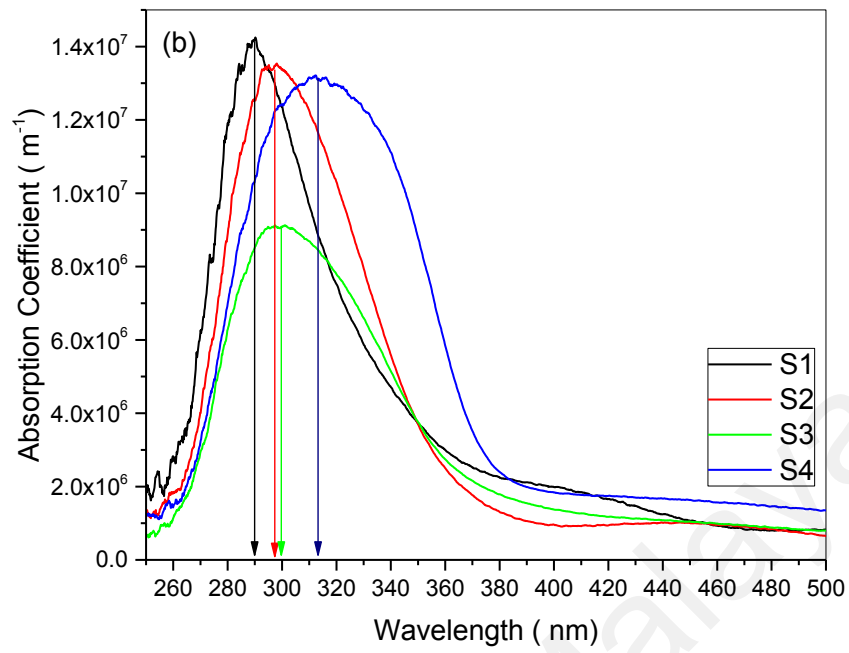


Figure 5.1, continued.

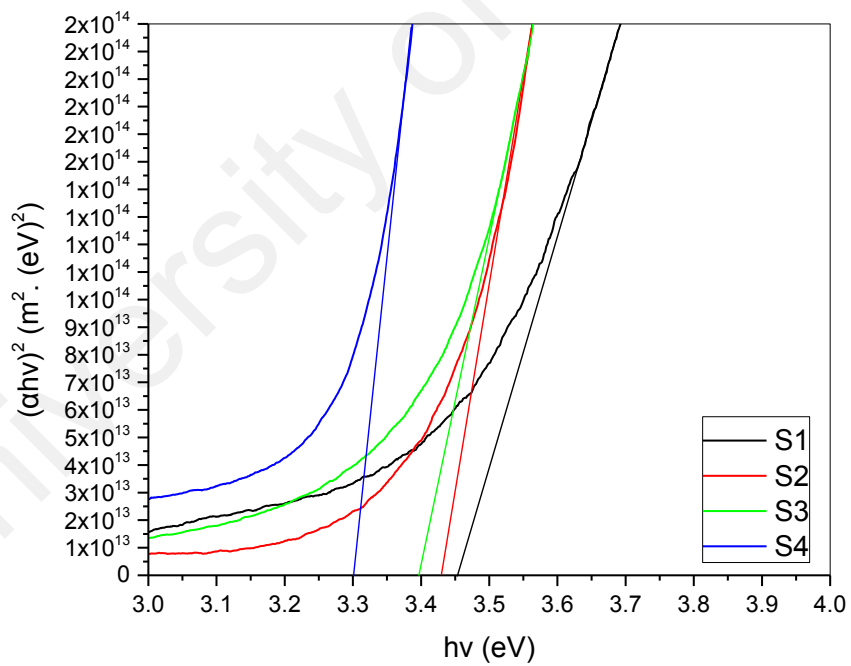
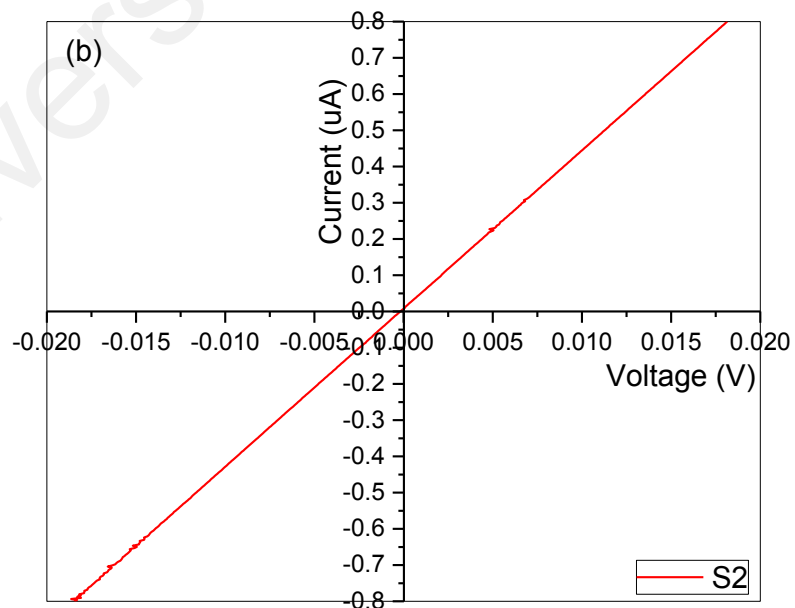
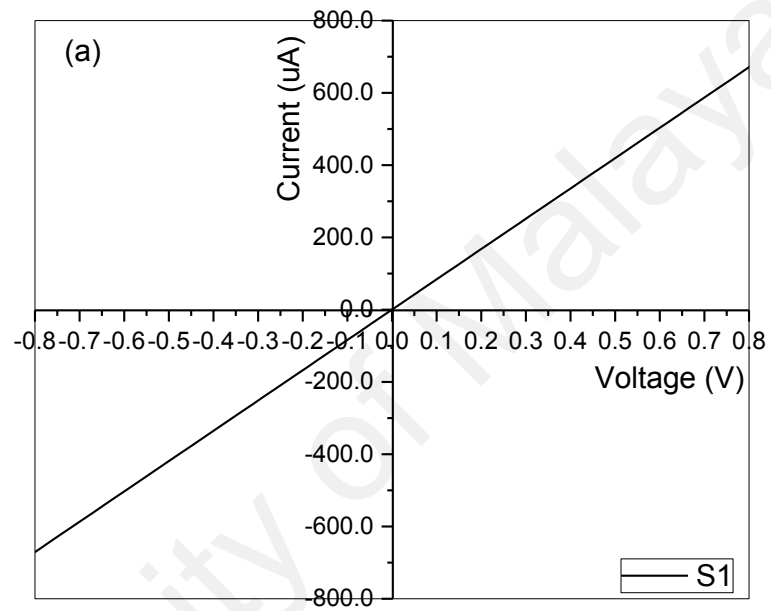


Figure 5.2: Optical absorption coefficients of AZO thin films in function of photon energy for different laser parameters.

**Table 5.1:** Properties of AZO films used in AZO/p-Si.

Sample	Laser wavelength (nm)	Thickness (nm)	Resistivity ( $\Omega \text{ cm}^{-1}$ )	Bandgap (eV)
S1	355	200	0.11	3.45
S2	355	191	1.98	3.42
S3	532	260	0.08	3.4
S4	532	240	1.07	3.3



**Figure 5.3:** I-V results of the AZO thin films deposited in 355 nm laser wavelength for sheet resistance: (a) S1 and (b) S2

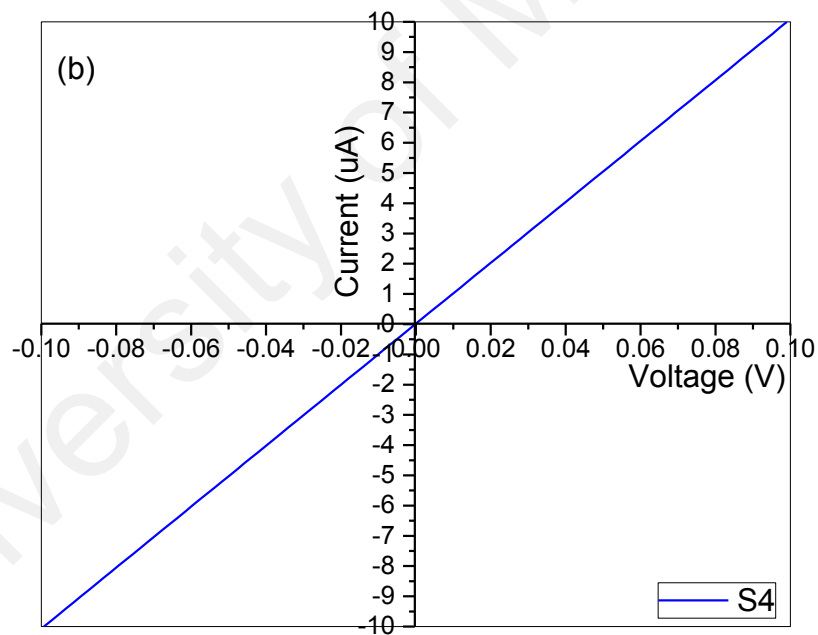
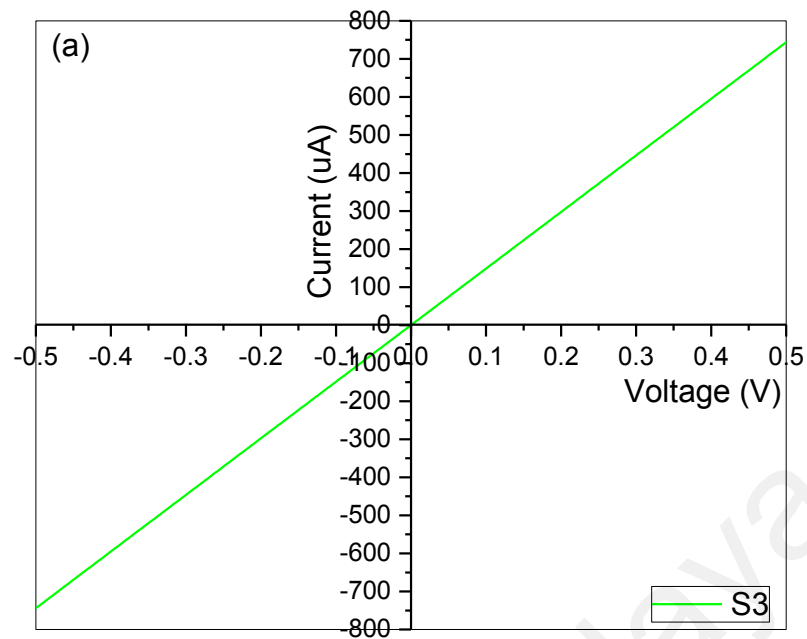


**Figure 5.4:** I-V results of the AZO thin films deposited in 532 nm laser wavelength for sheet resistance: (a) S3 and (b) S4.

In addition, photoluminescence of the samples was measured by using 266 nm laser as the excitation light source. Figure 5.5 shown the PL spectra of samples S1 to S4. Near band edge transition results in PL at  $\sim 380$  nm for the films deposited by both lasers. AZO film deposited by 355 nm laser exhibit a high PL peak in the visible at  $\sim 520$  nm. The PL

peak at 520 nm is related to the defects such as oxygen vacancies ( $V_o$ ) and Zinc interstitials ( $Z_{ni}$ ) (Vempati et al., 2012). According to the Ye et al., 2005 research, the PL visible in the range of 450 nm to 600 nm is due to the defects in ZnO. As a comparison, AZO film deposited by 532 nm has fewer defects that result in PL in the visible range.

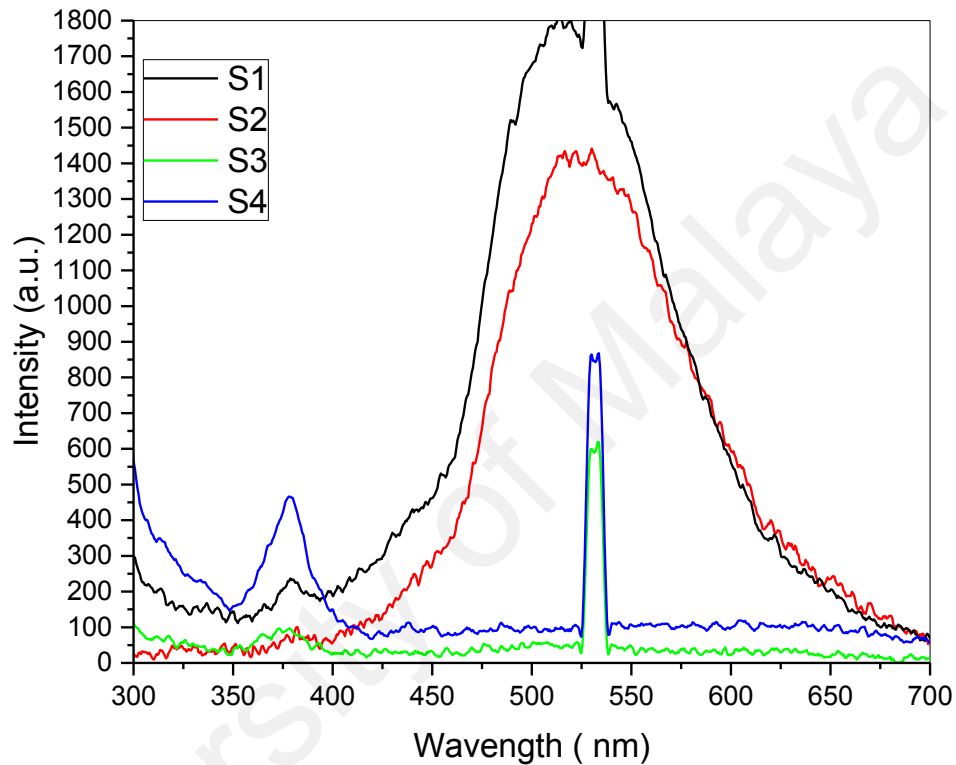


**Figure 5.5:** Photoluminescence spectra of samples.

The structure of the samples for AZO/p-Si heterojunction is shown in Figure 5.6. A layer of gold was coated by vacuum evaporator onto the top of AZO/p-Si and Aluminum contact was placed on p-Si. The gold layer transmits about > 60 % (Figure 5.7) and it act as ohmic contact on the AZO layer (Figure 5.8.). The J-V characteristics of the samples are tested in visible light and UV light and presented in the subsequent sections.

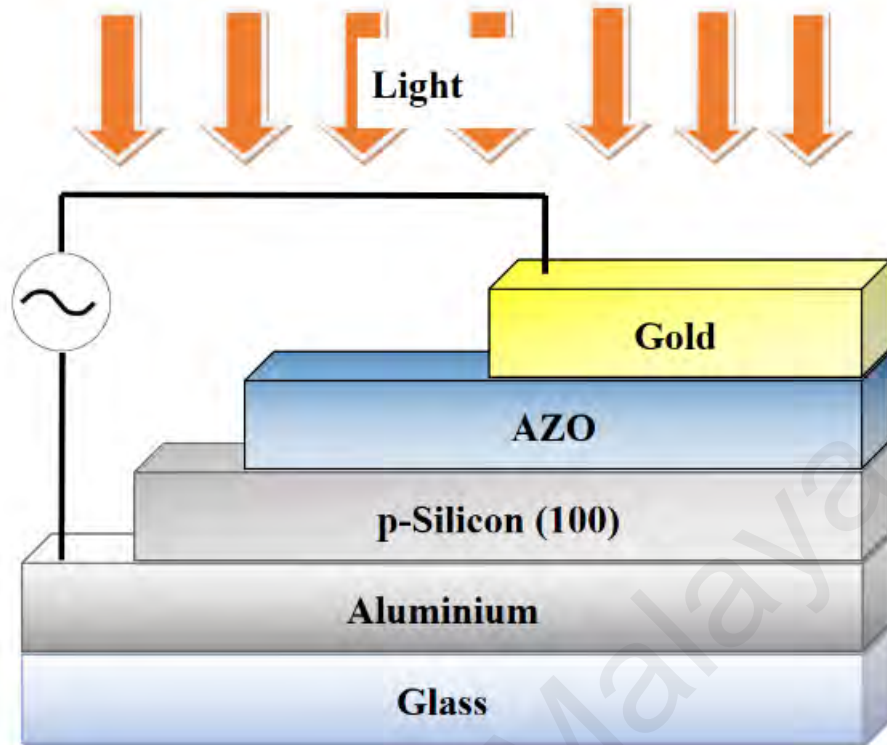


**Figure 5.6:** Schematics diagram of the Ag/AZO/p-Si/Al structure.

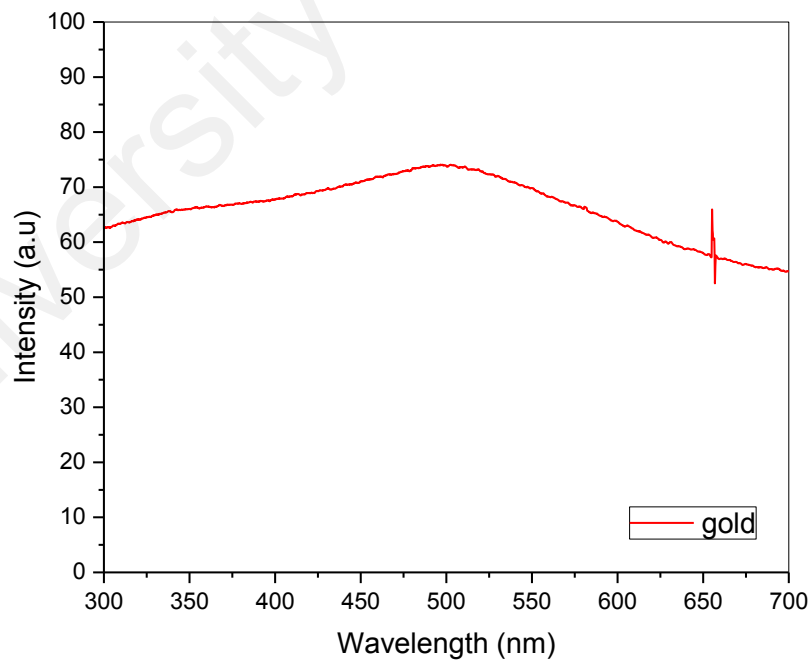


**Figure 5.7:** Transmittance of Au films.

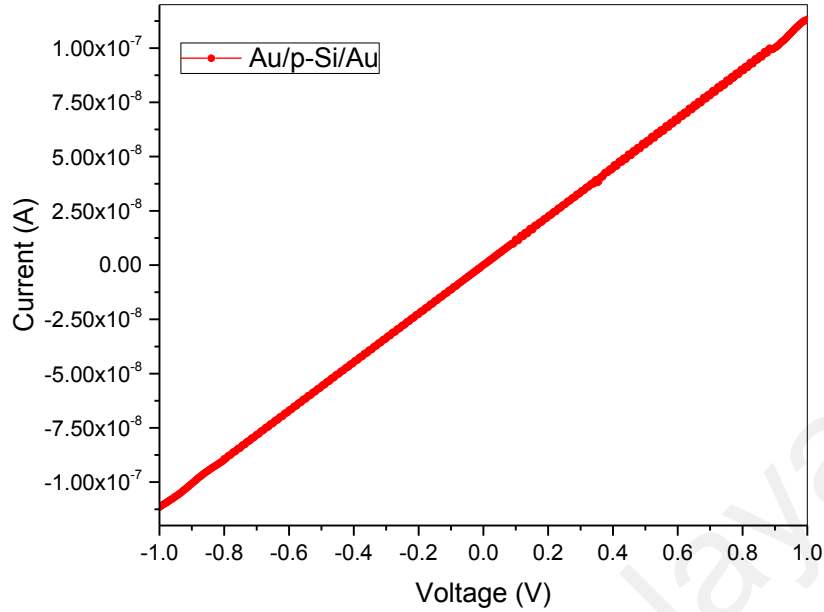


**Figure 5.8:** I-V characteristic of Au/AZO/Au structure.

### 5.3 The effect of visible light illumination on AZO/p-Si heterojunction

The effect of visible illumination on the J-V characteristic of Au/p-Si/Al heterojunction is shown in Figure 5.9. As the intensity of light increases, photocurrent is generated in zero bias and forward bias because of electron-hole pair generation at p-Si side.

The effects of visible illumination on the J-V characteristic of Au/AZO/p-Si/Al heterojunction are shown in Figure 5.10 to Figure 5.13 where the AZO films are deposited by different laser parameters. All of the samples exhibited rectification and generated photocurrent when illuminated. It is noted that the photoresponse occurred in both forward and reverse biased. In forward biased, the response of the samples is higher as compared to the reference samples Au/p-Si/Al. Above a threshold light intensity, the light-induced current saturated due to the limited carrier in AZO thin films and p-Si. The limited penetration of the visible light was also another factor to cause the saturation of the photocurrent. The performance of the samples is summarized in Table 5.2.

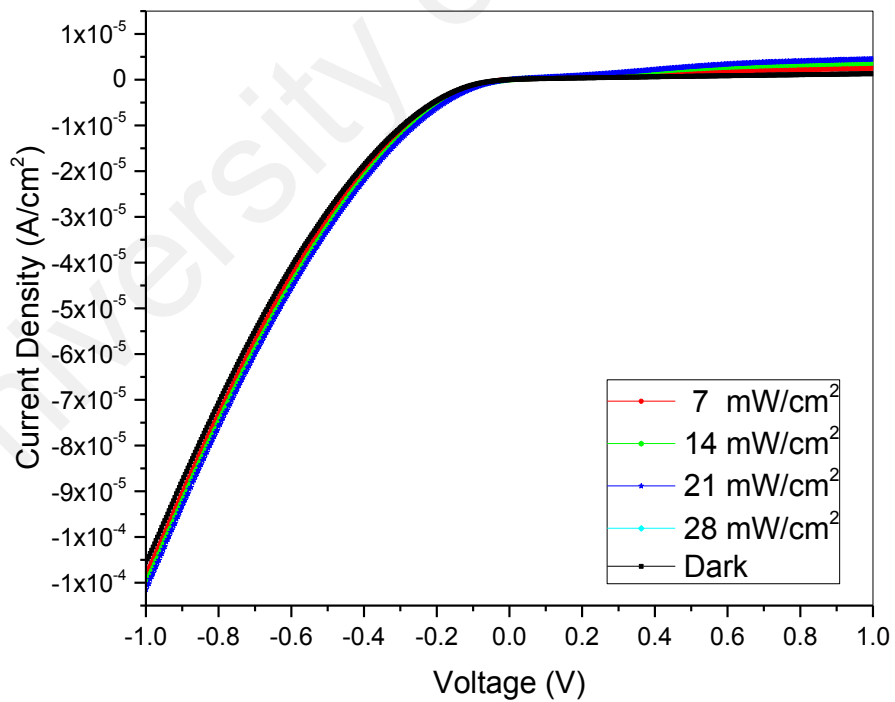
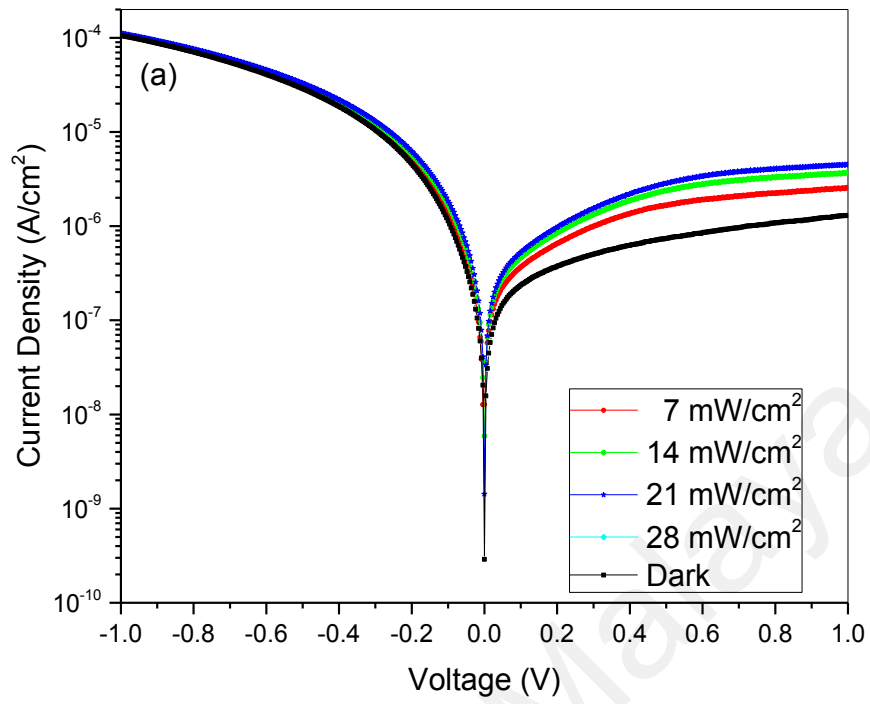


**Figure 5.9:** J-V characteristic of the Au/p-Si/Al heterojunction with different visible light intensity: (a) semi-log plot and (b) linear plot.

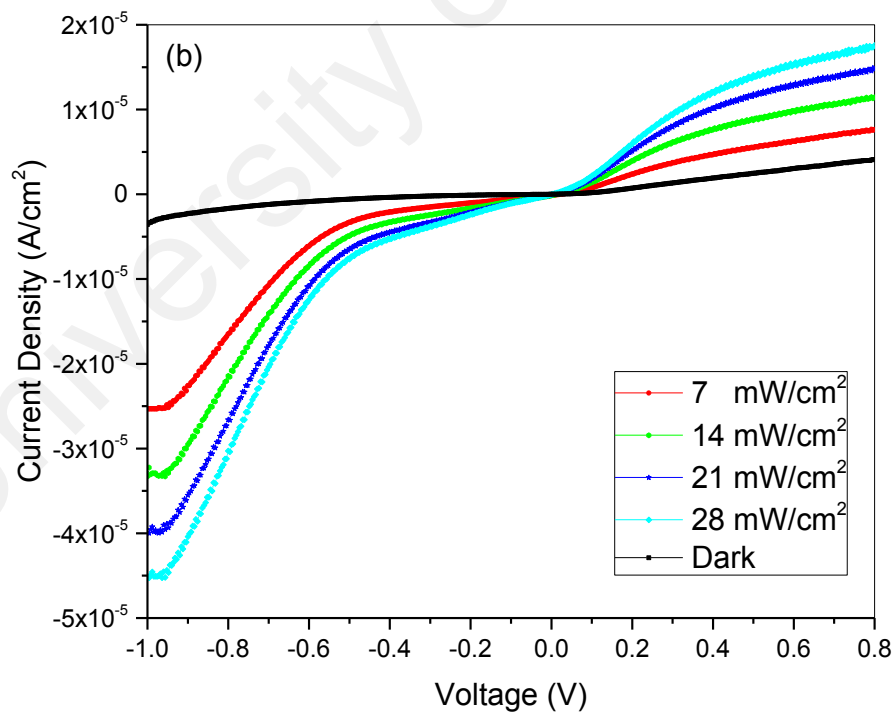
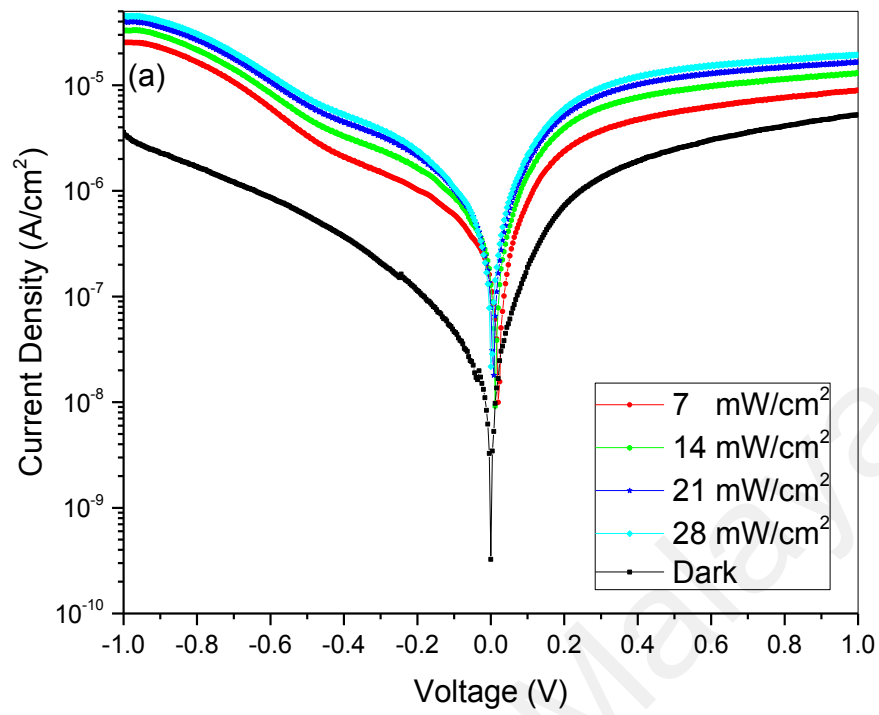


**Figure 5.10:** J-V characteristic of S1 with different visible light intensity: (a) semi-log plot and (b) linear plot.

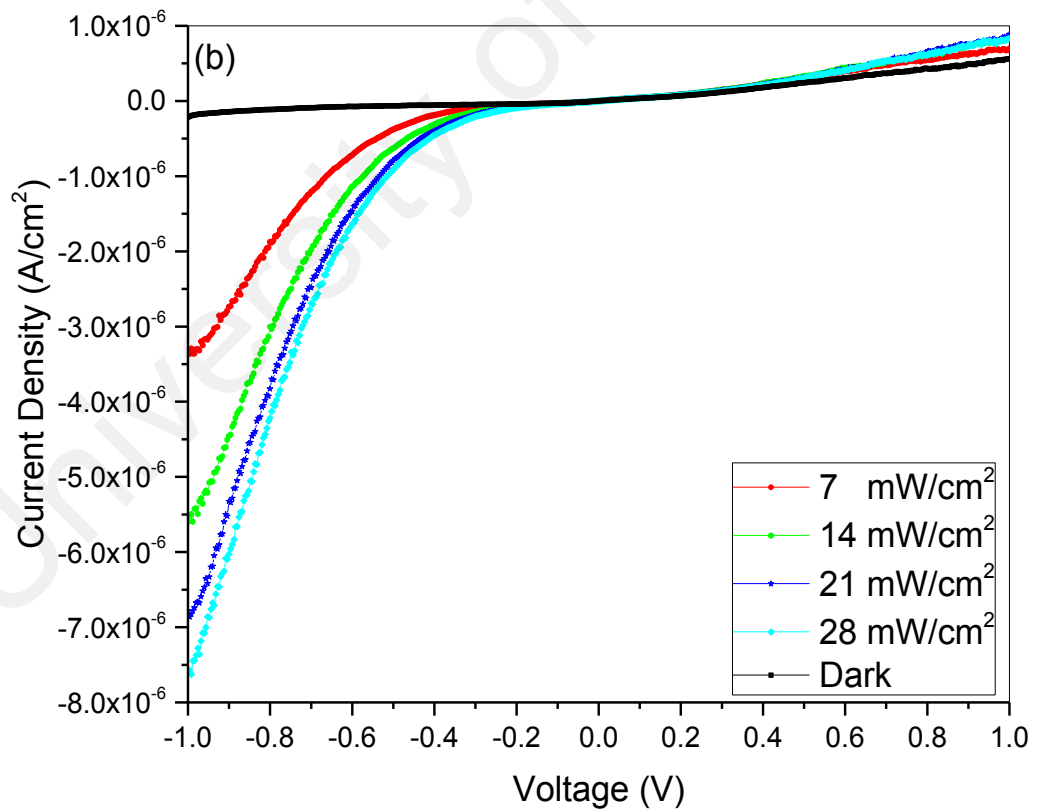
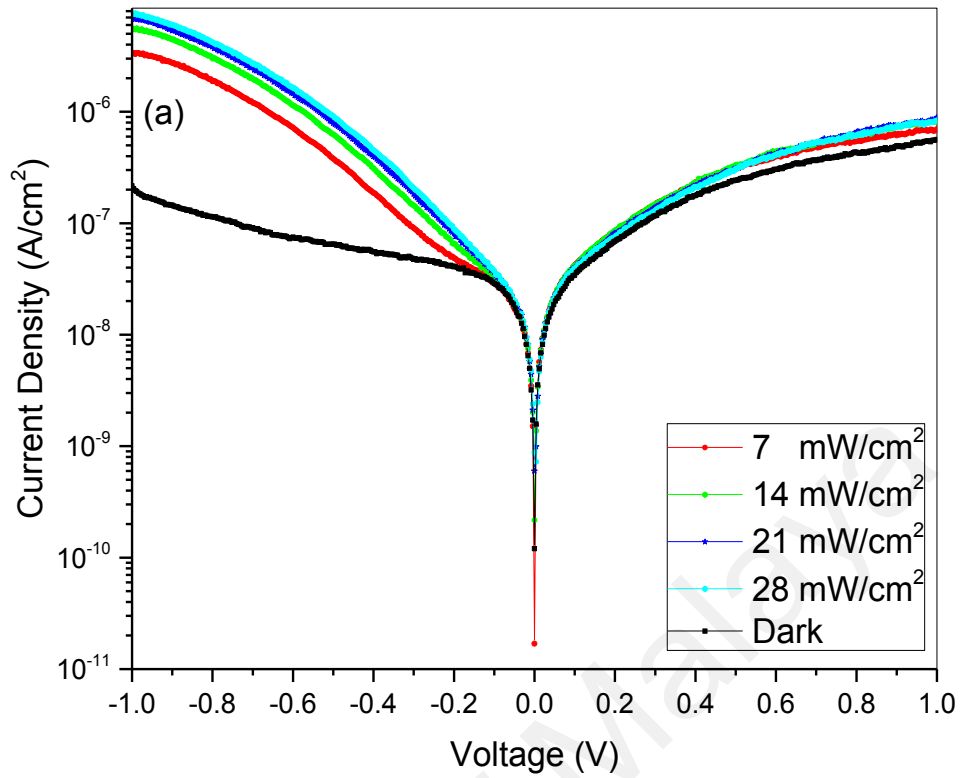


**Figure 5.11:** J-V characteristic of the S2 with different visible light intensity: (a) semi-log plot and (b) linear plot.

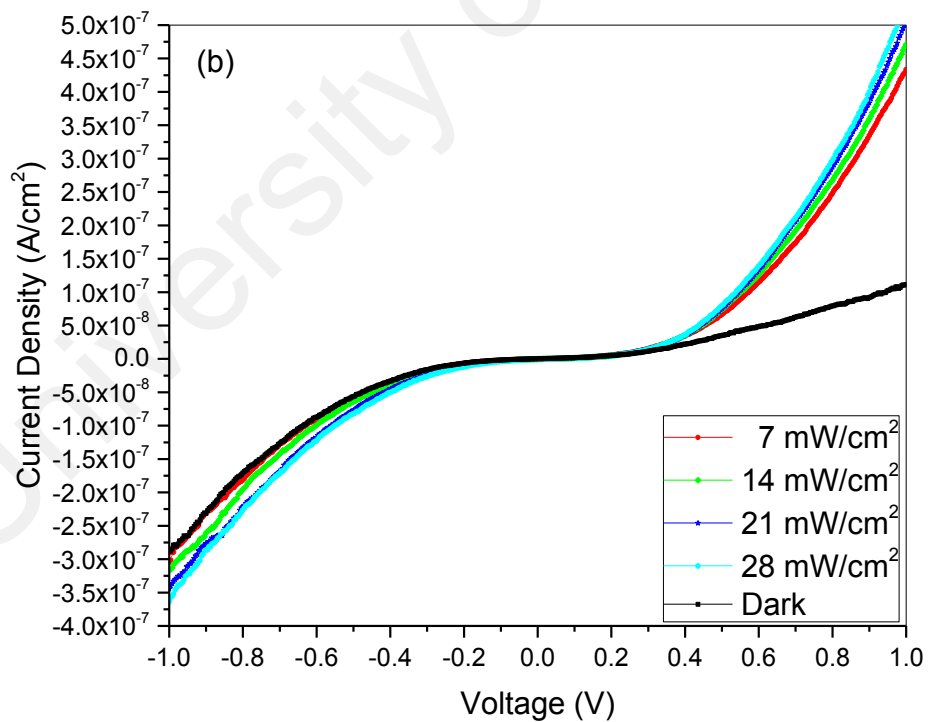
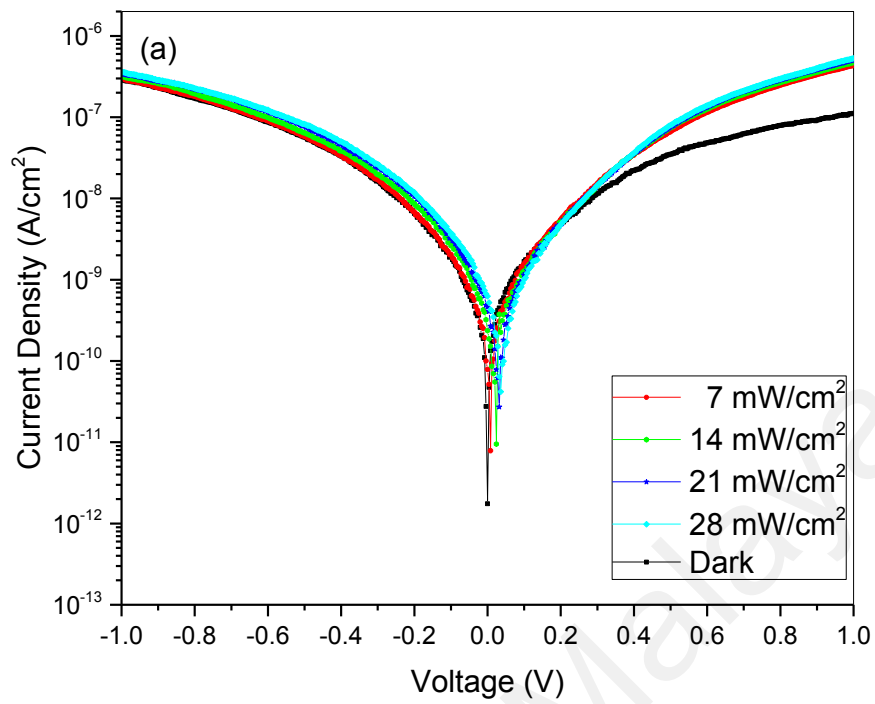


**Figure 5.12:** J-V characteristic of the S3 with different visible light intensity: (a) semi-log plot and (b) linear plot.

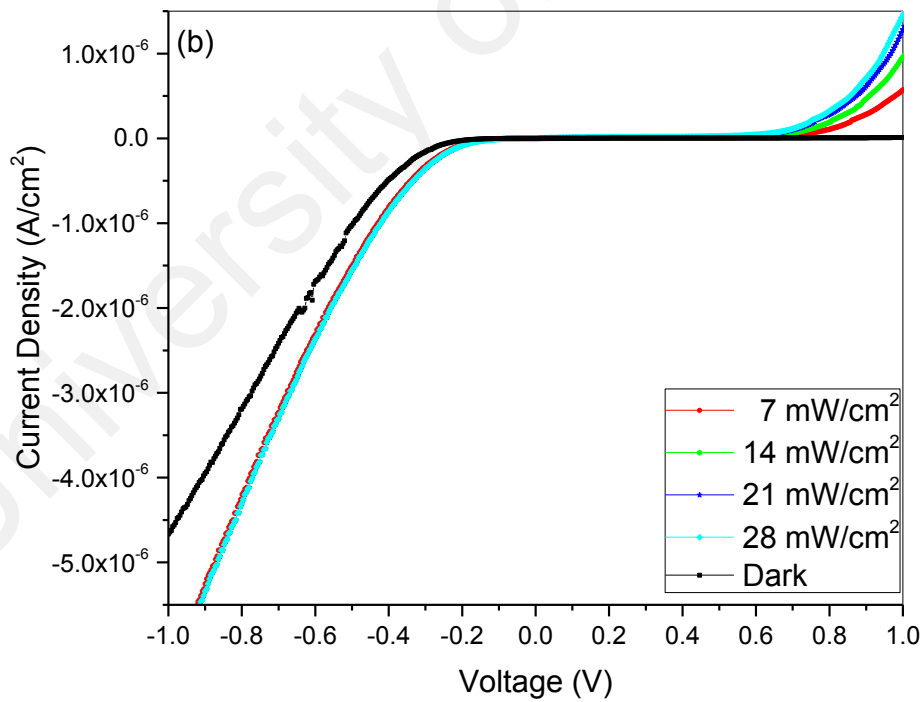
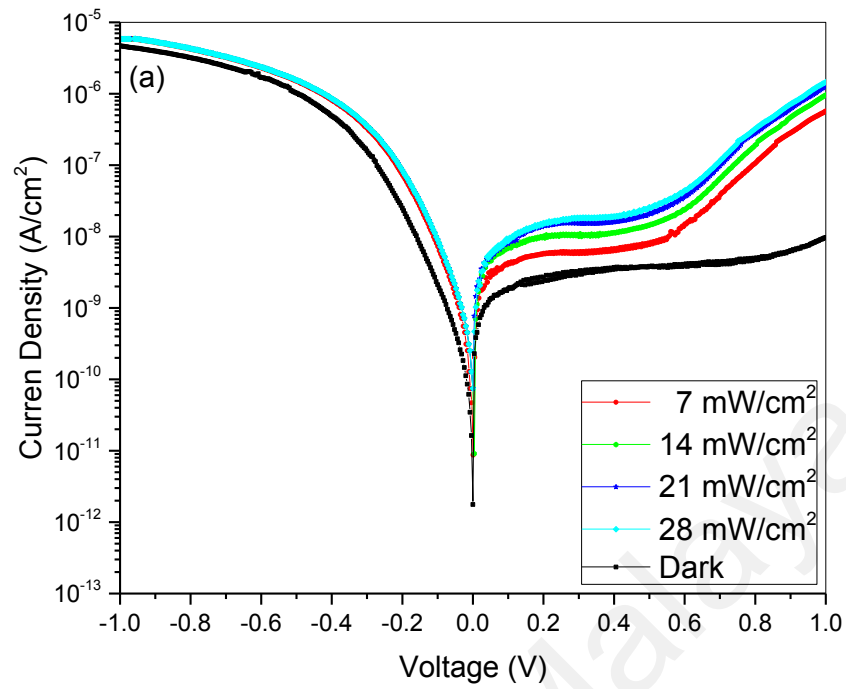


**Figure 5.13:** J-V characteristic of the S4 with different visible light intensity: (a) semi-log plot and (b) linear plot.

**Table 5.2:** Ratio of Photocurrent with the Dark current ( $I_{ph}/I_d$ ).

Samples	Light Insensitive (W/cm <sup>2</sup> )	Photoresponse ( $I_{ph}/I_d$ )	
		Forward Bias (1 V)	Reverse Bias (-1 V)
S1	7	1.7	7.1
	14	2.5	9.3
	21	3.2	11.2
	28	3.7	12.7
S2	7	1.2	18
	14	1.5	30
	21	1.6	36
	28	1.5	40
S3	7	3.9	1.0
	14	4.2	1.1
	21	4.5	1.2
	28	4.8	1.2
S4	7	58.0	1.3
	14	93.3	1.3
	21	132.0	1.3
	28	150.0	1.3
p-Si (100)	7	2.0	1.0
	14	2.8	1.0
	21	3.5	1.1
	28	4.0	1.1

The photoresponse are highly dependent on the quality of the AZO thin films such as morphology, stoichiometry and crystalline of the thin films (Kim et al., 2001).

Under forwards bias, S3 and S4 (532 nm) produce higher photocurrent as compared to S1 and S2 (355 nm) as shown in Figure 5.14(b). This phenomenon indicated that the AZO thin films deposited by 532 nm laser act a photo window to allow the visible light photo into the depletion region of the AZO/p-Si junction particularly at the p-Si side. The PL result shown that the AZO thin films deposited by 532 nm laser possess only a small green peak often related to the defects in ZnO. Thus AZO is insensitive to visible light. Therefore, visible photons transmitted through the AZO layer but are absorbed in the

depletion region of the p-Si to generate electron-hole pair, resulting the photoresponse behaviour of the AZO thin films (532 nm) in Au/AZO/p-Si/Al structure to be almost same as the sample without AZO layer (Au/p-Si/Al) under the illumination of the visible light.

Under reverse bias, the heterojunction with AZO thin films deposited by 355 nm laser wavelength (S1 and S2) are higher photoresponse than the samples deposited in 532 nm (S3 and S4). Compare the AZO thin films deposited in 355 nm (S1 and S2) to the 532 nm (S3 and S4), the photoresponse mechanism of 355 nm samples in heterojunction structure are totally different from the 532 nm. The PL of 532 nm samples consist mainly of a single peak at 382 nm. However, the AZO thin films deposited by 355 nm laser wavelength produced PL in UV and also visible (green) and the PL at the visible wavelength was higher intensity than the 382 nm peak. This indicated that there was ZnO defect energy level in the AZO thin films (355 nm). Therefore, the photogenerated electron hole pair are highly possible for the samples deposited by 355 nm, rather than only act as a transmittance window. In order to explain the mechanism of the photogenerated electron in the Au/AZO (355 nm)/p-Si heterojunction, a band diagram is constructed. Figure 5.15 shown the energy band diagram of Au/AZO (355 nm)/p-Si heterojunction derived from the Anderson model. In this case, electrons transfer from AZO to Au. As shown in Figure 5.15, there were three possible paths of the photoexcited electrons contributed the photocurrent in reserve bias. Firstly, similar to 532 nm, the electron hole pair may be generated in the depletion region of p-Si, the photogenerated hole would attracted by the negative charge of the outer circuit and drift to the p-Si side whereas the electron would be swept to the AZO side by electric field. The second possible path is that the photogenerated electrons could be trapped by lower defect level of the AZO and then jumped to the higher defect level by absorbing visible photons. After that, the electrons would travel from higher defect level to the conduction band of AZO

and to the Au side. The third path is the photogenerated electron in depletion region near the AZO and Au interface were excited to a higher defect level directly by absorption of photons with high energy. After that, the photoexcited electron would travel to the conduction band of AZO.

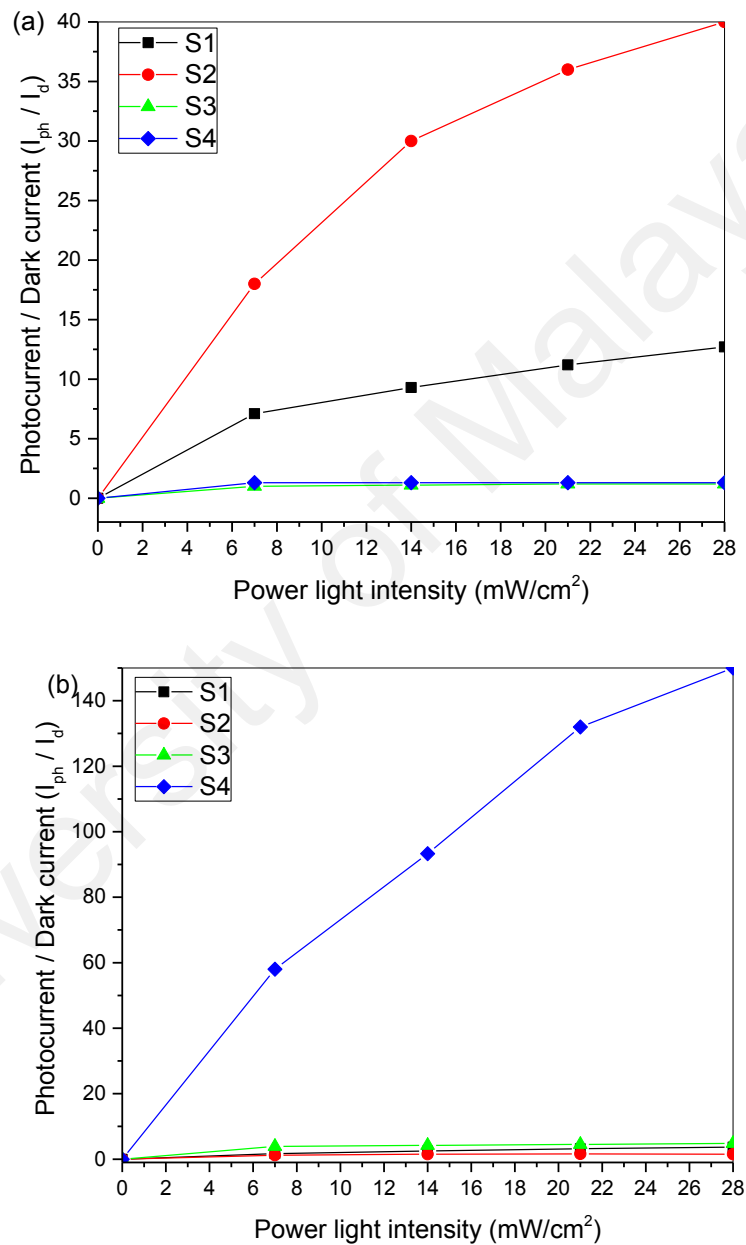


**Figure 5.14:** The ratio of Photocurrent and Dark current ( $I_{ph}/I_d$ ) of the AZO/p-Si heterojunction with different laser parameter in (a) reverse bias and (b) forward bias.

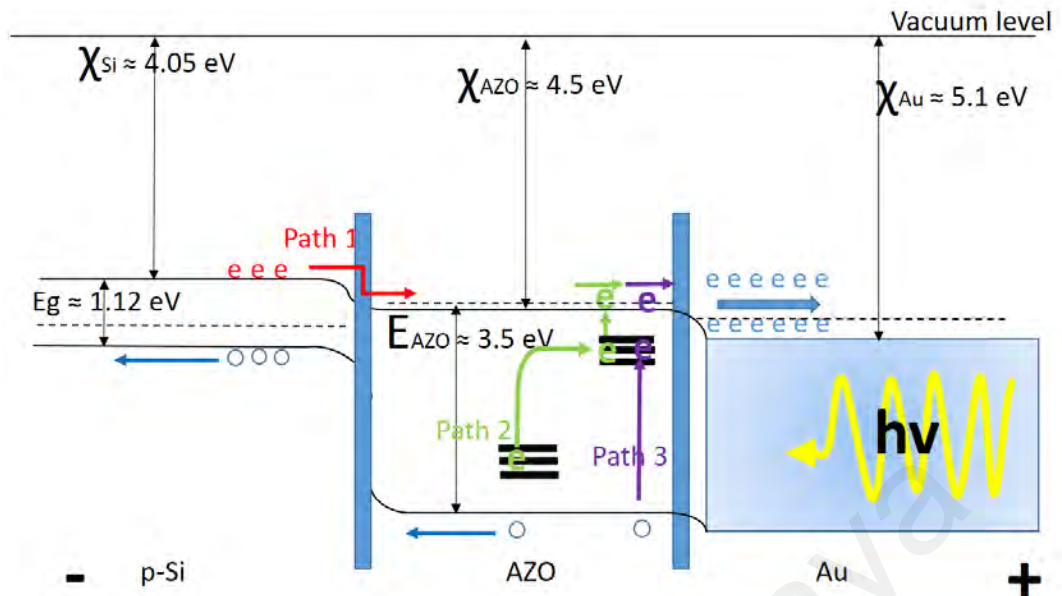


**Figure 5.15:** The band diagram of Au/AZO/p-Si heterojunction in reverse bias.

#### 5.4 The effect of UV light illumination on AZO/p-Si heterojunction

UV light centered at 365 nm was used to illuminate the AZO/p-Si heterojunction (Figure 5.16). The power density of the UV light was 1.9 mW/cm<sup>2</sup> in this experiment.

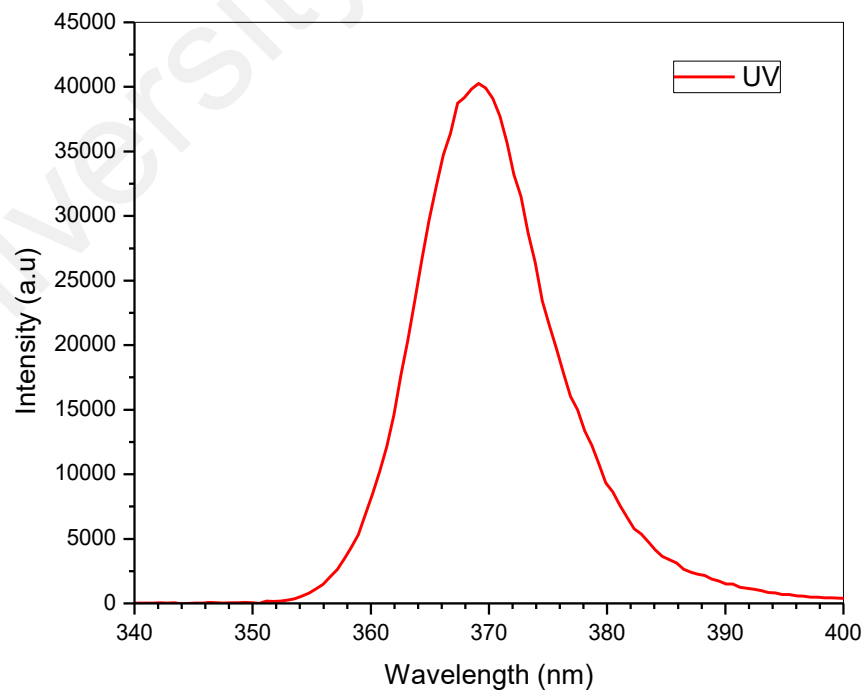


**Figure 5.16:** Spectrum of UV light.

Figure 5.17 shows the J-V characteristic of Au/p-Si/Al heterojunction in the dark and in UV illumination. No photoresponse was detected under UV illumination. The J-V characteristic of samples S1 to S4 (Au/AZO/p-Si/Al) with AZO thin film are shown in Figure 5.18 to 5.21.

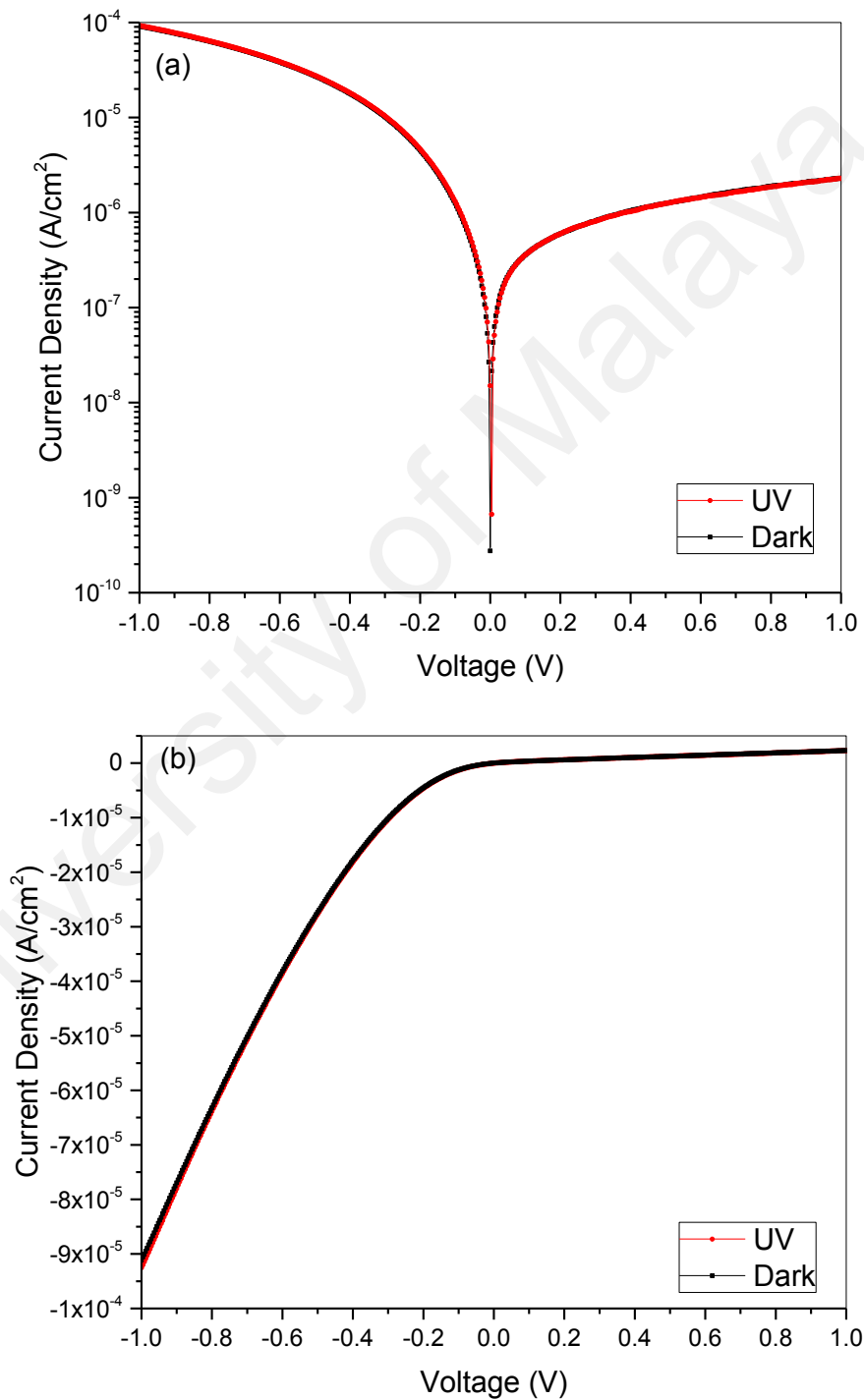


**Figure 5.17:** J-V characteristic of the Au/p-Si/Al heterojunction in dark and UV illumination: (a) semi-log plot and (b) linear plot.

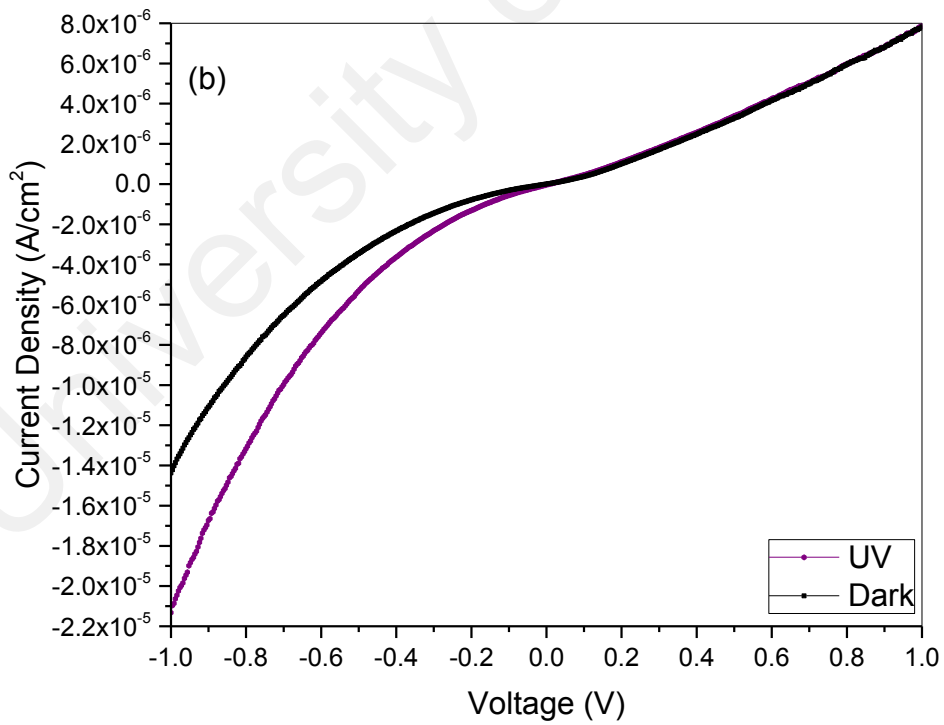
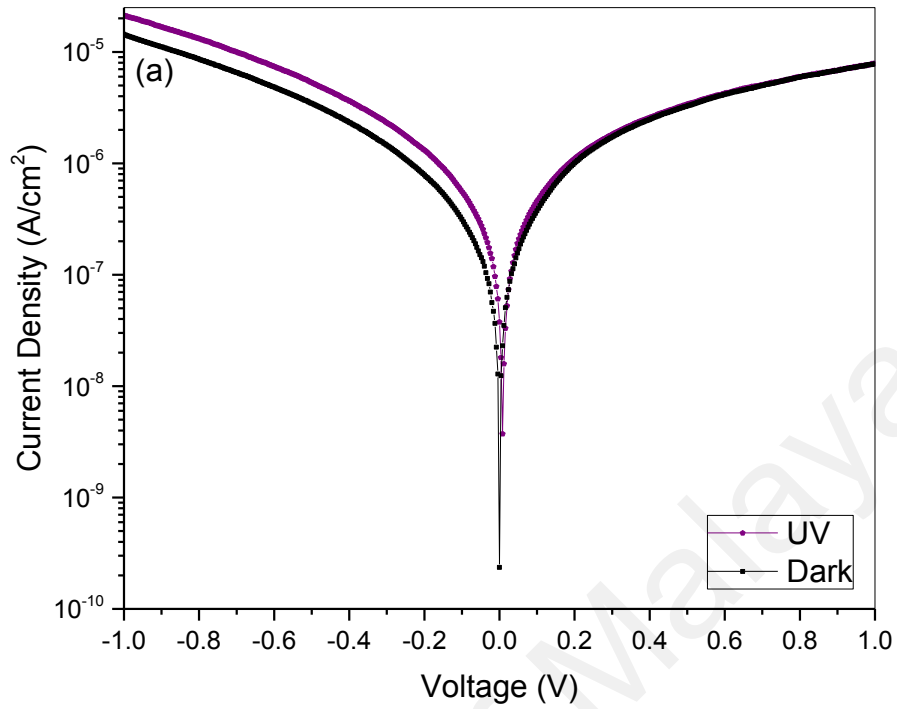


**Figure 5.18:** J-V characteristic of the S1 with UV illumination: (a) semi-log plot and (b) linear plot.

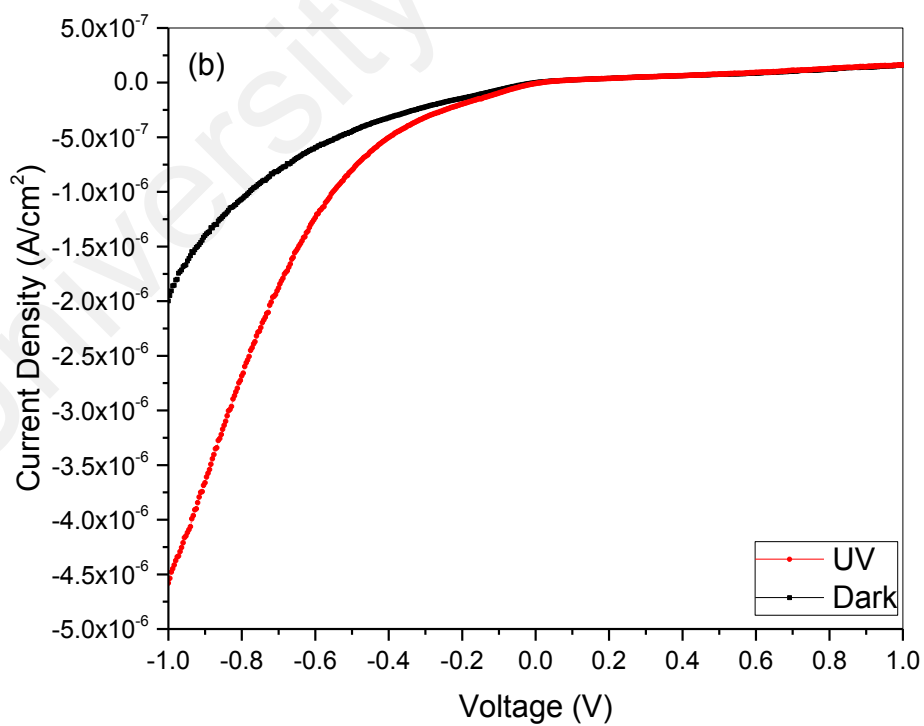
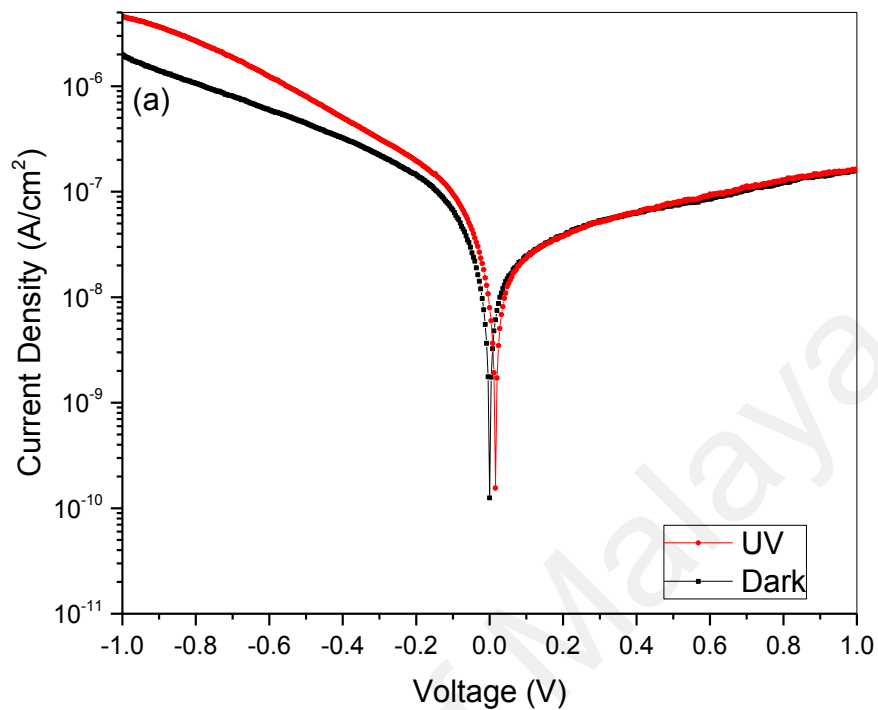


**Figure 5.19:** J-V characteristic of the S2 with UV illumination: (a) semi-log plot and (b) linear plot.

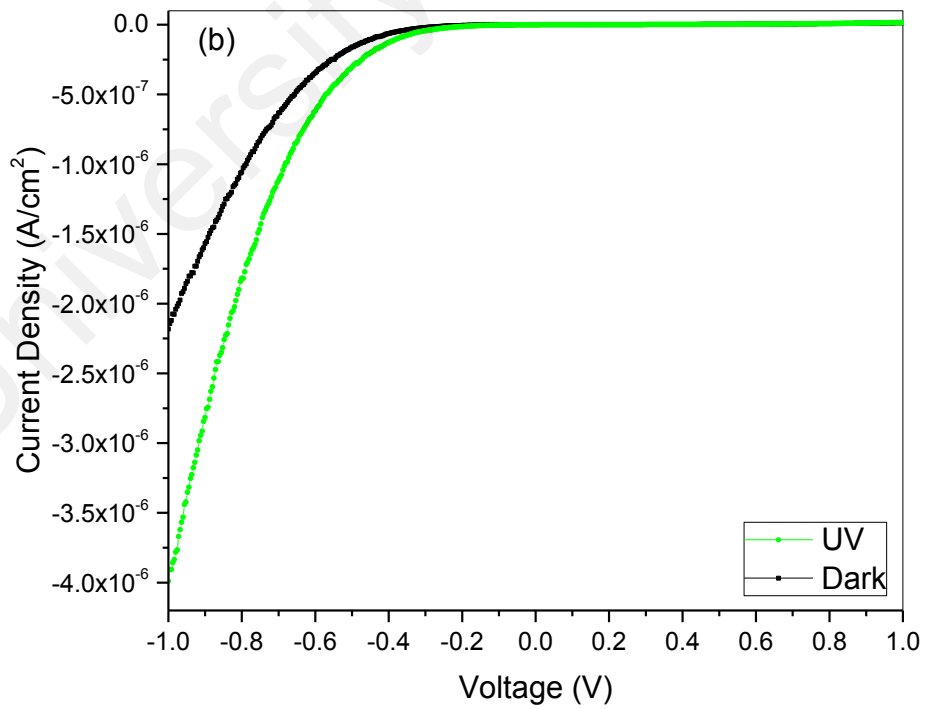
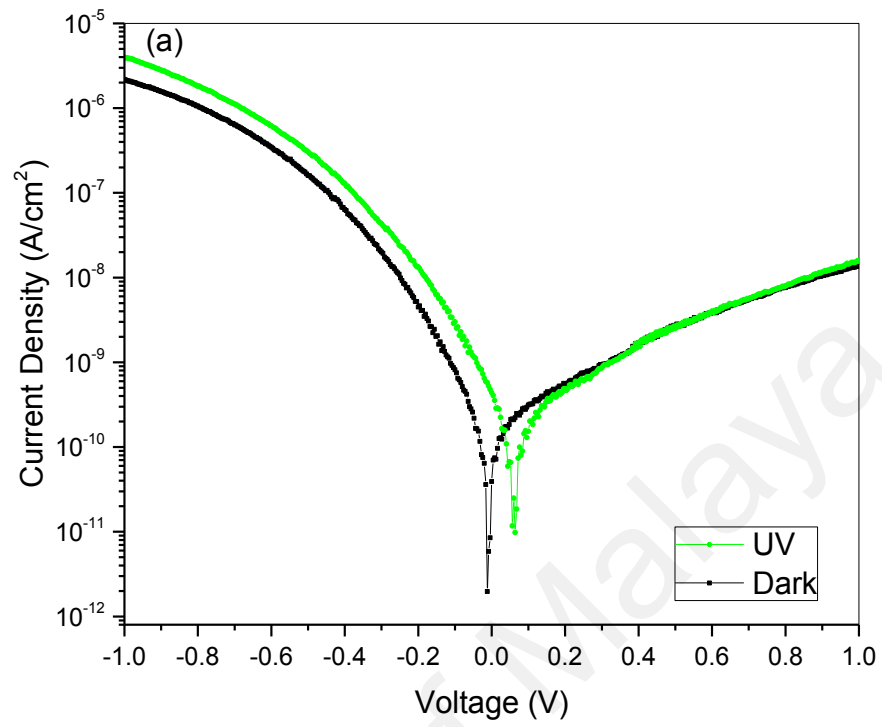


**Figure 5.20:** J-V characteristic of the S3 with UV illumination: (a) semi-log plot and (b) linear plot.

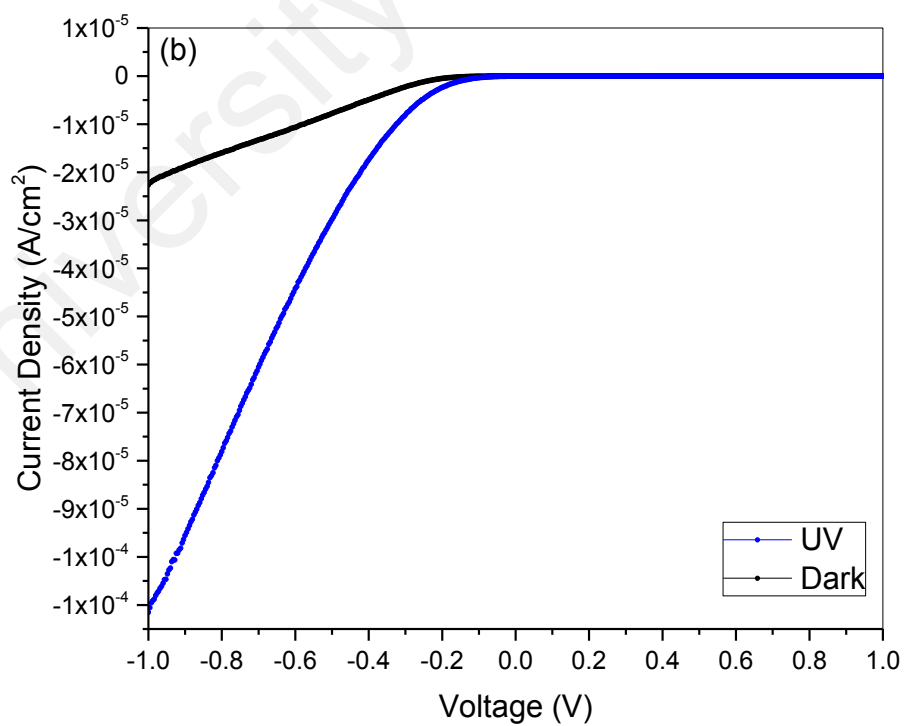
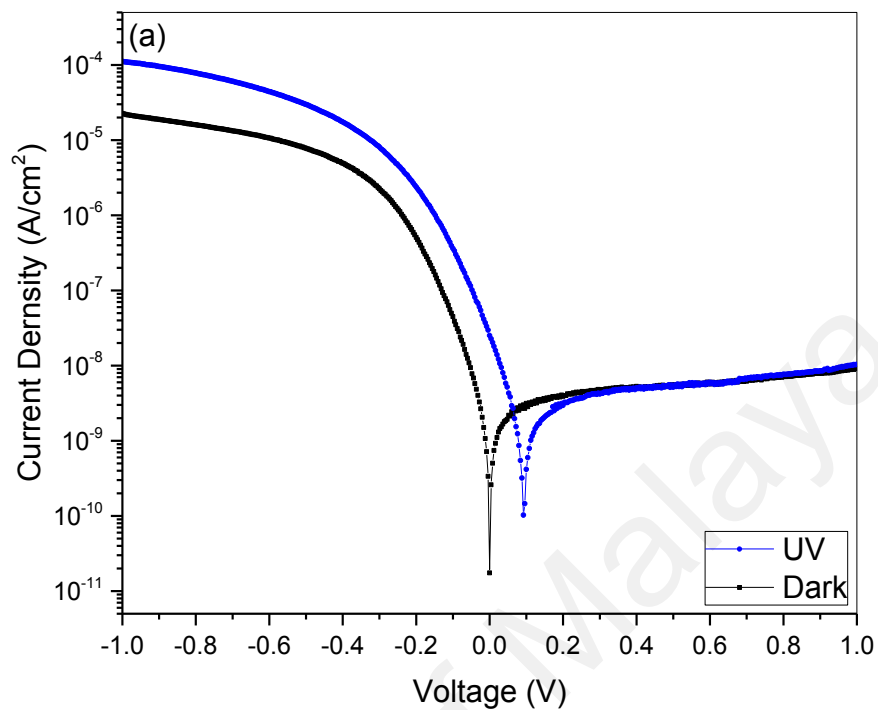


**Figure 5.21:** J-V characteristic of the S4 with UV illumination: (a) semi-log plot and (b) linear plot.

As shown from Figure 5.18 to 5.21, all of samples with AZO thin films responded to the UV light. The response to UV illumination only occurred when the junction is reverse-bias. The results indicated that the UV light was mainly absorbed in the AZO depletion side. The results of  $I_{ph}/I_d$  for all the samples are summarized in Table 5.3.

**Table 5.3:** Ratio of photocurrent  $I_{ph}$  / Dark current  $I_d$  (under UV illumination).

Sample	Photocurrent $I_{ph}$ / Dark current $I_d$	
	Reverse Bias (-1V)	Forward Bias (-1V)
S1	1.4	1.0
S2	2.3	1.0
S3	1.8	1.2
S4	4.9	1.1
p-Si	1.0	1.0

According to Gao et al., 2017, AZO responses to UV light due to the wide bandgap of AZO thin films. The AZO thin films in this work exhibited a bandgap of 3.3 to 3.45 eV and PL  $\sim$  383 nm in room temperature. Thus electrons-hole pair can be generated with the UV light illumination. The results are in agreement with the reports of Mridha & Basak, 2007; Boet al., 2009 and Huang et al., 2009. The photogenerated carriers in forward bias are mainly dominated the carriers at the depletion region of p-Si side whereas the photogenerated carriers in reserve bias are mainly dominated those at the depletion region of AZO. Therefore, UV photon will be absorbed in the AZO layer and generated electrons-hole pairs; electron would be drifted towards the positive electrode through AZO depletion region. Consequently, the current increase as the reverse bias is increased. The photocurrent in forward bias was dominated by p-Si side depletion region and thus UV photon was not absorbed by p-Si.

## 5.5 Effect of Resistivity

In this section, the characteristic of sample S1 and S2 deposited by using 355 nm laser, with different resistivity ( $S1 = 0.11 \Omega\text{cm}^{-1}$  and  $S2 = 1.98 \Omega\text{cm}^{-1}$ ) are compared. Both of the samples were deposited by using 355 nm laser. As shown in Table 5.1, the resistivity of S2 was 20 times higher than S1. The high resistivity was highly dependent on the carrier concentration and mobility of the thin film which has been discussed in Chapter 4.3.5.

Figure 5.22 shows the J-V characteristics of AZO/p-Si heterojunction with higher resistivity of AZO thin films (S2) and lower resistivity AZO thin films (S1) in linear plot (a) and semi-log plot (b). Both samples showed the rectifying behaviour. However, the sample with the low resistivity AZO thin films (S1) produced more current than the high resistivity AZO (S2) in both reverse and forward bias and the current leakage of S1 is higher than S2 in zero bias as shown in Figure 5.22(b).

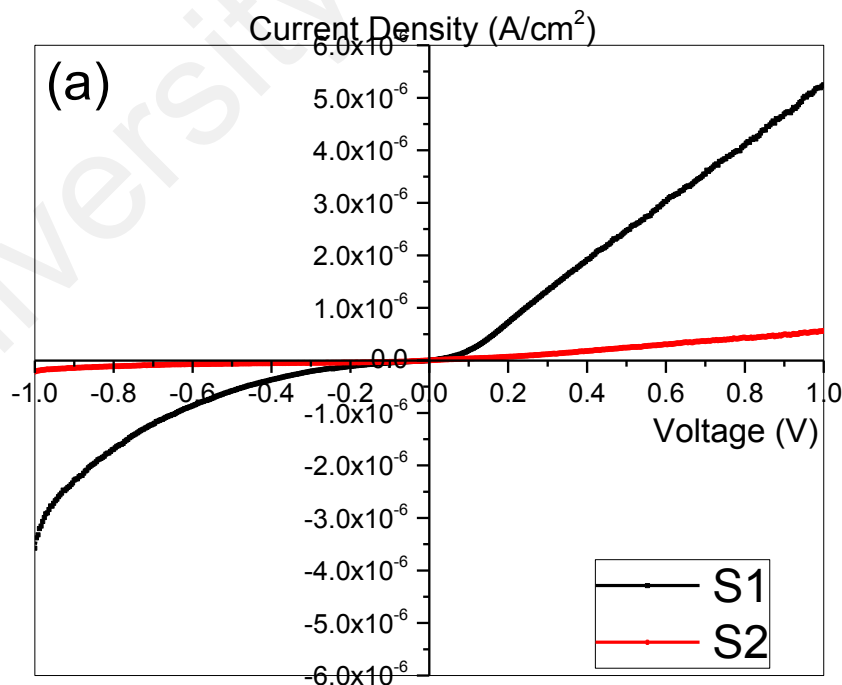


**Figure 5.22:** J-V characteristic of AZO/p-Si heterojunction in dark: (a) linear plot and (b) semi-plot.

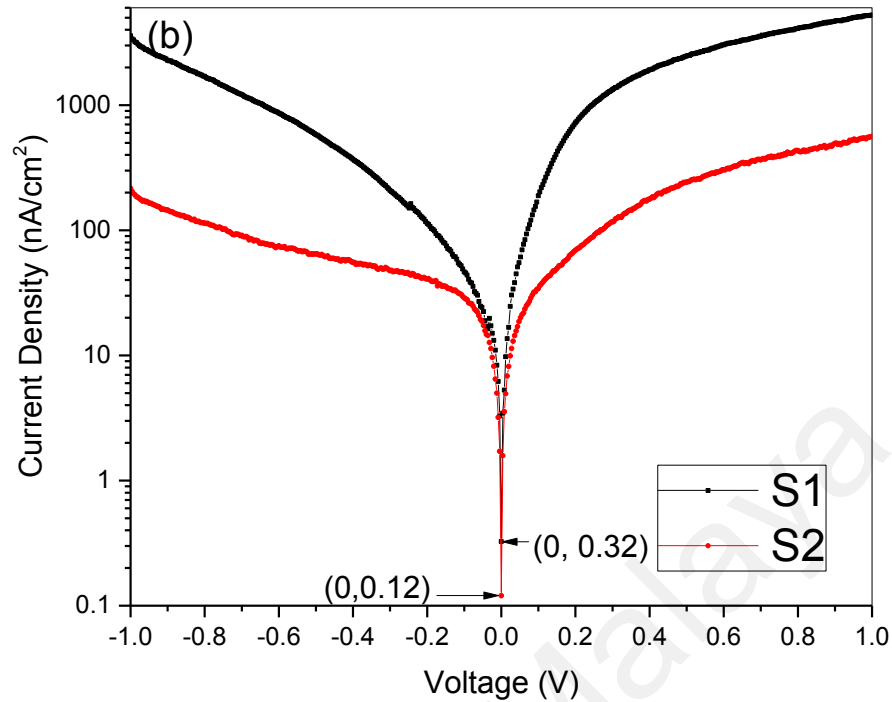


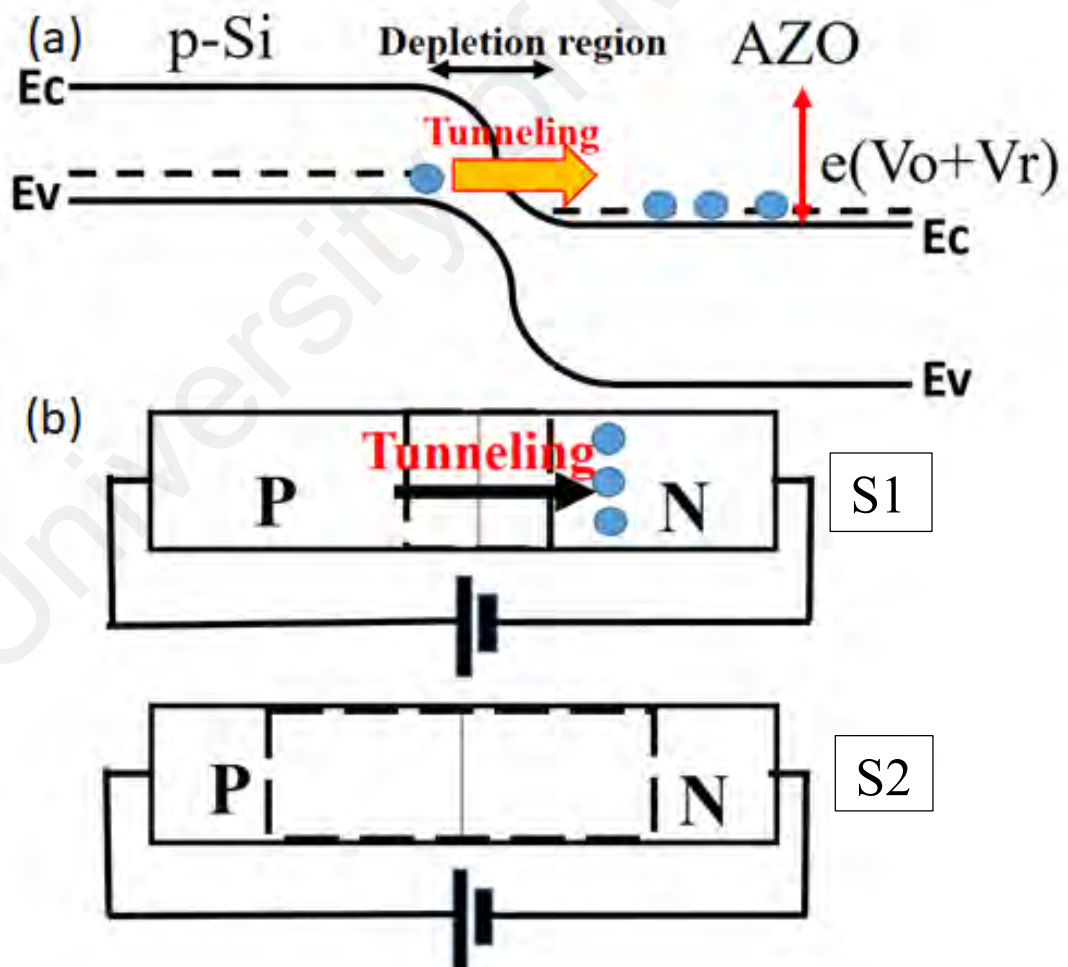
**Figure 5.22, continued.**

The J-V characteristics of S1 and S2 in forward bias without illuminated are compared. Both samples increased the current in the forward bias but the turn on voltage of the S1 is lower than the S2 as shown in Figure 5.22. The lower turn-on voltage of S1 suggested that it has higher carrier concentration and higher mobility when compared to S2. Forward current was dominated by the majority carriers; therefore, due to the higher carrier concentration and higher carrier mobility in S1, the turn on voltage of the S1 is lower than S2. In addition, according to the Burstein-Moss effect (BM), increasing the carrier concentration would shift the Fermi level toward or in the conduction band, resulting in the easy flow of the electron from AZO side to p-Si (Ajimsha et al., 2008).

When S1 and S2 are reverse bias without illumination, the saturation current or leakage current of the S1 is higher than the S2. The breakdown voltage of S1 is lower as compared to the S2. This may be due to the fact that the depletion region of AZO/p-Si (S1) junction is narrower compared to the S2. The lower breakdown voltage and higher reverse current

in S1 can be explained based on the tunnelling mechanism and it is shown in Figure 5.23. As shown in Figure 5.23, tunnelling mechanism occurred in the narrow depletion region with reverse bias, electrons (minority carriers) switched faster with high kinetic energy and tunnel through the depletion region from the valence band of p-Si to the conduction band on the AZO side when the reverse voltage applied. The tunnelling process led to a larger increase of current in reverse bias.

Compare the S1 and S2 in zero bias, the current produced of S1 is higher than S2 which are  $0.32 \text{ nA/cm}^2$  (S1) and  $0.12 \text{ nA/cm}^2$  (S2), as shown in Figure 5.22(b). This is due to the smaller depletion in S1. However, their current density in zero bias are not much different.



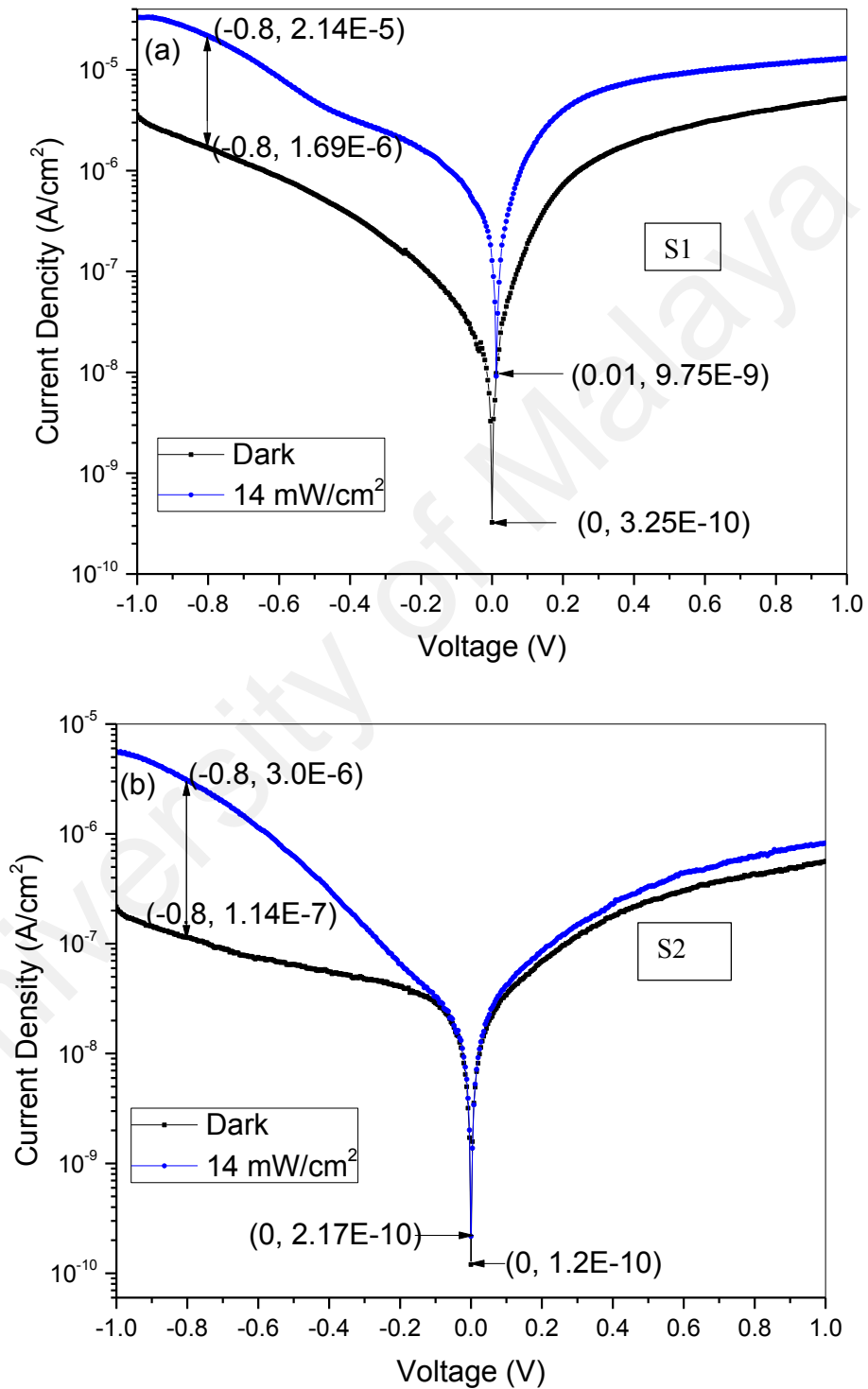
**Figure 5.23:** (a) pn junction bandgap of AZO/p-si in reverse bias and (b) pn junction of S1 and S2 in reverse bias.

Figure 5.24 shows the photoresponse of AZO/p-Si heterojunction (S1 and S2) under illumination of  $14 \text{ mW/cm}^2$ . At forward bias, both samples response to the visible light. The photo-generated forward current was slightly higher than the current in dark. In forward bias, the photogenerated electron-hole pairs were generated in the p-Si side as discussed in Chapter 5.2. However, the photocurrent generated is slightly higher in S1 because majority carriers of AZO in S1 were easier to tunnel from the AZO side to the p-Si side and compound with the photogenerated electrons. As the voltage keep going to increase, the depletion region will decrease and finally disappear. As shown in the Figure 5.25(b) and 5.26(b), the J-V curve shows the straight line (ohmic) in higher voltage or after the turn-on voltage. Due to the smaller depletion region in S1, the turn on voltage of S1 is smaller than S2.

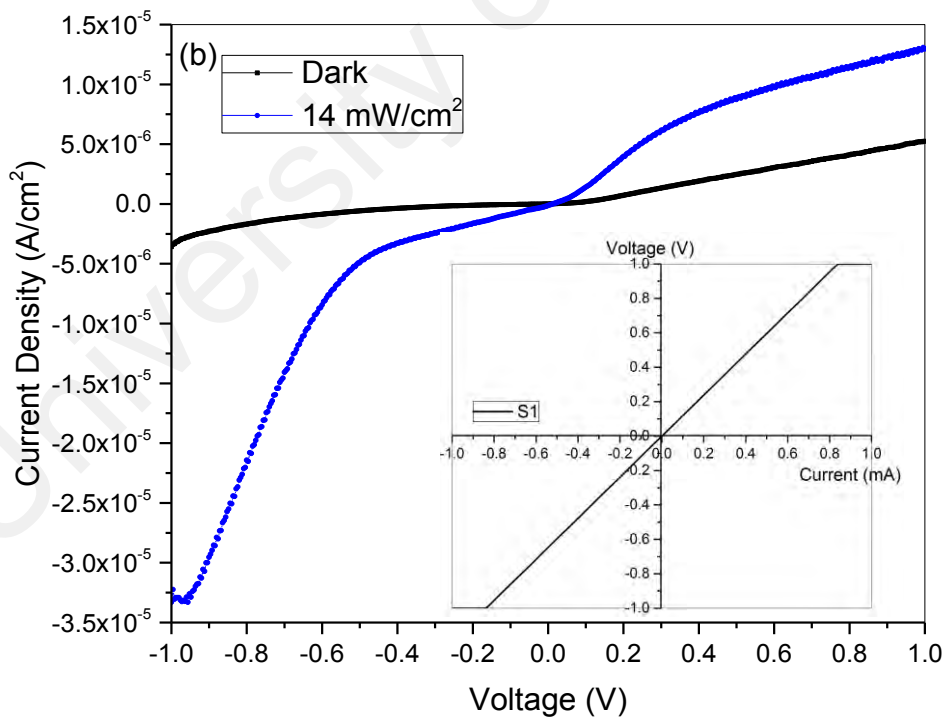
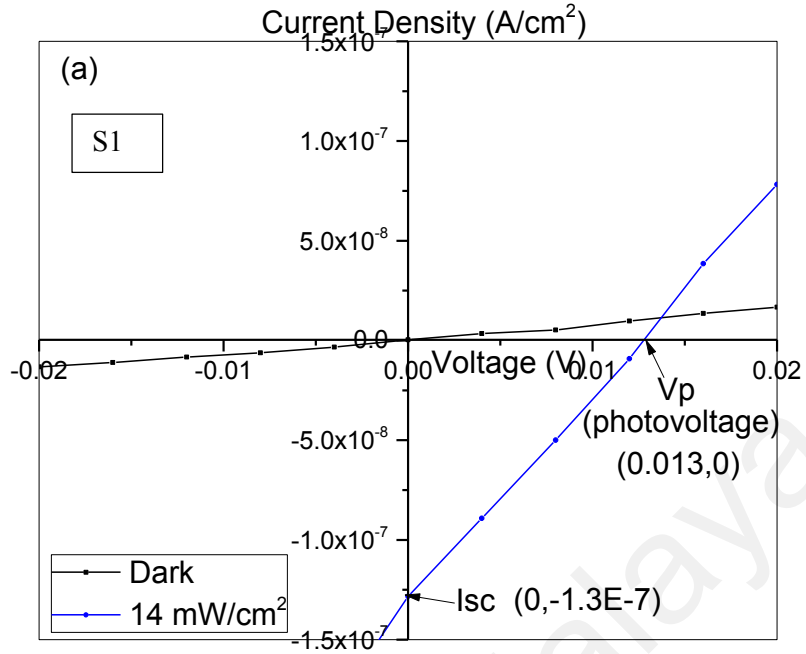
Compare the S1 and S2 in reverse bias under illumination, the S1 till generated higher current density but S1 is faster than S2 to reach the saturation. Below  $0.2 \text{ V}$ , the ratio of the photocurrent to dark current of S1 was higher than S2. However, beyond  $0.2 \text{ V}$ , the ratio of the photocurrent to dark current of S2 was higher than S1. After  $0.2 \text{ V}$ , the rate of increase of the current density in S2 was much higher than S1 because the photogenerated electrons were switched by the larger electric field force with high kinetic energy, resulting avalanche breakdown.

Figure 5.25 and Figure 5.26 were used to shown the photovoltage effect in AZO/p-Si heterojunction (S1 and S2). Figure 5.25(a) and 5.26(a) were enlarged of the J-V curve and the Figure 5.25(a) and 5.26(a) were overall of the J-V curve. Compare the S1 and S2, only the S1 shows the photovoltage effect. The photovoltage effect generated in S1 can be used to explain the lower turn voltage and higher photocurrent generated than S2 in forward bias. The photovoltage causes the barrier between the Fermi level ( $E_{fp}$ ) in p-Si

and Fermi level ( $E_{fn}$ ) in AZO. Therefore, photogenerated electron and majority carrier of AZO easier flow to p-Si side. However, compared to the commercial solar cell, the photovoltage generated by S1 was too low.



**Figure 5.24:** J-V characteristic of AZO/p-Si heterojunction under illumination: (a) S1 and (b) S2.



**Figure 5.25:** Load line for the photovoltaic mode of the S1: (a) enlarged and (b) overall of the curve.

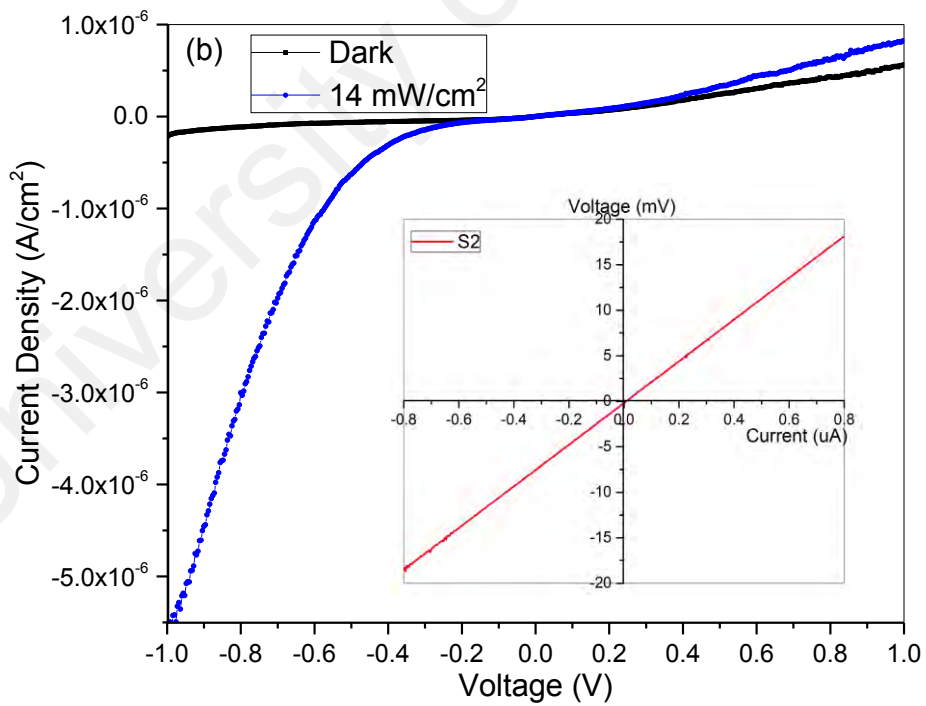
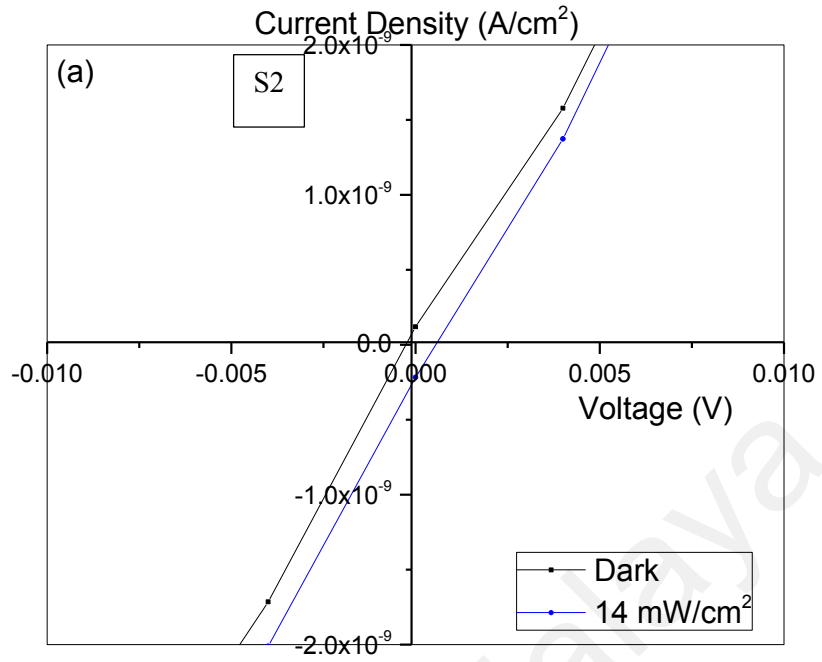


**Figure 5.26:** Load line for the photovoltaic mode of the S2: (a) enlarged and (b) overall of the curve.

## 5.6 Summary

In this section, 4 samples (S1, S2, S3 and S4) were prepared. AZO films were deposited on the p-Si to form Au/AZO/p-Si/Al heterojunction by 355 nm and 532 nm laser respectively. The reference sample (Au/p-Si/Al) without AZO films was illuminated by UV and visible light. The reference sample does not show any response to the UV light (Figure 5.17) but it shows photoreponse to the visible light in forward bias as shown in Figure 5.9.

Under Visible light illumination, the photoresponse of samples deposited by 532 nm laser (S3 and S4) were higher than those samples deposited by 355 nm laser (S1 and S2) in forward bias. As shown in Table 5.2, the samples deposited by 532 nm laser have higher ratio of photocurrent with dark current when compare to the 355 nm laser samples (S1 and S2) in forwards bias. According to the PL results, AZO thin films deposited by 532 nm laser possess only a small green peak often related to the defects in ZnO. Thus AZO is insensitive to visible light. Therefore, according to the explanation of Baydogan et al., 2012b; Gao et al., 2017; Jeong et al., 2003 and Bo et al., 2010, the visible photons would transmit through the AZO films layer and visible photons were absorbed mainly in depletion region of p-Si side to generated electron-hole pairs. In addition, under reverse bias, the ratio of photocurrent to dark current of samples (S1 and S2) deposited by 355 nm laser were higher than the 532 nm laser samples (S3 and S4). According to the PL results the AZO thin films deposited by 355 nm laser wavelength produced PL in UV and also visible (green) and the PL at the visible wavelength was higher intensity than the 382 nm peak. This indicated that there was ZnO defect energy level in the AZO thin films (355 nm). In the research of Kaur et al., 2015, the PL of the AZO defect prepared by PLD and the energy bandgap related to the AZO defect in optoelectronic were reported also. Therefore, the photogenerated electron hole pair are highly possible for the samples

deposited by 355 nm, rather than only act as a transmittance window. As shown in Figure 5.15, the photocurrent in reverse bias can be contributed by three mechanisms; which are electron-hole pair generated in p-Si side, photogenerated electrons trapped by low lying defect and jump to the higher defect by absorbing low energy visible and the transition from the higher defect to the conduction band.

Under UV illumination, all the samples show photoresponse to the UV light because of the wide bandgap of AZO thin films (Gao et al., 2017). According to the Tauc plot method, the AZO films bandgap of 3.3 eV to 3.45 eV are obtained. When the samples were illuminated by UV light, the energy would be absorbed through AZO thin films, a large quantity of photo-excited electron hole pairs were generated in the entire region of the ZnO layer (Hazra et al., 2014; Periasamy & Chakrabarti, 2011). Thus, those photogenerated electron-hole pairs in the depletion region would be switched to opposite direction under reverse bias operation (Hazra et al., 2014). Consequently, the current increases as the reverse bias increases. According to the report by Huang et al., 2009, the photogenerated carriers in forward bias are mainly dominated by the carriers at the depletion region of p-Si side whereas the photogenerated carriers in reverse bias are mainly dominated by those at the depletion region of AZO.

In addition, the photoresponse or the ratio of the photocurrent to dark current of AZO/p-Si heterojunction was affected by the resistivity of the AZO thin films. High doping or conductivity reduces the width of the depletion junction. Therefore, in this work, the lower resistivity sample (S1) generated more current and lower turn on voltage in forward bias and lower breakdown voltage in reverse bias under non-illumination. However, under illumination, the photoresponse or the ratio of the photocurrent to dark current of the high resistivity sample (S2) was higher than the lower resistivity sample

(S1) in reverse bias (-1 V). This was due to the wider depletion junction that can generate more photoexcited electron-hole pairs when compare to the narrower depletion junction.

University of Malaya

## CHAPTER 6: CONCLUSION AND SUGGESTION OF FUTURE WORK

### 6.1 Conclusion

In this work, plasma characteristics of 355 nm and 532 nm laser ablation of Al-doped (AZO) and the AZO thin films characteristics were studied. The AZO thin films were deposited on p-Si to form heterojunction. The properties and the characteristics of the AZO/p-Si heterojunction were investigated.

The plasma characteristics of 355 nm and 532 nm laser ablation of Al-doped ZnO (AZO) target were studied by optical emission spectroscopy and ion probe measurements. Zn emission lines were measured detected at above  $0.9 \text{ J/cm}^2$  for 355 nm laser and  $0.6 \text{ J/cm}^2$  for 532 nm laser respectively, while Al species were detected only above  $2 \text{ J/cm}^2$ . The kinetic energy of the ions was slightly higher for 532 nm ablation as compared to 355 nm ablation. In addition, the ablation of 532 nm laser was affected by the large laser penetration depth. When deposited at  $2 \text{ J/cm}^2$  and  $4 \text{ J/cm}^2$ , AZO films with energy band gap of 3.4 to 3.6 eV were obtained as compared to an undoped film which has a typical optical band gap of 3.27 eV. Nanostructured AZO films were obtained by 355 nm laser ablation but nano and micro-particulates were formed in 532 nm laser ablation. The large micron-sized particulates were Al-rich thus affecting not only the morphology but also the stoichiometry of the films. It is thus concluded that despite a lower ablation and growth rate, 355 nm generated Zn, O and also Al species at lower threshold fluence that can lead to high quality AZO films at room temperature.

In addition, AZO films deposited by 355 nm show higher transmittance, above 80 % in the visible, but AZO films deposited by 532 nm exhibits lower transmittance due to the submicron or micron-sized particulates. The AZO thin films deposited at  $2 \text{ J/cm}^2$  using 355 nm laser shows the lowest resistivity among the samples. The absorption coefficient

of the AZO films were  $\sim 10^5 \text{ cm}^{-1}$  at 355 nm  $\sim 10^4 \text{ cm}^{-1}$  at 532 nm. Both electrical resistivity and optical bandgap were better for the films deposited at  $2 \text{ J/cm}^2$  using a 355 nm laser. However, increasing the laser fluence increased the growth rate but produced films with higher resistivity.

The AZO films were deposited on the p-Si to form Au/AZO/p-Si/Al heterojunction by 355 nm and 532 nm laser respectively. The J-V characteristics of Au/AZO/p-Si/Al heterojunction when illuminated by UV and visible light were studied. All the samples (Au/AZO/p-Si/Al) shown response to UV light in reverse bias because the wide bandgap of AZO thin films, agreed to the report by others (Gao et al., 2017). However, under visible light illumination, the photoresponse of samples deposited by 532 nm laser were higher than samples deposited by 355 nm in forward bias and the photoresponse of samples deposited by 355 nm laser were higher than 532 nm laser samples in reserve bias. According to the report by Huang et al., 2009, the photogenerated carriers in forward bias are mainly dominated the carriers at the depletion region of p-Si side whereas the photogenerated carriers in reserve bias are mainly dominated those at the depletion region of AZO. In the case of samples deposited by 532 nm laser, the AZO thin films acted as a transmittance window where low energy visible light transmitted through the AZO films and was absorbed mainly at the depletion region of p-Si to generated electron-hole pairs. However, due to the high density of ZnO defect in 355 nm laser deposited samples, the photogenerated electron hole pair are also generated in the samples deposited by 355 nm, rather than only act as a transmittance window. The ratio of photocurrent to the dark current of the samples was affected by the resistivity of the samples. High doping or high conductivity samples reduces the width of the depletion junction. Therefore, lower resistivity samples generated more current and lower turn on voltage in forward bias and also lower breakdown voltage in reverse bias. However, the higher resistivity sample

generated more photoexcited electron-hole pairs in depletion region due to the wider depletion junction.

## **6.2 Suggestion of future work**

Several possible works can be carried out with the aims of the further studies of AZO thin films and AZO/p-Si heterojunction:

1. Deposition in other gas and background pressure (1 mTorr to 100 mTorr). Deposition in other gas may result in AZO with different properties. The absorption of light by traps of the AZO/p-Si may change, which directly affect the photoresponse of the AZO/p-Si heterojunction
2. Deposition by other laser. In order to more understanding the laser-produce plasma and the effect of the laser in AZO thin film. The effects of Femtosecond laser may be studied.
3. Multiple heterojunction (Au/ITO/AZO/p-Si/Al) may be deposited by PLD. The metal oxide semiconductor (MOS) and Varistor (MOV) effect may be formed in this multiple heterojunction (Au/ITO/AZO/p-Si/Al).

## REFERENCES

- Agura, H., Suzuki, A., Matsushita, T., Aoki, T., & Okuda, M. (2003). Low resistivity transparent conducting Al-doped ZnO films prepared by pulsed laser deposition. *Thin Solid Films*, 445(2), 263-267.
- Ajimsha, R., Jayaraj, M., & Kukreja, L. (2008). Electrical characteristics of n-ZnO/p-Si heterojunction diodes grown by pulsed laser deposition at different oxygen pressures. *Journal of Electronic Materials*, 37(5), 770-775.
- Alauddin, M., Song, J. K., & Park, S. M. (2010). Effects of aluminum doping and substrate temperature on zinc oxide thin films grown by pulsed laser deposition. *Applied Physics A: Materials Science & Processing*, 101(4), 707-711.
- Alivov, Y. I., Özgür, Ü., Doğan, S., Johnstone, D., Avrutin, V., Onojima, N., . . . & Morkoç, H. (2005). Photoresponse of n-ZnO/p-Si heterojunction diodes grown by plasma-assisted molecular-beam epitaxy. *Applied Physics Letters*, 86(24), 241108.
- Bai, Z., Yan, X., Chen, X., Cui, Y., Lin, P., Shen, Y., & Zhang, Y. (2013). Ultraviolet and visible photoresponse properties of a ZnO/Si heterojunction at zero bias. *RSC Advances*, 3(39), 17682-17688.
- Baskaran, A., & Smereka, P. (2012). Mechanisms of stranski-krastanov growth. *Journal of Applied Physics*, 111(4), 044321.
- Baydogan, N., Karacasu, O., & Cimenoglu, H. (2012a). Effect of annealing temperature on ZnO: Al/p-Si heterojunctions. *Thin Solid Films*, 520(17), 5790-5796.
- Baydogan, N., Karacasu, O., & Cimenoglu, H. (2012b). ZnO: Al thin films used in ZnO: Al/p-Si heterojunctions. *Journal of Sol-gel Science and Technology*, 61(3), 620-627.
- Bedia, F., Bedia, A., & Benyoucef, B. (2013). Electrical properties of ZnO/p-Si heterojunction for solar cell application. *International Journal of Materials Engineering*, 3(4), 59-65.
- Begum, N. J., & Ravichandran, K. (2013). Effect of source material on the transparent conducting properties of sprayed ZnO: Al thin films for solar cell applications. *Journal of Physics and Chemistry of Solids*, 74(6), 841-848.
- Bhaskar, R., Lakshmanan, A., Sundarrajan, M., Ravishankar, T., Jose, M., & Lakshminarayan, N. (2009). Mechanism of green luminescence in ZnO. *Indian Journal of Pure and Applied Physics*, 47(1), 772-774.

- Bo, H., Ma, Z. Q., Jing, X., Lei, Z., Sheng, Z. N., Feng, L., . . . & Yue, Z. C. (2010). Structural, electrical and optical properties of AZO/SiO<sub>2</sub>/p-Si SIS heterojunction prepared by magnetron sputtering. *Optica Applicata*, 40(1), 15-24.
- Bo, H., Quan, M. Z., Jing, X., Lei, Z., Sheng, Z. N., Feng, L., . . . & Shan, Y. Z. (2009). Characterization of AZO/p-Si heterojunction prepared by DC magnetron sputtering. *Materials Science in Semiconductor Processing*, 12(6), 248-252.
- Butcher, P., & Hearn, C. (1969). Hot electron effects. *Science Progress*, 1933, 229-257.
- Cao, B., Cai, W., & Zeng, H. (2006). Temperature-dependent shifts of three emission bands for ZnO nanoneedle arrays. *Applied Physics Letters*, 88(16), 161101.
- Cao, P., Han, S., Liu, W., Jia, F., Zeng, Y., Zhu, D., & Lu, Y. (2014). Effect of oxygen flowrate on optical and electrical properties in Al doped ZnO thin films. *Materials Technology*, 29(6), 336-340.
- Chang, J.-C., Guo, J.-W., Hsieh, T.-P., Yang, M.-R., Chiou, D.-W., Cheng, H.-T., . . . & Chu, S.-Y. (2013). Effects of substrate temperature on the properties of transparent conducting AZO thin films and CIGS solar cells. *Surface and Coatings Technology*, 231, 573-577.
- Chattopadhyay, K. K. (2009). *Introduction To Nanoscience And Nanotechnology*. Delhi, India : PHI Learning Pvt. Ltd.
- Chen, L.-C., & Tien, C.-H. (2010). Photocurrent Properties of Nanostructured ZnO/SiO<sub>2</sub>/Si Photodiodes in Magnetic Fields. *Current Nanoscience*, 6(4), 397-401.
- Chey, S. J., Liu, W., Yuan, M., & Mitzi, D. B. (2009). *Characterization of indium tin oxide and al-doped Zinc oxide thin films deposited by confocal RF magnetron sputter deposition*. Paper presented at the Photovoltaic Specialists Conference (PVSC), 2009 34th IEEE.
- Coleman, V., & Jagadish, C. (2006). Basic properties and applications of ZnO. *Zinc Oxide Bulk, Thin Films and Nanostructures: Processing, Properties, and Applications*, 1, 1-20.
- Craciun, V., Amirhaghi, S., Craciun, D., Elders, J., Gardeniers, J., & Boyd, I. W. (1995). Effects of laser wavelength and fluence on the growth of ZnO thin films by pulsed laser deposition. *Applied Surface Science*, 86(1-4), 99-106.

- Cranton, W., Kalfagiannis, N., Hou, X., Ranson, R., & Koutsogeorgis, D. (2016). Enhanced electrical and optical properties of room temperature deposited Aluminium doped Zinc Oxide (AZO) thin films by excimer laser annealing. *Optics and Lasers in Engineering*, 80, 45-51.
- Dong, B.-Z., Fang, G.-J., Wang, J.-F., Guan, W.-J., & Zhao, X.-Z. (2007). Effect of thickness on structural, electrical, and optical properties of ZnO: Al films deposited by pulsed laser deposition. *Journal of Applied Physics*, 101(3), 033713.
- Dosmailov, M., Leonat, L., Patek, J., Roth, D., Bauer, P., Scharber, M., . . . & Pedarnig, J. (2015). Transparent conductive ZnO layers on polymer substrates: Thin film deposition and application in organic solar cells. *Thin Solid Films*, 591, 97-104.
- Dutta, M., & Basak, D. (2008). p-ZnO/n-Si heterojunction: Sol-gel fabrication, photoresponse properties, and transport mechanism. *Applied Physics Letters*, 92(21), 212112.
- Duygulu, N. E., Kodolbas, A., & Ekerim, A. (2014). Effects of argon pressure and rf power on magnetron sputtered aluminum doped ZnO thin films. *Journal of Crystal Growth*, 394, 116-125.
- Edwards, P. P., Porph, A., Jones, M. O., Morgan, D. V., & Perks, R. M. (2004). Basic materials physics of transparent conducting oxides. *Dalton Transactions*(19), 2995-3002.
- Eshaghi, A., & Hajkarimi, M. (2014). Optical and electrical properties of aluminum zinc oxide (AZO) nanostructured thin film deposited on polycarbonate substrate. *Optik-International Journal for Light and Electron Optics*, 125(19), 5746-5749.
- Fallert, J., Hauschild, R., Stelzl, F., Urban, A., Wissinger, M., Zhou, H., . . . & Kalt, H. (2007). Surface-state related luminescence in ZnO nanocrystals. *Journal of Applied Physics*, 101(7), 073506.
- Fernandez, S., & Naranjo, F. (2010). Optimization of aluminum-doped zinc oxide films deposited at low temperature by radio-frequency sputtering on flexible substrates for solar cell applications. *Solar Energy Materials and Solar Cells*, 94(2), 157-163.
- Floro, J., Hearne, S., Hunter, J., Kotula, P., Chason, E., Seel, S., & Thompson, C. (2001). The dynamic competition between stress generation and relaxation mechanisms during coalescence of Volmer–Weber thin films. *Journal of Applied Physics*, 89(9), 4886-4897.

- Gao, Z., Jahed, N. M., & Sivoththaman, S. (2017). Biased Photoresponse Analysis of Al-ZnO Heterojunctions with n-and p-Type Silicon. *IEEE Transactions on Electron Devices*, 64(3), 1100-1107.
- Garcés, F., Budini, N., Arce, R., & Schmidt, J. (2015). Thickness dependence of crystalline structure of Al-doped ZnO thin films deposited by spray pyrolysis. *Procedia Materials Science*, 9, 221-229.
- George, S. M. (2009). Atomic layer deposition: an overview. *Chemical Reviews*, 110(1), 111-131.
- Ghosh, S., Das, K., Tripathy, N., Bose, G., Kim, D., Lee, T., . . . & Kar, J. (2016). Ultraviolet photodetection characteristics of Zinc oxide thin films and nanostructures. Paper presented at the IOP Conference Series: Materials Science and Engineering, 5(1), p.01235, IOP Publishing.
- Girtan, M., Vlad, A., Mallet, R., Bodea, M., Pedarnig, J., Stanculescu, A., . . . & Antohe, S. (2013). On the properties of aluminium doped zinc oxide thin films deposited on plastic substrates from ceramic targets. *Applied Surface Science*, 274, 306-313.
- Gong, S. C., Choi, Y.-J., Kim, H., Park, C.-S., Park, H.-H., Jang, J. G., . . . & Yeom, G. Y. (2013). Aluminum-doped zinc oxide formed by atomic layer deposition for use as anodes in organic light emitting diodes. *Journal of Vacuum Science & Technology A: Vacuum, Surfaces, and Films*, 31(1), 01A101.
- Gu, X., Zhu, L., Cao, L., Ye, Z., He, H., & Chu, P. K. (2011). Optical and electrical properties of ZnO: Al thin films synthesized by low-pressure pulsed laser deposition. *Materials Science in Semiconductor Processing*, 14(1), 48-51.
- Hasan, M. R., Xie, T., Barron, S. C., Liu, G., Nguyen, N. V., Motayed, A., . . . & Debnath, R. (2015). Self-powered p-NiO/n-ZnO heterojunction ultraviolet photodetectors fabricated on plastic substrates. *APL materials*, 3(10), 106101.
- Hazra, P., Singh, S., & Jit, S. (2014). Ultraviolet photodetection properties of ZnO/Si heterojunction diodes fabricated by ALD technique without using a buffer layer. *JSTS: Journal of Semiconductor Technology and Science*, 14(1), 117-123.
- Holmelund, E., Schou, J., Thestrup, B., Tougaard, S., Johnson, E., & Nielsen, M. M. (2004). Pulsed laser deposition of aluminum-doped ZnO films at 355 nm. *Applied Physics A*, 79(4-6), 1137-1139.
- Holmelund, E., Thestrup, B., Schou, J., Larsen, N. B., Nielsen, M. M., Johnson, E., & Tougaard, S. (2002). Deposition and characterization of ITO films produced by laser ablation at 355 nm. *Applied Physics A: Materials Science & Processing*, 74(2), 147-152.

- Hsu, Y.-H., Lin, J., & Tang, W. C. (2008). RF sputtered piezoelectric zinc oxide thin film for transducer applications. *Journal of Materials Science: Materials in Electronics*, 19(7), 653-661.
- Huang, H., Fang, G., Mo, X., Yuan, L., Zhou, H., Wang, M., . . . & Zhao, X. (2009). Zero-biased near-ultraviolet and visible photodetector based on ZnO nanorods/n-Si heterojunction. *Applied Physics Letters*, 94(6), 063512.
- Hussain, B., Ebong, A., & Ferguson, I. (2015a). *Zinc oxide and silicon based heterojunction solar cell model*. Paper presented at the Photovoltaic Specialist Conference (PVSC), 2015 IEEE 42nd.
- Hussain, B., Ebong, A., & Ferguson, I. (2015b). Zinc oxide as an active n-layer and antireflection coating for silicon based heterojunction solar cell. *Solar Energy Materials and Solar Cells*, 139, 95-100.
- Inguva, S., Vijayaraghavan, R. K., McGlynn, E., & Mosnier, J.-P. (2015). Highly transparent and reproducible nanocrystalline ZnO and AZO thin films grown by room temperature pulsed-laser deposition on flexible Zeonor plastic substrates. *Materials Research Express*, 2(9), 096401.
- Isherwood, P. J., Gona, M., Bowers, J. W., Neves, N., Newbatt, P., & Walls, J. M. (2015). *Comparison of DC and RF sputtered aluminium-doped zinc oxide for photovoltaic applications*. Paper presented at the Photovoltaic Specialist Conference (PVSC), 2015 IEEE 42nd.
- Janotti, A., & Van de Walle, C. G. (2009). Fundamentals of zinc oxide as a semiconductor. *Reports on Progress in Physics*, 72(12), 126501.
- Jarzebski, Z. (1982). Preparation and physical properties of transparent conducting oxide films. *Physica Status Solidi (a)*, 71(1), 13-41.
- Jeong, I.-S., Kim, J. H., & Im, S. (2003). Ultraviolet-enhanced photodiode employing n-ZnO/p-Si structure. *Applied Physics Letters*, 83(14), 2946-2948.
- Johnson, K. W., Guruvenket, S., Sailer, R. A., Ahrenkiel, S. P., & Schulz, D. L. (2013). Atmospheric pressure plasma enhanced chemical vapor deposition of zinc oxide and aluminum zinc oxide. *Thin Solid Films*, 548, 210-219.
- Kabra, V., Aamir, L., & Malik, M. (2014). Low cost, p-ZnO/n-Si, rectifying, nano heterojunction diode: Fabrication and electrical characterization. *Beilstein Journal of Nanotechnology*, 5(1), 2216-2221.

- Kaid, M., & Ashour, A. (2007). Preparation of ZnO-doped Al films by spray pyrolysis technique. *Applied Surface Science*, 253(6), 3029-3033.
- Kang, S. J., & Joung, Y. H. (2013). Optical and hall properties of Al-doped ZnO thin films fabricated by pulsed laser deposition with various substrate temperatures. *Journal of Materials Science: Materials in Electronics*, 24(6), 1863-1868.
- Kaur, G., Mitra, A., & Yadav, K. (2015a). Growth and properties of pulsed laser deposited Al-doped ZnO thin film. *Advance Materials Letter*, 6(1), 73-79.
- Kaur, G., Mitra, A., & Yadav, K. (2015b). Pulsed laser deposited Al-doped ZnO thin films for optical applications. *Progress in Natural Science: Materials International*, 25(1), 12-21.
- Kek, R., Lee, B. K., Nee, C. H., Tou, T. Y., Yap, S. L., Arof, A. K. B. H. M., & Yap, S. S. (2016). Plasma characteristics of 355nm and 532nm laser deposition of Al-doped ZnO films. *Surface and Coatings Technology*, 303, 191-196.
- Khomyak, V., Ilashchuk, M., Parfenyuk, O., & Shtepliuk, I. (2013). Fabrication and electrical characterization of the anisotype n-ZnO/p-CdTe heterostructures for solar cell applications. *Journal of Applied Physics*, 114(22), 223715.
- Kim, H., Horwitz, J., Qadri, S., & Chrisey, D. (2002). Epitaxial growth of Al-doped ZnO thin films grown by pulsed laser deposition. *Thin Solid Films*, 420, 107-111.
- Kim, H., Kim, J., Park, M., & Im, S. (2001). Photoelectric, stoichiometric and structural properties of n-ZnO film on p-Si. *Thin Solid Films*, 398, 93-98.
- Kim, W.-H., Maeng, W., Kim, M.-K., & Kim, H. (2011). Low pressure chemical vapor deposition of aluminum-doped zinc oxide for transparent conducting electrodes. *Journal of The Electrochemical Society*, 158(8), D495-D499.
- Klingshirn, C. (2007). ZnO: From basics towards applications. *Physica Status Solidi (b)*, 244(9), 3027-3073.
- Klingshirn, C. (2007). ZnO: Material, Physics and Applications. *Chemical Physics and Physical Chemistry*, 8(6), 782-803.
- Ko, H., Tai, W.-P., Kim, K.-C., Kim, S.-H., Suh, S.-J., & Kim, Y.-S. (2005). Growth of Al-doped ZnO thin films by pulsed DC magnetron sputtering. *Journal of Crystal Growth*, 277(1), 352-358.

- Kohiki, S., Nishitani, M., & Wada, T. (1994). Enhanced electrical conductivity of zinc oxide thin films by ion implantation of gallium, aluminum, and boron atoms. *Journal of Applied Physics*, 75(4), 2069-2072.
- Kulczyk-Malecka, J., Kelly, P., West, G., Clarke, G., & Ridealgh, J. (2011). Investigations of diffusion behaviour in Al-doped zinc oxide and zinc stannate coatings. *Thin Solid Films*, 520(5), 1368-1374.
- Kumar, N., Kaur, R., & Mehra, R. (2006). Characterization of sol-gel derived yttrium-doped n-ZnO/p-Si heterostructure. *Materials Science-Wroclaw*, 24(2/1), 375.
- Kuoni, A., Holzherr, R., Boillat, M., & de Rooij, N. F. (2003). Polyimide membrane with ZnO piezoelectric thin film pressure transducers as a differential pressure liquid flow sensor. *Journal of Micromechanics and Microengineering*, 13(4), S103.
- Lee, C.-T., & Chiu, Y.-S. (2015). Piezoelectric ZnO-nanorod-structured pressure sensors using GaN-based field-effect-transistor. *Applied Physics Letters*, 106(7), 073502.
- Lee, M., Sheu, J.-K., Lai, W., Su, Y.-K., Chang, S.-J., Kao, C., . . . & Chi, G.-C. (2003). Characterization of GaN Schottky barrier photodetectors with a low-temperature GaN cap layer. *Journal of Applied Physics*, 94(3), 1753-1757.
- Lei, L. C. (2004). Apparatus and method for vaporizing solid precursor for CVD or atomic layer deposition: Google Patents.
- Li, L. N., Zhao, Y., Chen, X. L., Sun, J., & Zhang, X. D. (2012). Effects of Oxygen Flux on the Aluminum Doped Zinc Oxide Thin Films By Direct Current Magnetron Sputtering. *Physics Procedia*, 32, 687-695.
- Liu, K., Sakurai, M., & Aono, M. (2010). ZnO-based ultraviolet photodetectors. *Sensors*, 10(9), 8604-8634.
- Liu, Y., Li, Q., & Shao, H. (2009). Optical and photoluminescent properties of Al-doped zinc oxide thin films by pulsed laser deposition. *Journal of Alloys and Compounds*, 485(1), 529-531.
- Liu, Y., Li, Y., & Zeng, H. (2013). ZnO-based transparent conductive thin films: doping, performance, and processing. *Journal of Nanomaterials*, 2013(2013), 9.
- Liu, Y., & Lian, J. (2007). Optical and electrical properties of aluminum-doped ZnO thin films grown by pulsed laser deposition. *Applied Surface Science*, 253(7), 3727-3730.

- Low, J. J., Kreider, M. L., Pulsifer, D. P., Jones, A. S., & Gilani, T. H. (2008). Band gap energy in silicon. *American Journal of Undergraduate Research*, 7(1), 27-32.
- Look, D. C., Farlow, G. C., Reunchan, P., Limpijumnong, S., Zhang, S., & Nordlund, K. (2005). Evidence for native-defect donors in n-type ZnO. *Physical Review Letters*, 95(22), 225502.
- Majumdar, S., & Banerji, P. (2009). Temperature dependent electrical transport in p-ZnO/n-Si heterojunction formed by pulsed laser deposition. *Journal of Applied Physics*, 105(4), 043704.
- Maksimov, O. (2010). Recent advances and novel approaches of p-type doping of zinc oxide. *Reviews on Advanced Materials Science*, 24(1-2), 26-34.
- Matsubara, K., Fons, P., Iwata, K., Yamada, A., Sakurai, K., Tampo, H., & Niki, S. (2003). ZnO transparent conducting films deposited by pulsed laser deposition for solar cell applications. *Thin Solid Films*, 431, 369-372.
- Miao, D., Jiang, S., Zhao, H., Shang, S., & Chen, Z. (2014). Characterization of AZO and Ag based films prepared by RF magnetron sputtering. *Journal of Alloys and Compounds*, 616, 26-31.
- Mishra, D., Greving, D., Confalonieri, G. B., Perlich, J., Toperverg, B., Zabel, H., & Petravic, O. (2014). Growth modes of nanoparticle superlattice thin films. *Nanotechnology*, 25(20), 205602.
- Mohanta, A., Simmons, J. G., Everitt, H. O., Shen, G., Kim, S. M., & Kung, P. (2014). Effect of pressure and Al doping on structural and optical properties of ZnO nanowires synthesized by chemical vapor deposition. *Journal of Luminescence*, 146, 470-474.
- Mohite, R. (2017). Deposition of Al-Doped ZnO Thin Films by Spray Pyrolysis for Photoelectrochemical Applications. *Indian Journal of Applied Research*, 6(10).
- Morkoç, H., & Özgür, Ü. (2009). General Properties of ZnO. *Zinc Oxide : Fundamentals, Material and Device Technology*. Weinheim, Germany: Wiley-VCH.
- Mridha, S., & Basak, D. (2007). Ultraviolet and visible photoresponse properties of n-Zn O/p-Si heterojunction. *Journal of Applied Physics*, 101(8), 083102.
- Murdoch, G., Hinds, S., Sargent, E., Tsang, S., Mordoukhovski, L., & Lu, Z. (2009). Aluminum doped zinc oxide for organic photovoltaics. *Applied Physics Letters*, 94(21), 138.

- Pandey, R., Yuldashev, S., Nguyen, H. D., Jeon, H. C., & Kang, T. W. (2012). Fabrication of aluminium doped zinc oxide (AZO) transparent conductive oxide by ultrasonic spray pyrolysis. *Current Applied Physics*, 12, S56-S58.
- Periasamy, C., & Chakrabarti, P. (2011). Large-area and nanoscale n-ZnO/p-Si heterojunction photodetectors. *Journal of Vacuum Science & Technology B, Nanotechnology and Microelectronics: Materials, Processing, Measurement, and Phenomena*, 29(5), 051206.
- Qi, H., Li, Q., Wang, C., Zhang, L., & Lv, L. (2007). Effects of oxygen pressure on n-ZnO/p-Si heterojunctions fabricated using pulsed laser deposition. *Vacuum*, 81(8), 943-946.
- R. MANOJ, M. K. J. (2012). Pulsed laser deposited ZnO:Al thin films for optoelectronic applications. *Journal of Intense Pulsed Lasers and Application in Advanced Physics*, 2(1), 11-15.
- Rodnyi, P., & Khodyuk, I. (2011). Optical and luminescence properties of zinc oxide. *Optics and Spectroscopy*, 111(5), 776-785.
- Samwel, B., Samiji, M., & Mlyuka, N. (2015). Effects of target composition on the optical constants of DC sputtered ZnO: Al thin films. *Tanzania Journal of Science*, 41(1), 38-47.
- Sundaram, K., & Khan, A. (1997). Work function determination of zinc oxide films. *Journal of Vacuum Science & Technology A: Vacuum, Surfaces, and Films*, 15(2), 428-430.
- Suzuki, A., Matsushita, T., Wada, N., Sakamoto, Y., & Okuda, M. (1996). Transparent conducting Al-doped ZnO thin films prepared by pulsed laser deposition. *Japanese Journal of Applied Physics*, 35(1A), L56.
- Tamiko, O., Takashi, M., Yuki, T., Hiroharu, K., Yoshihito, Y., Takeshi, I., & Yoshiaki, S. (2016). Sputtering deposition of Al-doped zinc oxide thin films using mixed powder targets. *Japanese Journal of Applied Physics*, 55(1S), 01AA08.
- Tan, K. C., Lee, Y. S., Yap, S. L., Kok, S. Y., Nee, C. H., Siew, W. O., . . . & Yap, S. S. (2014). Pulsed laser deposition of Al-doped ZnO films on glass and polycarbonate. *Journal of Nanophotonics*, 8(1), 084091-084091.
- Tanaka, H., Ihara, K., Miyata, T., Sato, H., & Minami, T. (2004). Low resistivity polycrystalline ZnO: Al thin films prepared by pulsed laser deposition. *Journal of Vacuum Science & Technology A: Vacuum, Surfaces, and Films*, 22(4), 1757-1762.

- Tang, X., Li, G., & Zhou, S. (2013). Ultraviolet electroluminescence of light-emitting diodes based on single n-ZnO/p-AlGaIn heterojunction nanowires. *Nano Letters*, 13(11), 5046-5050.
- Tauc, J. (1969). Optical properties and electronic structure of amorphous semiconductors *Optical Properties of Solids* (pp. 123-136): Springer.
- Thestrup, B., & Schou, J. (1999). Transparent conducting AZO and ITO films produced by pulsed laser ablation at 355 nm. *Applied Physics A: Materials Science & Processing*, 69(7), S807-S810.
- Tunna, L., Kearns, A., O'Neill, W., & Sutcliffe, C. (2001). Micromachining of copper using Nd: YAG laser radiation at 1064, 532, and 355 nm wavelengths. *Optics and Laser Technology*, 33(3), 135-143.
- Tuomisto, F., Ranki, V., Saarinen, K., & Look, D. C. (2003). Evidence of the Zn vacancy acting as the dominant acceptor in n-type ZnO. *Physical Review Letters*, 91(20), 205502.
- Valerini, D., Caricato, A., Lomascolo, M., Romano, F., Taurino, A., Tunno, T., & Martino, M. (2008). Zinc oxide nanostructures grown by pulsed laser deposition. *Applied Physics A: Materials Science and Processing*, 93(3), 729-733.
- Vempati, S., Mitra, J., & Dawson, P. (2012). One-step synthesis of ZnO nanosheets: a blue-white fluorophore. *Nanoscale Research Letters*, 7(1), 470.
- Wang, C., Chang, S.-J., Su, Y.-K., Chiou, Y., Chang, C., Lin, T., . . . & Tang, J.-J. (2005). High detectivity GaN metal-semiconductor-metal UV photodetectors with transparent tungsten electrodes. *Semiconductor Science and Technology*, 20(6), 485.
- Wang, F., Wu, M., Wang, Y., Yu, Y., Wu, X., & Zhuge, L. (2013). Influence of thickness and annealing temperature on the electrical, optical and structural properties of AZO thin films. *Vacuum*, 89, 127-131.
- Wei-Ying, Z., Sheng, Z., Li-Jie, S., & Zhu-Xi, F. (2008). Dependence of photovoltaic property of ZnO/Si heterojunction solar cell on thickness of ZnO films. *Chinese Physics Letters*, 25(5), 1829.
- Wei, S.-H., Li, J., & Yan, Y. (2008). *Design of shallow p-type dopants in ZnO*. Paper presented at the Photovoltaic Specialists Conference, 2008. PVSC'08. 33rd IEEE.

- Willander, M., Nur, O., Zhao, Q., Yang, L., Lorenz, M., Cao, B., . . . & Grundmann, M. (2009). Zinc oxide nanorod based photonic devices: recent progress in growth, light emitting diodes and lasers. *Nanotechnology*, 20(33), 332001.
- Wong, L., Chiam, S., Chim, W., Pan, J., & Wang, S. (2013). Highly conductive and transparent aluminum-doped zinc oxide thin films deposited on polyethylene terephthalate substrates by pulsed laser deposition. *Thin Solid Films*, 545, 285-290.
- Yang, C., Li, X., Yu, W., Gao, X., Cao, X., & Li, Y. (2009). Zero-biased solar-blind photodetector based on ZnBeMgO/Si heterojunction. *Journal of Physics D: Applied Physics*, 42(15), 152002.
- Yao, P., Hang, S., & Wu, M. (2013). Growth characteristics and properties of Al-doped ZnO thin films by DC magnetron sputtering from AZOY (R) target. *Transactions of the Canadian Society for Mechanical Engineering*, 37(3).
- Yap, S. S., Yong, T. K., Nee, C. H., & Tou, T. Y. (2016). Pulsed Laser Deposition of ITO: From Films to Nanostructures. *Application of Laser Ablation Films Deposition, Nanomaterial Synthesis and Surface Modification*. InTech.
- Ye, J., Gu, S., Qin, F., Zhu, S., Liu, S., Zhou, X., . . . & Shi, Y. (2005). Correlation between green luminescence and morphology evolution of ZnO films. *Applied Physics A: Materials Science & Processing*, 81(4), 759-762.
- Yousif, A. A. (2014). Current transport studies of n-ZnO/p-Si hetero-nanostructures grown by pulsed laser deposition. *International Journal of Application or Innovation in Engineering Management*, 3(1), 35-43.
- Yuan, H., Luo, B., Yu, D., Cheng, A.-j., Campbell, S. A., & Gladfelter, W. L. (2012). Atomic layer deposition of Al-doped ZnO films using ozone as the oxygen source: A comparison of two methods to deliver aluminum. *Journal of Vacuum Science & Technology A: Vacuum, Surfaces, and Films*, 30(1), 01A138.
- Zaharescu, M., Mihaiu, S., Toader, A., Atkinson, I., Calderon-Moreno, J., Anastasescu, M., . . . & Vojisavljevic, K. (2014). ZnO based transparent conductive oxide films with controlled type of conduction. *Thin Solid Films*, 571, 727-734.
- Zhang, Y., Gu, S., Tang, K., Ye, J., Ge, H., Yao, Z., . . . & Zheng, Y. (2015). Fabrication and characterization of highly oriented N-doped ZnO nanorods by selective area epitaxy. *Journal of Nanomaterials*, 2015, 7.
- Zhao, M.-H., Wang, Z.-L., & Mao, S. X. (2004). Piezoelectric characterization of individual zinc oxide nanobelt probed by piezoresponse force microscope. *Nano Letters*, 4(4), 587-590.

Zhu, H., Shan, C., Yao, B., Li, B., Zhang, J., Zhao, D., . . . & Fan, X. (2008). High spectrum selectivity ultraviolet photodetector fabricated from an n-ZnO/p-GaN heterojunction. *The Journal of Physical Chemistry C*, 112(51), 20546-20548.

Zhu, K., Yang, Y., Wei, T., Tan, R., Cui, P., Song, W., & Choy, K.-L. (2013). Room temperature DC magnetron sputtering deposition of hydrogenated aluminum doped zinc oxide thin films on polyethylene terephthalate substrates. *Materials Letters*, 106(1), 363-365.

University of Malaya

## LIST OF PUBLICATIONS AND PAPERS PRESENTED

**Kek, R.,** Lee, B. K., Nee, C. H., Tou, T. Y., Yap, S. L., Arof, A. K. B. H. M., & Yap, S. S. (2016). Plasma characteristics of 355nm and 532nm laser deposition of Al-doped ZnO films. *Surface and Coatings Technology*, 303, 191-196

University of Malaya